Experimental Studies for the Second-Forbidden non-unique β decay of ^{20}F at IGISOL

Master's thesis, October 9, 2018

Author:

Marjut Hukkanen

Supervisor:

Anu Kankainen

JYVÄSKYLÄN YLIOPISTO
FYSIIKAN LAITOS

Abstract

Hukkanen, Marjut
Experimental Studies for the Second-Forbidden non-unique β decay of ^{20}F at IGISOL
Master's thesis
Department of Physics, University of Jyväskylä, 2018, 73 pages.

The evolution of stars is determined by the stars initial mass, smaller stars with masses under eight solar masses end their life as a white dwarf when the heavier stars with masses over 11 solar masses end as core-collapse supernovae. The evolutionary path of the intermediate-mass star with masses between 8 to 11 solar masses is still uncertain. The electron capture on ^{20}Ne ground state leading to ^{20}F ground state has been estimated to have an important role in the evolution of intermediate-mass stars. The branching of this ground-state to ground-state transition has previosly had only an experimental upper limit. This thesis focuses on the experimental developments of a measurement setup which we used to measure this branching ratio for the first time.

The measurement was done at the Ion Guide Isotope Separator On-Line (IGISOL) facility in the Accelerator Laboratory of the University of Jyväskylä. The $^{20}F^{+}$ ions were produced via ^{19}F(d,p)^{20}F reaction with a 9 MeV deuteron beam. The experimental setup consisted of a Siegbahn-Slätis type of intermediate-image spectrometer, plastic scintillator detector and of $LaBr_3$(Ce) detector. This work gives of a detaled description of the measurement setup and its testing as well as a brief discussion of the stellar evolution related topics and of an overview of the successful experiment.

Keywords: stellar evolution, intermediate-mass stars, IGISOL, beta decay, Siegbanh-Slätis type intermediate-image spectrometer, scintillator detector

Tiivistelmä

Hukkanen, Marjut
Kokeelliset tutkimukset toisen kertaluokan kielletylle, epäuniikille, ^{20}F beetasiirtymälle IGISOL-laitteistolla
Pro Gradu -tutkielma
Fysiikan laitos, Jyväskylän yliopisto, 2018, 73 sivua

Tähtien evoluution vaiheet perustuvat tähden alkuperäiseen massaan: kevyemmät tähdet, joiden massa on alle kahdeksan Auringon massaa päättävät evoluutionsa valkoisena kääpiönä, kun taas suuremmat tähdet, joiden massa on suurempi kuin 11 Auringon massaa päätyvät supernoviksi, jotka johtuvat tähden ytimen luhistumisesta. Kuitenkin keskimassaisten tähtien evolutiivinen kaari on vielä epäselvä. On arvioitu, että keskimassaisten tähtien evoluutiossa ^{20}Ne ytimeen taphtuvilla elektronisieppauksilla, jotka johtavat ^{20}Fe ytimen perustilalle, on tärkeä rooli. Kuitenkin tälle perustilalta perustilalle tapahtuvan siirtymän voimakkuudelle on määritetty vain kokeellinen yläraja. Tämä työ keskittyy mittauslaitteiston, jolla mittasimme onnistuneesti kyseisen siirtymän vahvuuden ensimmäistä kertaa, kokeelliseen kehitystyöhön.

Mittaukset tapahtuivat IGISOL-tutkimusryhmän tiloissa Jyväskylän yliopiston kiihdytinlaboratoriossa. $^{20}F^{+}$-ionit tuotettiin ^{19}F(d,p)^{20}F reaktiolla käyttämällä 9 MeV energistä deuteronihiukkassuihkua. Kokeellinen laitteisto koostui Siegbahn-Slätis tyypin keskikuvantavasta spektrometristä, muovituikeilmaisimesta ja $LaBr_3$(Ce)-ilmaisimesta. Tämä työ antaa kuvauksen käytetystä mittauslaitteistosta ja sen testauksesta sekä lyhyen esittelyn tähtien evoluutioon liittyvistä aiheista ja katsauksen onnistuneeseen perustilalta perustilalle tapahtuvan siirtymän mittaukseen.

Avainsanat: tähtien evoluutio, IGISOL, beetahajoaminen, Siegbahn-Slätis tyypin keskikuvantava spektrometri, tuikeilmaisin

Acknowledgements

I want to thank my supervisor Dr. Docent Anu Kankainen for firstly introducing this project and convincing me of it, even if at the beginning I had no clue what even the name of the project meant. Secondly, I want to thank her for the patience, kind words and the excellent guidance through the whole process of this thesis work. The constant feedback and comments on my work have been extremely helpful and have shaped me especially towards a better academic writer. Especially one meeting has stuck to me, when I was feeling down from the work and felt like the thesis was going nowhere and she gave me the encouraging words "there is not much more left to go" even if it still was a lot more to be done, but I definitely needed the encouraging words. I want to thank the whole IGISOL group for taking me in and giving me helping hands, tools, lunch company and advice. I also want to express my gratitude for Dr. Oliver Kirsebom for letting me join the project, trusting me on the work and giving me guidance on both the experimental work and the data analysis. I want to also thank Dr. Wladyslaw H. Trzaska for enlightening discussions and help during this project. This thesis project has been probably one of the best and teaching master's thesis projects one could have, and it has taught me many things, including that the job of a physicist has many more sides than I thought there were.

I want to thank my family for always being supportive for my studies even if it has made me so busy that I don't always have the time to visit. I want to thank my friends for sticking with me all these years and especially for the support you have given me. A separate thank you is needed for the friends called "Fyysiot/Naisfyysiot" who were the group of people who were with me at the same situation on the first day of university and have studied with me all these years, without you I would have never been able to finish this.

Jyväskylä, October 8, 2018
Marjut

Contents

List of Figures

List of Tables

1 Introduction

The evolutionary path of a star can be determined by the mass of the star: lighter mass stars with masses up to eight solar masses (8 $M_\odot$) end up as white dwarfs and heavier mass stars (from 11 $M_\odot$ up) as core-collapse supernovae. But the evolution of the stars between these two, intermediate-mass stars of $8 - 10$ $M_\odot$, cannot yet be predicted as well as for the light- and heavy-mass stars. The intermediate-mass stars develop a degenerate core consisting of oxygen, formed during helium burning via $^{12}C + \alpha$ reactions, and carbon burning products, neon and magnesium. The ONe or ONeMg core can reach such a heavy mass that the star undergoes a collapse of the core. This happens when the electron degeneracy pressure can no longer resist the gravity. Here electron capture reactions, which relieve the pressure that is created by the electrons, play a key role. Electron capture reactions on ^{20}F heat the core, and a $^{16}O + ^{16}O$ thermonuclear runaway will ignite impacting the last stages of the evolution of the star. This leads to either complete or partial distruption of the core or collapse into a neutron star. The impact of this thermonuclear runaway is still uncertain because of the uncertainty for example in determining the oxygen ignition density. Martínes-Pinedo et al. [1] have shown that the second-forbidden, non-unique, ground-state to ground-state transition between ^{20}Ne and ^{20}F, could dominate the electron-capture rate in an important temperature-density range. In order to determine the strength of this transition and its role in the evolution of intermediate-mass stars, its branching ratio needs to be known. Before this work, only an upper experimental limit of the branching ratio was known [2]. We have successfully measured the ground-state to ground-state transition for the first time.

The measurements were conducted at the Ion Guide Isotope Separator On-Line (IGISOL) facility in the Accelerator Laboratory of the University of Jyväskylä. The ^{20}F activity was produced in a $^{19}F(d,p)^{20}F$ reaction using 9 MeV deuterons from the K130 cyclotron on a thin BaF_2 target. The $^{20}F^+$ ions were mass-separated with a 55° dipole magnet and transported to the experimental setup where the ions were implanted on a thin carbon foil. A setup consisting of a refurbished Siegbahn-Slätis type of intermediate image spectrometer, a plastic scintillator and a $LaBr_3(Ce)$ scintillator detector, was built at the end of the spectroscopy line at IGISOL.

This thesis provides a brief discussion of the stellar evolution and β decay as well as a detailed discussion of the experimental methods and preparation measurements. The main goal is to give a good overview of the experimental preparations done as well as a short overview of the successful experiment on determining the branching ratio of the second-forbidden, non-unique ground-state to ground-state transition between ^{20}F and ^{20}Ne.

2 Theoretical background

2.1 Evolution of stars

The life of a star starts from a large and dense interstellar gas cloud, which is called nebula. The nebulae consist mainly of hydrogen and helium. The cloud will start to contract under its own gravity increasing the density and opacity of the cloud. When the cloud becomes more opaque the emitted radiation cannot escape the densest parts of the cloud which leads to a temperature and pressure rise. A nebula does not form only one protostar but multiple. The pressure rise in the contracting fragment of the gas cloud will stop the contraction. Just after the full stop of the contraction the deuterium fuses with hydrogen and the possible lithium is broken down by the interactions with protons. When the temperature has risen to several millions of kelvins, hydrogen to helium fusion can start in the protostar. These two elements are the main energy sources of smaller stars. [3, 4]

In this thesis smaller stars are considered to be bigger than the mass of 0.4 $M_\odot$ but below mass of 8 $M_\odot$. The path of stellar evolution for smaller mass stars described below is shown at the top part of Fig. 1. The hydrogen fusion can proceed in two different ways: via pp chains in stars under the mass 1.5 $M_\odot$ or via CNO cycles in stars with more mass. At the stage when hydrogen fusion is the only energy source of the star, the star is said to be in the main sequence phase. This is also the longest phase in the evolution of the smaller stars. [3, 4] Our Sun is a good example of a smaller star where the main sequence phase will take place for $9.3 \cdot 10^9$ years [3].

The next phase, subgiant branch phase, starts when the main sequence star has burned all the hydrogen to helium in the centre of the star. The hydrogen burning will still continue around the helium core as a hydrogen burning shell. In the subgiant phase the envelope of the star is expanding because the hydrogen around the core is still being burned into helium, adding to the size of the core and providing energy for the surface expansion. Due to this surface expansion the star has moved to a red giant phase. [3, 4]

In stars with mass under 2.3 $M_\odot$ the core becomes degenerate due to the high density [4]. Degenerate matter resists compression because the Pauli exclusion principle states that only maximum two spin-1/2 particles can occupy a given quantum state at the same

time. This means that the lower levels are already occupied hence electrons cannot move to those [3]. The temperature keeps rising to a level where the helium can be burned into carbon. The helium burning causes the temperature of the degenerate core to rise even higher, but the star cannot compensate by expandig due to the degeneracy. The degeneracy is lifted when the star reaches high enough temperature leading to a sudden expansion of the core. This is called a helium flash. The star has moved to horizontal branch phase, where it resides burning helium in the core as the main energy source. For the Sun the horizontal branch phase takes around $0.1 \cdot 10^9$ years before moving to the next phase. [3, 4]

When the helium has been burnt into carbon and oxygen, the helium core is exhausted and the core can contract again. The contraction causes heating up and igniting the helium that is around the surrounding shell. This phase of the evolution of a star is called the asymptotic giant branch phase. Now the star can be divided into the carbon-oxygen core, helium burning shell and to a hydrogen burning shell. The energy of the star is generated in turns in the hydrogen and helium burning shells because the smaller stars are not heavy enough to fuse carbon. When the star is alternating between the energy generation in hydrogen or helium shell the star is called to be thermally pulsing. The pulsing also makes the star lose mass as a stellar wind. This stellar wind is called a planetary nebula. [3]

The stars with masses over 2.3 $M_\odot$ have a similar yet different evolution than the stars under this mass. The core does not become degenerate leading to a result where the helium flash does not occur. These stars undergo a few different phases than the lighter stars but end their evolution with planetary nebulae and a cooling down phase. [3]

The small star is coming to the last phases of its evolution with the remaning hydrogen burning shell extinguishing. After this only the carbon-oxygen core remains with the cooling down. The life of a small star ends as a white dwarf which has a mass around 0.5 $M_\odot$. [3, 4]

When looking at larger stars that have masses over 11 $M_\odot$, the evolution timescale is much shorter than in small stars (for heavy stars around $7 \cdot 10^6$ years). At the bottom part of Fig. 1 the evolution of a larger star is shown. The hydrogen and helium is burnt in a similar way than in smaller stars, but faster due to the faster contraction under the heavier mass. The burning of helium is warming up the outer shell of hydrogen which causes expansion of the shell and leads to a red supergiant star. The phase of helium burning in the core takes around $8 \cdot 10^5$ years before the helium of the core has been fully

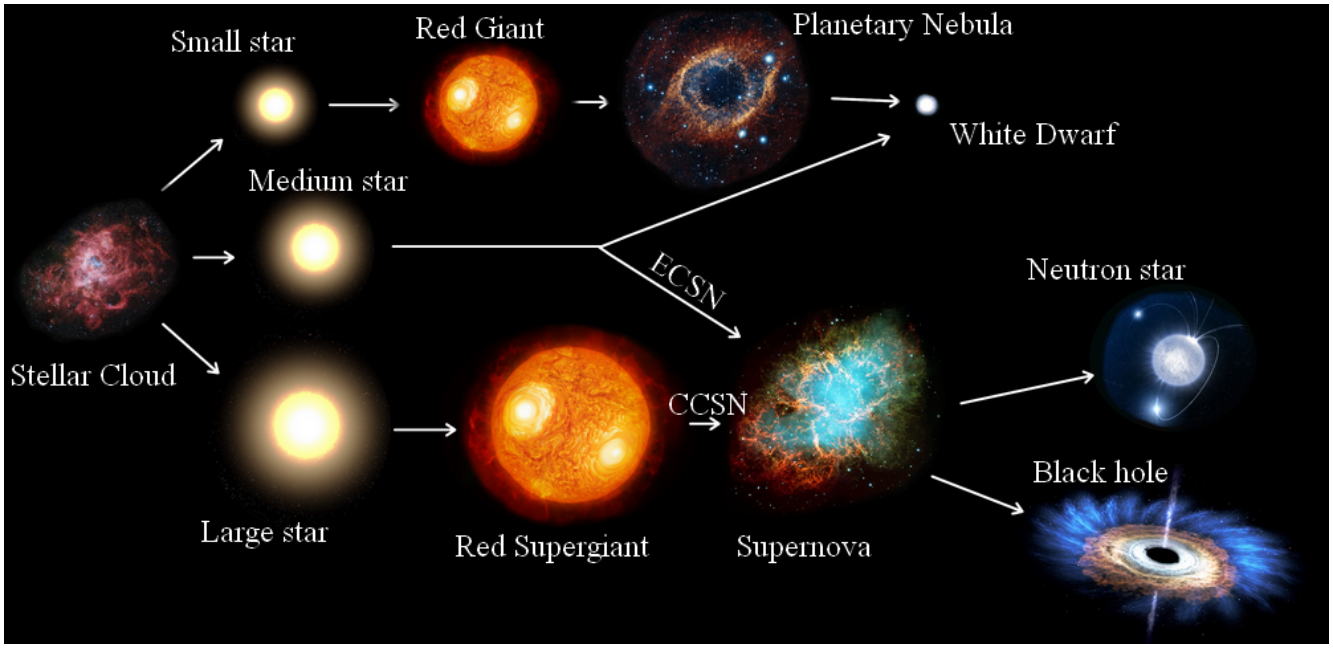

Figure 1. The path of stellar evolution for stars with different initial masses. The small star follow a path to a white dwarf while the larger star ends up as a neutron star or a black hole. The fate of the medium-mass stars is still uncertain with the choises of a white dwarf or an electron capture supernova leading to a neutron star. [5, 6]

burnt. The helium burning still continues on a shell between the outer hydrogen burning shell and the exhausted core.

Next in the evolution of a heavier mass stars are four different core burning stages which create similar shells around the core as the hydrogen shell: carbon burning, neon burning, oxygen burning and silicon burning. These burning stages lead to a star that has an onion like structure with the different shells of elements and an iron core. The shell burning reactions are still going, adding to the mass of the iron core. The iron in the core cannot be burnt because fusion reactions would require energy contrary to the fusion of lighter elements, which release energy. The iron core grows until the Chandrasekhar's mass limit ($\approx 1.4 M_\odot$), where the core suddenly collapses because the electron degeneracy pressure cannot hold against the gravitational pressure. These events lead to a core collapse supernova explosion disrupting star's outer layers and ejecting heavier synthesized elements into the interstellar medium. A massive star is destroyed by the core-collapse supernova leaving either a neutron star or a black hole as a remanant. [3, 4]

The stellar evolution of intermediate-mass stars (8 $M_\odot$-11 $M_\odot$) is still not well established. The intermediate-mass stars are formed from a similar protostar as discussed above. These intermediate-mass stars are heavy enough to burn carbon in their carbon-

oxygen cores leading to ONe or ONeMg cores. The star is at a super asymptotic giant branch (SAGB) when the carbon has been ignited. In the ONeMg cores the electron captures on ^{24}Mg start first and after that the captures on ^{20}Ne set in. A detailed discussion of the effects of the electron captures on ^{20}Ne are given in the next chapter. The energy released through the γ-rays from the decay of ^{20}O which follows from the electron capture on ^{20}Ne and subsequently on ^{20}F and the collapsing core will start a ^{16}O+^{16}O thermonuclear runaway. [7] There is still a lot of debate ongoing about the final evolution of the intermediate-mass stars following the thermonuclear runaway: will the star eject its outer layers as planetary nebula and end up as an oxygen-neon white dwarf [3, 7] or does it form an electron capture supernova and collapse into a neutron star [8, 9]. The biggest uncertainties in the modeling of the evolution of an intermediate-mass star are in the mass loss, convective boundary mixing and the ignition density of the oxygen deflagration [7]. The ignition density of oxygen depends on the the electron capture rates of ^{24}Mg and even more strongly on the electron capture rate of ^{20}Ne. A more detailed discussion about the uncertainties and results of earlier research on the evolution of intermediate-mass stars are well summerized in Ref. [7].

2.2 ^{20}Ne electron capture in the evolution of 8 -10 $M_\odot$ stars

The intermediate-mass stars have electron-degenerate ONe or ONeMg cores where the pressure created by electron degeneracy in the core can be lost due to the electron captures. The most crucial electron captures in determining the evolution of the intermediate-mass star happen on nuclei ^{20}Ne and ^{24}Mg [1]. These electron captures reduce the electron fraction (reducing electron degeneracy pressure) and rises the temperature of the core leading to the accelerated contraction of the core. Electron capture on even-A nuclei lead to heating of the core contrary to electron capture on odd-A nuclei where it can lead to a so-called Urca process where the core is cooled via neutrino emissions following the electron captures [10]. The compression of the core leads to increasing electron chemical potential.

At the astrophysically relevant densities (when $\log_{10}\rho$ is between 9.0 to 10.0) the electron capture on ^{20}F will happen immediately after the capture on ^{20}Ne happens, but the electron captures do not at least directly lead to the convection in the core. When there is no convection, the temperature will grow which leads to a thermal runaway. Due to these events the core heats up until the temperature is high enough to ignite oxygen. The electron capture on ^{24}Mg happens at a different density and is not as crucial as electron

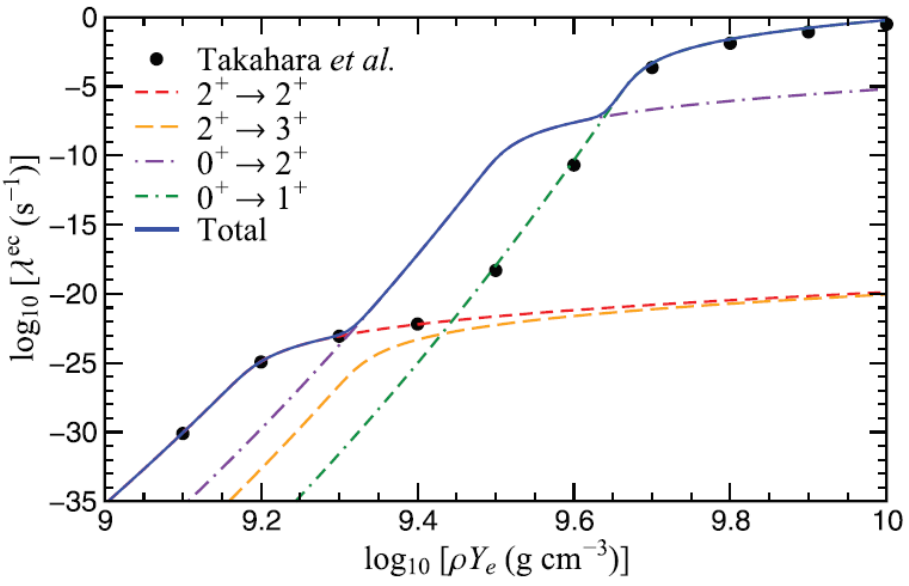

Figure 2. Calculated electron capture rates for four different transitions in determining the total electron capture rate of ^{20}Ne. The black dots represent electron capture values given by Takahara et al. for a comparison to the calculated values by Martínez-Pinedo et al. [1].

captures on ^{20}Ne for the evolution of the star. [9] The electron capture chain that starts with the electron capture on ^{20}Ne is given as

$$^{20}\mathrm{Ne} + e^- \rightarrow ^{20}\mathrm{F} + \nu_e \qquad ^{20}\mathrm{F} + e^- \rightarrow ^{20}\mathrm{O} + \nu_e,$$

where the Q value for the electron capture of the ^{20}Ne ground-state to ^{20}Fe ground-state transition is $-7024.467(0.030)$ keV [10, 11].

In Fig. 2 calculated electron capture rates of ^{20}Ne are presented by Martínez-Pinedo et al. [1]. The electron capture rates were calculated on transitions that are crucial on determining the electron capture rate of ^{20}Ne at the astrophysically relevant density and temperature range. Whenever the electron chemical potential is less than the electron capture threshold the capture rates grow exponentially. This changes when the electron chemical potential reaches the same level as the electron capture threshold. As seen in the figure at the lower densities the capture on the exited 2^+ state of ^{20}Ne to the ground state (2^+) in ^{20}F is favored. Next the electron capture from the ground state to ground state is favored (the temperatures are under 0.9 GK) and so on. The conclusion of the calculations by Martínez-Pinedo et al. was that the second-forbidden, non-unique, ground-state to ground-state transition would dominate the electron capture rate in an important temperature-density range. The calculation cannot yet be strongly backed up with an experimental value because only an experimental upper limit has been measured, which is dicussed in the next section. But even if the strength of the transition is smaller than this upper limit the second-forbidden transition is still likely to dominate the electron capture rate in this important temperature-density range. [1]

These calculated electron capture rates on ^{20}Ne have been used on MESA (Modules for Experiments in Stellar Astrophysics) simulations by J. Schwab et al. on the impact of the second-forbidden, non-unique, ground-state to ground-state transition on the density-temperature range of the oxygen ignition [9]. A figure of this MESA simulation is shown in Fig. 3. In this figure the solid blue line represents the temperature-density dependance evolving if the second-forbidden 0^+ to 2^+ transition was not accounted for, while the solid red line represent the temperature-density dependance evolving if the second-forbidden 0^+ to 2^+ transition was 10^3 below the experimental upper limit. From these it can be noticed that the electron captures on ^{20}Ne start at a lower density when the transition is accounted for. The oxygen ignition also happens at a different density-temperature pair when the transition is accounted for even if the difference is not as big as the difference on the starting density of the electron captures. Due to only having an experimental upper limit for this second-forbidden, non-unique, ground-state to ground-state transition, it

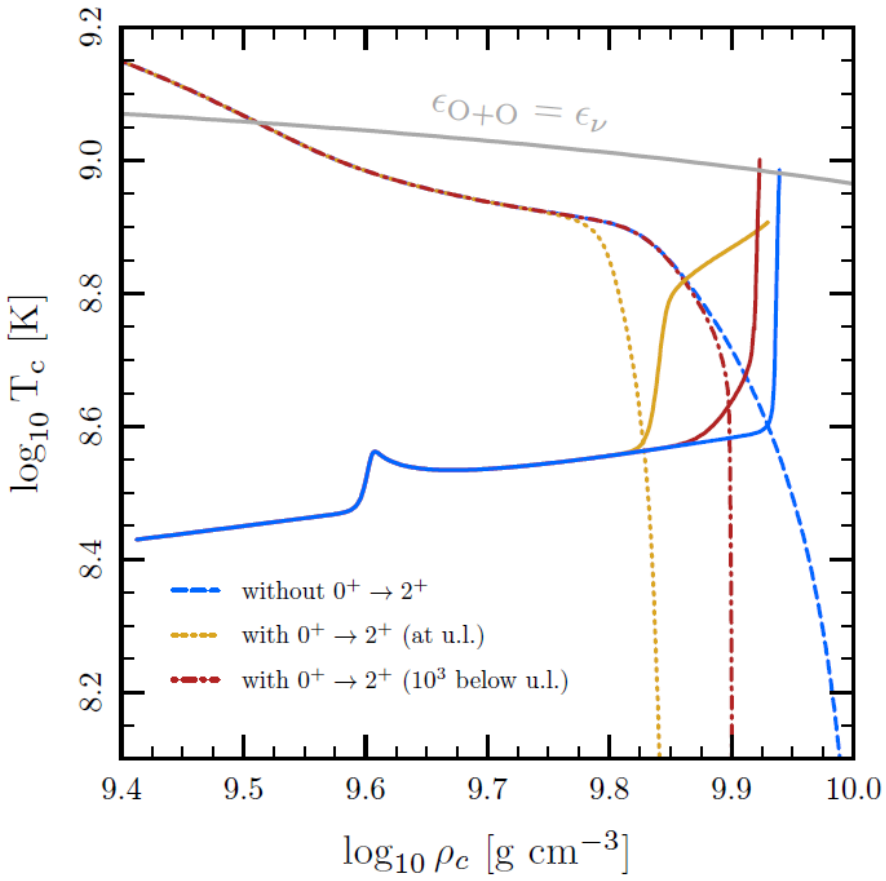

Figure 3. A comparison of the impact of the transition strength of the second-forbidden, non-unique transition on the oxygen ignition density. The change in density is seen where the solid blue line (without the transition) and the solid red line (transition 10^3 below the upper limit) are shown. The dotted, dash-dotted and dashed lines show were the time-scale for ^{20}Ne captures is equal to the fiducial compression time-scale (10^4 yr) for different values of the ground-state to ground-state transition strengths. [9]

brings a major uncertainty to the simulations of the final stages of the intermediate-mass star evolution.

2.3 β-decay

The first classification of β decay was done by Rutherford when he classified the three different types of radiation emitted by their ability to penetrate materials. In the early studies of β decay in 1920's, it was noticed that there were no well-defined energies but a continuous spectrum of energies when the energy distribution was measured. A solution for the continuous energy spectrum, which seemed to break the laws on momentum and energy conservation, was introduced by Pauli in 1931, and later given a name of neutrino by Fermi. This lead to a successful theory of the β decay by Fermi, which will be discussed in detail below. [12]

Nuclear β decay can be divided into three different decay modes: β^- decay, β^+ decay and electron capture (EC). In β^- decay a neutron is converted into a proton while releasing an electron (e^-) and an electron antinneutrino ($\bar{v}_e$). In β^+ decay a proton is converted into a neutron while releasing a positron (e^+) and an electron neutrino (v_e). In electron capture the nucleus captures an electron from one of the inner electron shells and converts a proton into a neutron and electron neutrino. In β decay the mass number A stays constant, but the proton and neutron numbers change accordingly. The β decay increases the binding energy of the nucleus, moving closer to the valley of stability. All β decays are weak-interaction transitions. [12, 13]

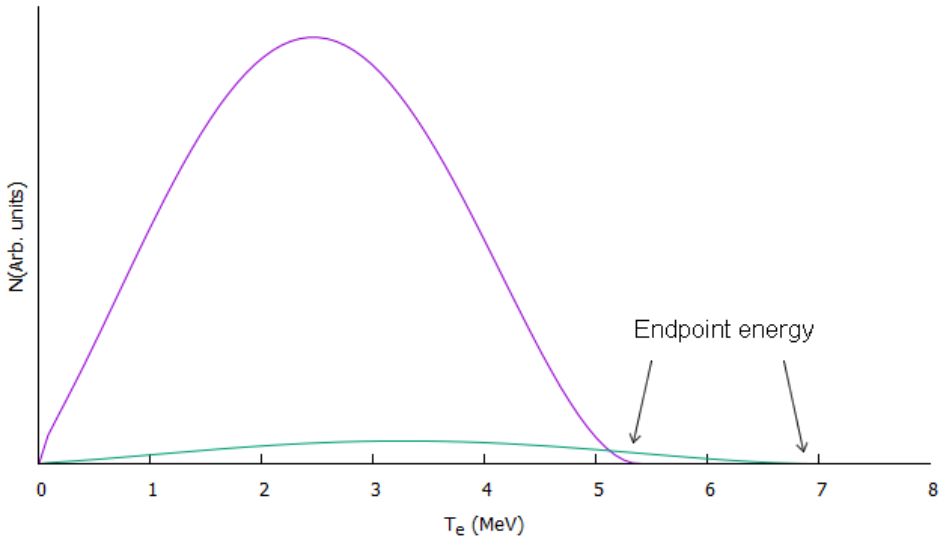

Figure 4. A schematic view of a continuous energy spectrum of the β decay of ^{20}F. The $2^+ \rightarrow 2^+$ transition is shown in lilac color and the ground-state to ground-state transition ($2^+ \rightarrow 0^+$) is shown in green.

Table 1. Selection rules for allowed and forbidden β decays.

Type		ΔJ	$\Delta\pi$
Allowed			
	Fermi	0	no
	Gamow-Teller	0 or 1 (except: $0^+ \rightarrow 0^+$)	no
Forbidden			
1st		0, 1 or 2	yes
2nd		2 or 3	no
3th		3 or 4	yes
4th		4 or 5	no

When looking at an energy spectrum measured from a β decaying nucleus it can be seen that the distribution is continuous over the energies from zero to the enpoint energy Q_β. A schematic β decay spectrum of ^{20}F is shown in Fig. 4. The continuous trend can be explained by the neutrino (or antineutrino) and β particle sharing the energy from the decay and while the β particle stops fully in the detector, the neutrino usually does not. The neutrino also obeys the laws of momentum and charge conservation meaning that the neutrino is a neutral particle and shares the momentum from the reaction. [12, 14]

A β decay can be classified to be an allowed or forbidden transition depending on the angular-momentum transfer between the initial and final states and the parities of these states. The change in the total angular momentum and parity are called the selection rules for the β decay. Allowed β decays are further divided into Fermi and Gamow-Teller decays. In Fermi decays the electron (positron) spin is opposite to the spin of the antineutrino (neutrino), and they couple to a total spin $S = 0$. In Gamow-Teller type of transitions they are parallel and couple to a total spin $S = 1$. There is no change in spin and parity for Fermi decays ($\Delta J = 0$, $\Delta\pi = no$). For Gamow-Teller decays, there is no parity change ($\Delta\pi = no$) and either no spin change ($\Delta J = 0$; except $0^+ \rightarrow 0^+$) or a spin change coupled to one ($\Delta J = 1$). [13, 15]

In forbidden β decay's the change in total angular momentum is higher while there either is or is not a change in parity. The name "forbidden decay" does not mean that the decay does not happen but forbidden decays are not as probable as allowed decays. The order of forbiddenness of a β decay can be defined by the selection rules which are presented in table 1. The forbidden decays can be further divided into unique and non-unique forbidden decays. For a unique Kth forbidden β transition the change in total angular momentum is $\Delta J = K + 1$ and for a non-unique Kth forbidden β transition the change in total angular momentum is $\Delta J = K$ when the order $K \geq 1$. [13]

When calculating the transition probability of a β decay three essential things need to be taken into account: the formation of an electron and a neutrino, relativistic treatment of these two particles and the calculation needs to give an continuous energy distribution. In the Fermi theory it is assumed that the rest mass of the neutrino is zero.

Fermi's Golden Rule equation for the transition probability can be written as

$$\lambda = \frac{2\pi}{\hbar}|V_{if}|^2\rho(E_{if}), \tag{1}$$

where V_{if} is the transition matrix element of the interaction between the intial state and the final state decribed with the integral of the wave functions as follows: $V_{fi} = \int \psi_f^* V \psi_i dv$. The term $\rho(E_{if})$ is the energy density of the final states. The probability of the transition to happen is bigger when there is more final states accessible. The derivation starting from the Fermi's Golden Rule and ending up with the equation of the energy spectrum for β decay has been well written in Ref. [12] and will not be repeated here. The shape of the electron spectum for allowed transition is given by

$$P(KE) = \frac{G_F^2}{2\pi^3}C(KE)p_e KE(Q-KE)^2F_0(Z,KE), \tag{2}$$

where KE is the kinetic energy, G_F is a Fermi constant, C(KE) is the shape function (involves for example the nuclear matrix element) and $F_0(Z,KE)$ is the Fermi function [15]. Forbidden decays can differ from this shape. For example in the electron capture rate calculation by Martínez-Pinedo et al., it was concluded that the shape factor for forbidden decay can change the branching ratio, which could lead to a factor of $4-10$ difference in the astrophysical electron capture rate [1]. To determine the transition strength of the β decay transition integration over the electron energies must be made as follows

$$\lambda = \int_{m_e c^2}^{Q} P(KE)dKE. \tag{3}$$

[12, 15]

For β decay a comparative half-life value, know as ft-value, can be used for easier way of comparing the probabilities of β decay of different nuclei. The ft-value can be calculated as

$$ft = f\frac{t_{1/2}}{b.r.}, \tag{4}$$

where $t_{1/2}$ is the half-life of the nucleus and $b.r.$ is the branching ratio of the transition of interest. For an allowed transition the decay rate can be calculated as follows

$$ft = \frac{C}{B(F) + B(GT)}, \tag{5}$$

where the constant C is 6144.2(16) s, $B(F)$ is the Fermi strength of the transition and $B(GT)$ is the Gamow-Teller strength of the transition [16]. The ft-value for forbidden decay is inversely proportional to the decay strength. Therefore the ft-value for the second-forbidden, non-unique transition between 0^+ state and 2^+ state can be calculated as $ft = C/B(transition)$, where $B(transition)$ is the strength of the transition[13]. The ft-value is usually given in a form of a $\log(ft)$-value and gives a good indication of the transition type (superallowed transitions have the smallest values and forbidden decays have the biggest values). There are only around 27 known second-forbidden ($\Delta J = 2$) non-unique β transitions with known ft-values [17]. In this work, we have determined one more, namely the ground state β decay of ^{20}F.

The experimental preparations described in this thesis work lead towards the experimental determination of the branching ratio of the second-forbidden transition between the ground states of ^{20}F and ^{20}Ne. The β^- decay of ^{20}F proceeds mainly to the first excited state ($J = 2^+$) as seen on the decay scheme in Fig. 5. However a small part of the ^{20}F decays straight to the the ground-state ($J = 0^+$) of ^{20}Ne. For this transition to the ground-state only an experimental upper limit (meaning that at this accuracy nothing was detected so the transition strength must be smaller) has been determined which was $\leq 10^{-5}$ [2]. The transition from the ground-state of ^{20}F to the ground-state of ^{20}Ne is a second-forbidden ($\Delta J = 2$ and $\Delta\pi = no$), non-unique β decay. The Q_β value for the decay to the first excited state is 7024.467(0.030) keV [11] while to the ground-state the Q_β value is 5390.86(8) keV [18] and the half-life of the ^{20}F is 11.163(8) s [19]. However a recent study determined the half-life of ^{20}F again and got a result of $t_{1/2} = 11.0011(69)_{stat.}(39)_{sys.}$ s [20]. This has a difference of 17σ to the previous value but the overall impact on the ft-value is small.

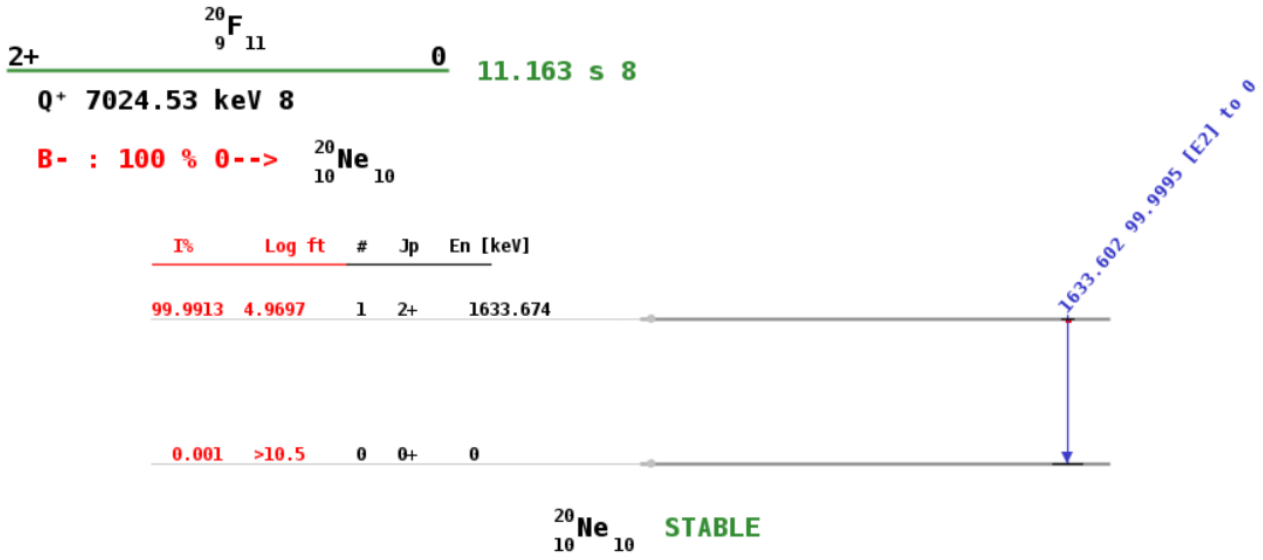

Figure 5. The decay scheme of ^{20}F. Only the lowest levels of ^{20}Ne are included. [19]

3 Experimental methods

The following chapter gives a detailed description of the experimental methods used to produce ^{20}F ions and to detect its β decay in this work. The β decay of ^{20}F was studied with a spectroscopy setup which was built at the spectroscopy line of the IGISOL facility. The setup consisted of a Siegbahn-Slätis intermediate-image spectrometer with its vacuum and high voltage power supply system, two scintillator detectors and a Caen DT5724 data acquisition system.

3.1 IGISOL facility

The ion guide isotope separator on-line (IGISOL) facility is located at the Accelerator Laboratory of the University of Jyväskylä. The ion guide technique was first developed in the 1980's at Jyväskylä and since then has been adopted at many other facilities as well [21, 22]. The layout of the IGISOL facility is presented in Fig. 6. At the IGISOL facility the beam can be provided by the K130 cyclotron or MCC30 cyclotron. For the ^{20}F β decay experiment, beam from K130 was employed. An off-line ion source is located on the second floor of the IGISOL facility and is used during the cooling down times of the IGISOL front end [23]. Here the cooling down time refers to the time it takes for the activity of the front end to decreases to a safe level for a human to enter and work at the area.

The beam from the cyclotron is delivered to the ion guide of IGISOL where it impinges into a thin target foil, where a typical thickness of the foil is a few mg/cm^2. The light-ion ionguide is marked as number 3 on Fig. 6 and can also be called IGISOL front end. In a thin target the reaction products have enough recoil energy that they can pass through the target material into the gas cell. Inside the target chamber a highly purified helium gas with typical pressures around $100 - 300$ mbar is flowing through the system to stop and thermalize the reaction products. The collisions between the reaction products and helium atoms or impurities cause charge exchange reactions leading to a high amount of singly-charged ions. The helium flow guides the ions towards the extraction and the ions are extracted out of the gas cell using a sextupole ion guide (SPIG). The affect of the different SPIG radiofrequency coils on the ^{20}F beam production was measured and is discussed in chapter 5.1. A more detailed describtion of the SPIG system is described

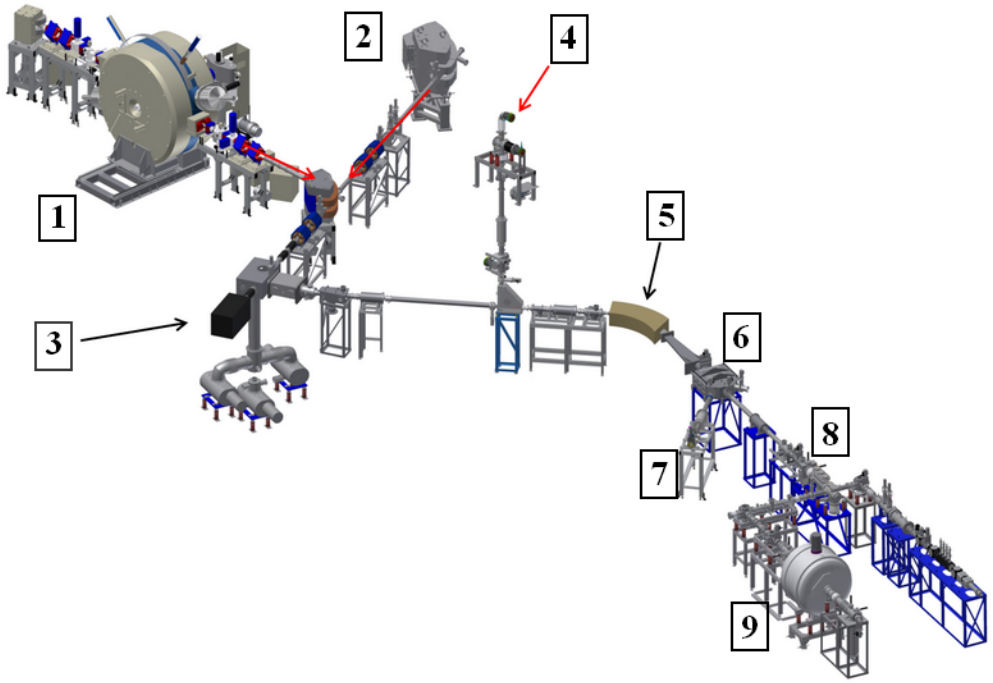

Figure 6. A schematic layout of the IGISOL facility. The elements are numbered as follows: 1) MCC30 cyclotron, 2) beam line from K130 cyclotron, 3) light-ion ionguide, 4) off-line ion source, 5) 55° dipole magnet 6) switchyard 7) spectroscopy line 8) cooler/buncher and 9) JYFLTRAP. The collinear laser spectroscopy beam line continues on the left side of the cooler/buncher line when looking from the direction of the beam.

in P. Karvonen's PhD thesis work [24, 25]. The extracted ions are accelerated to 30 keV and undergo a mass separation at the 55° dipole magnet based on their mass to charge ratio (m/q). The mass resolving power is around 300 which is high enough to separate neighbouring mass numbers.

The mass-separated beam can be directed by kickers and deflectors to three different directions at the switchyard (Fig. 6 number 6): the spectroscopy line (7), the cooler/buncher line (8) or the ^{135}Cs atom trap line. The cooler/buncher line is further divided to a collinear laser spectroscopy line or the JYFLTRAP Penning trap line (9). In our experiment the beam was directed from the switchyard (SW) to the spectroscopy beam line. To turn the beam from SW to the spectroscopy line one needs to apply a voltage of 3705 V on the right kicker and apply voltages of ±825 V to the right deflector. The beamline was tuned using stable ^{20}Ne beam on Faraday cups at the beamline. ^{20}Ne is present in the in-house helium used in the ion guide, and it is ionized by the primary beam entering the gas. The spectroscopy beamline has XY steerers and einzel lenses to control the size and position of the beam. At the end of this beamline a spectroscopy setup consisiting of a

spectrometer and two detectors was placed to measure the second-forbidden, non-unique, transition.

3.2 Experimental setup at the spectroscopy line

The full spectroscopy setup is shown in Fig. 7 and the connection to the IGISOL beam line is shown in Fig. 8. A wide range of GEANT4 simulations were performed for the spectroscopy setup but are not included in this thesis work. The data-analysis was done after the online measurements using the ROOT data-analysis software [26].

The strength of the second-forbidden, non-unique, ground-state to ground-state transition between ^{20}Ne and ^{20}F was determined from the branching ratio of the inverse transition in the β decay of ^{20}F. The ^{20}F decays via β decay mostly to the first excited state of ^{20}Ne as shown in the decay scheme of ^{20}F in chapter 2.3. The β decay to the first excited state dominates the β spectrum until the energy of $E_\beta = 5.4$ MeV. After this the tail of the weak ground-state to ground-state transition can be observed until the end-point energy of (7024.47 ± 0.03) keV [11]. A schematic view of the decay energy spectrum is shown in Fig. 9. The figure also shows the approximately 7 % signal area for the measurement adding challenges to the measurement. [27]

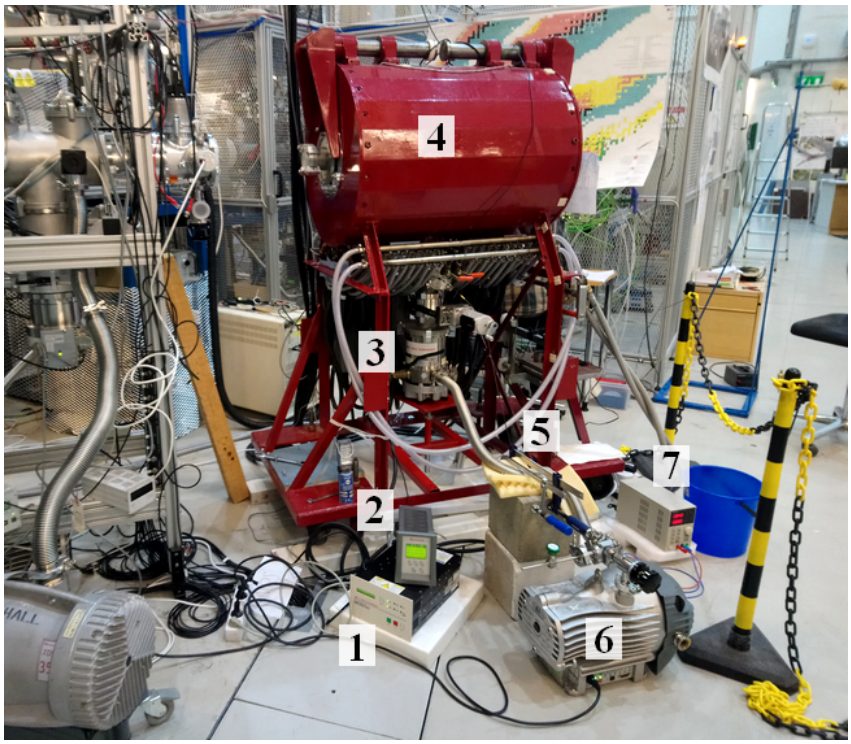

Figure 7. Experimental setup without the beam connection. The parts of the setup are labeled as follows: 1) Edwards turbo pump controller, 2) Edwards gauge controller, 3) Edwards turbomolecular STP451C pump, 4) spectrometer, 5) tied down vacuum tubing to reduce the vibrations of the tube on the carbon foil, 6) Edwards scroll nXDS 6i roughing pump and 7) the $LaBr_3$(Ce) detectors bias supply (Tenma 72-10480).

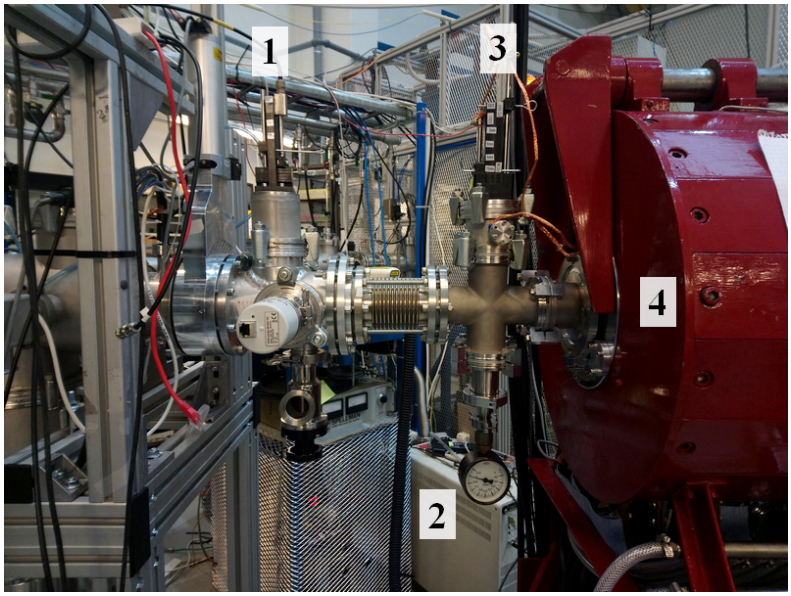

Figure 8. The connection of the spectrometer to the beam line. The parts are numbered as follows: 1) actuator holding a 500 μm thick, 300 mm^2 Si detector and an Al foil system in front of the detector, 2) analog gauge to monitor pressure on the beamline side of the carbon foil, 3) Faraday cup and collimator and 4) the carbon foil position inside the spectrometer.

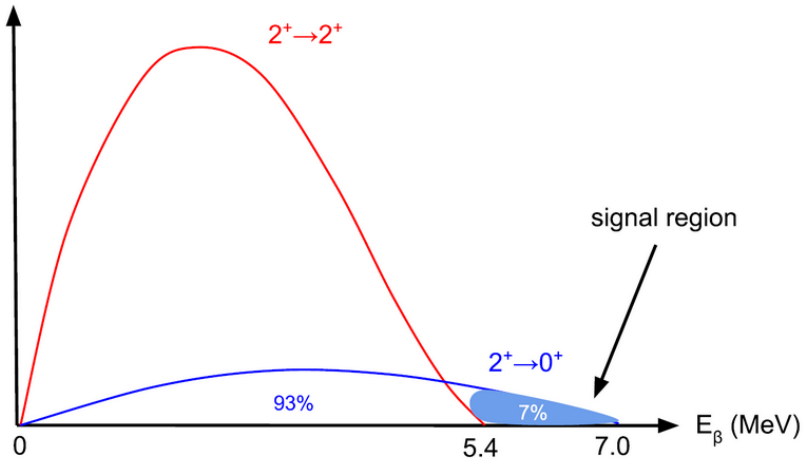

Figure 9. A schematic drawing of the energy spectrum of ^{20}F β decay. The decay to the first excited state is drawn in red when the ground-state to ground-state transition is drawn in blue. The signal area has been marked in lighter blue. [27]

3.3 Siegbahn-Slätis intermediate-image spectrometer

The main part of the spectroscopy setup consists of a Siegbahn-Slätis type intermediate-image spectrometer which is shown in Fig. 10. The measurements previosly done using this spectrometer have been able to bend electrons with energies up to 7−8 MeV [28]. The magnetic field of the spectrometer is created with two coils that are in a Helmholtz type of configuration. This gives the intermediate-image spectrometer an axially symmetric magnetic field and a good focusing effect. Axially symmetric magnetic field bends the electrons so that the electrons are on a spiral trajectory and return to the same axis. The focusing effect can be seen in Fig. 11 where the trajectory of the electrons start from the side labeled source, electrons leave the source at different angles but the magnetic field

Figure 10. The Siegbahn-Slätis type intermediate-image spectrometer used for the experiment. From the side two iron covers have been removed to reveal the current carrying coils.

bends the electron trajectories to the same spot on the other side of the spectrometer. The magnetic field is created with 18 coils using the configuration (18K) shown in Fig. 12 [29]. The coil configuration was confirmed by comparing a GEANT4 simulation of the magnetic field strength as a function of distance at a certain current setting to the measured magnetic field strength. A detailed description of the results of this measurement are described in section 4.3 where Fig. 35 also shows the shape of the magnetic field achieved with 18K configuration.

A cylindrical iron cover has been built around the vacuum chamber and the coils. In Fig. 10 two of the iron covers (red iron bricks) have been taken away to show the current carrying coils. The iron cover keeps surrounding magnetic fields out of the magnetic field created by the coils and therefore helps to form the axially symmetric field [29]. The maximum magnetic field that can be reached with the spectrometer is around 0.6 T and is located close to the iron doors of the spectrometer. The magnetic field is shaped so that the maximum magnetic fields are at the edges of the spectrometer and the center of the system has a 3.8 times lower magnetic field. To reach the maximum magnetic field the current applied is around 600 A. [28] The current for the spectrometer was provided with a Danfysik System 8000 853T power supply which had a maximum current of 700 A (maximum power was 49 kW and maximum voltage 70 V). The current was controlled with a Danfysik control panel where the current was stated in I/I_{max} [%]. The relation between the magnetic field value and the set current of the coils was $I/I_{max} = 141.0 \cdot B_{max}$, where I/I_{max} is the precentage needed of the maximum current to provide a magnetic field maxima B_{max} inside the spectrometer. This relation was determined by comparing a ^{207}Bi source measurement with a GEANT4 simulation.

The coils where the current runs are shaped rectangular and have cooling water flowing through them. During the testing of the spectrometer leaks of the cooling water from the plastic tubing could be seen. This has to do with the plastic tubing being hard to connect and tighten with the rectangularly shaped coils. Measures to collect the leaking cooling water were made. If using the maximum current the cooling water temperature should be under 25° C and have a circulating speed of at least 10 l/min [29].

In the beginning of the testing of the spectrometer, the vacuum was created with three pumps: Edwards scroll nXDS 6i roughing pump and two different turbo pumps (Edwards turbomolecular STP451C and Pfeiffer HiCube80). Using all three pumps a vacuum of 10^{-6} mbar could be achieved. During the May 2017 test experiment it was noticed that one of the turbo pumps (Pfeiffer HiCube80) could be left out, because vacuum of $10^{-5} - 10^{-6}$ mbar could be reached with only a roughing pump and one turbo pump. The roughing pump could reach a pressure of 10^{-2} mbar and afterwards the turbo pump could

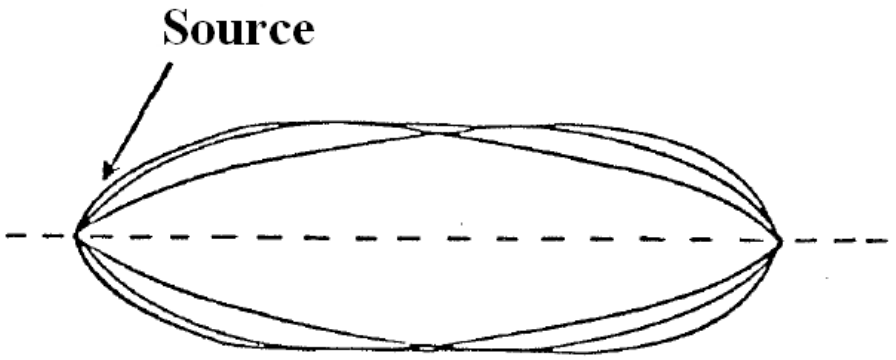

Figure 11. A schematic view of the electron trajectories affected by the focusing effect of the spectrometer [29].

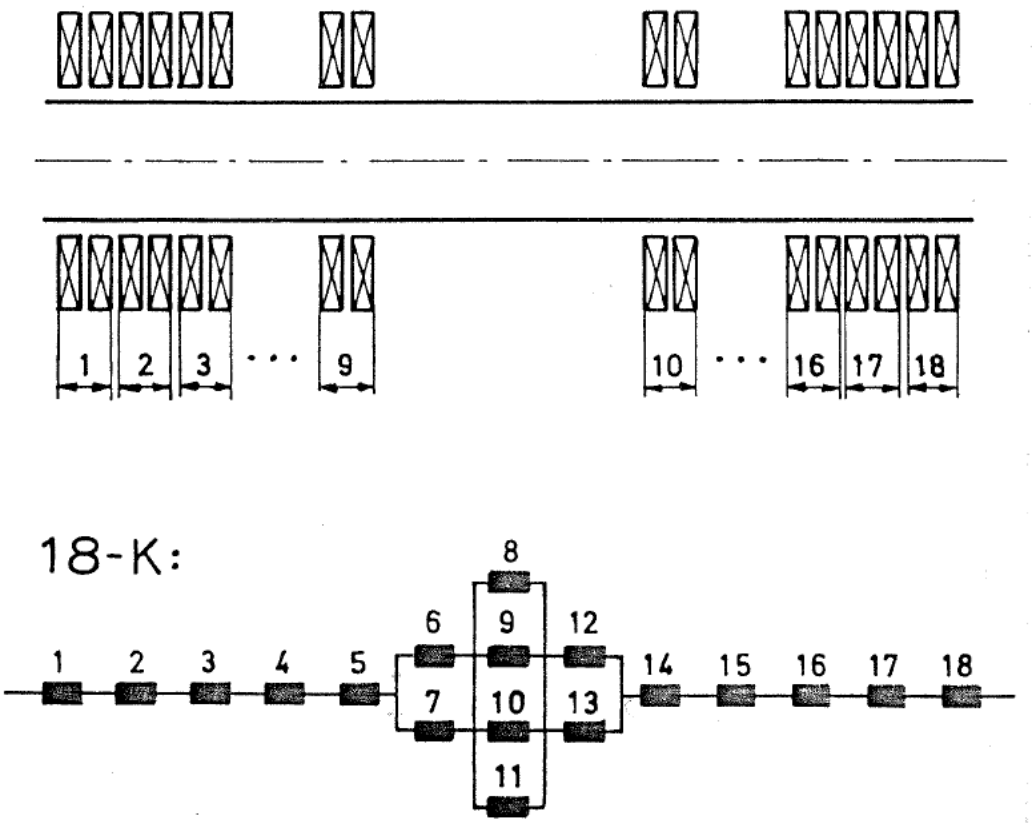

Figure 12. The numbering of the coils located inside the spectrometer and the 18K coil configuration [29].

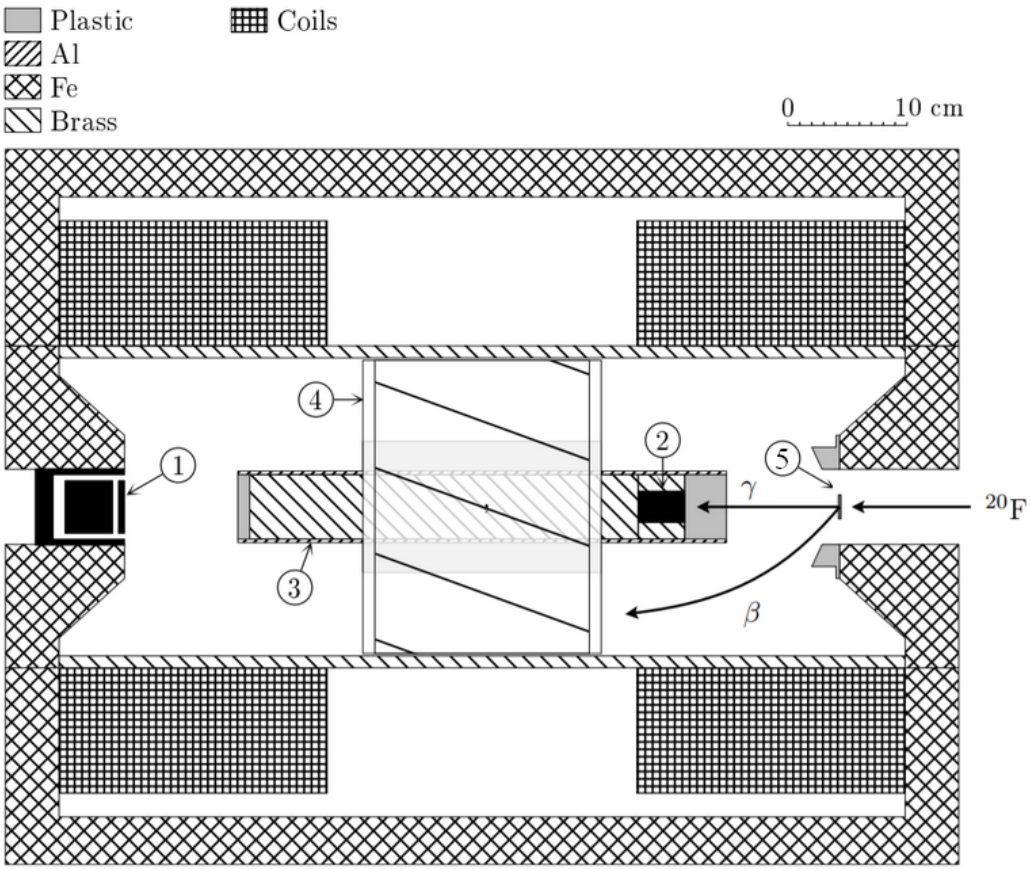

Figure 13. A schematic drawing of the spectrometer. Important parts of the setup are numbered as follows: 1) Scionix plastic scintillator detector, 2) $LaBr_3(Ce)$ detector, 3) brass shield, 4) positron baffle and 5) carbon foil. The drawing is modified from [30].

be turned on to reach a pressure of 10^{-6} mbar. If either end of the spectrometer had been opened, reaching the vacuum required physically pushing the ends of the spectrometer. After this the spectrometer kept the vacuum rather well.

The ^{20}F beam was stopped on a 51 μg/cm^2 thick carbon foil that is located at the entrance of the spectrometer and is labeled with number 5 on Fig. 13. The carbon foil is attached to an aluminium holder and to prevent the beam from getting above or under the holder a collimator is attached to the beamline in front of the spectrometer. The electrons emitted to a large angle were noticed to hit and scatter from the walls of the vacuum chamber of the spectrometer and with the use of GEANT4 simulations and measurements made with ^{207}Bi source it was decided that a plastic shielding at the starting angle would be needed. The plastic shield was placed close to the carbon foil to the iron door of the spectrometer and is at a 65° angle.

Figure 14. The positron baffle used around the shield. The electrons bend due to the magnetic field to the direction where they go between the Al plates when positrons bend to the other way hitting and stopping into the Al plates.

In the middle of the spectrometer at the centre axis a brass shield is placed (number 3 in Fig. 13). The brass shield is covering the Scionix detector (number 1 in Fig. 13) from for example the γ-rays emitted in the de-excitation of the first excited state in ^{20}Ne. This eliminates the $\beta\gamma$ summing that would happen if the γ-rays reached the detector. The shield also holds the $LaBr_3$(Ce) detector (number 2 in Fig. 13). Around the shield we placed a helical positron baffle. The baffle is shown in Fig. 14 and the shape of the baffle was designed so that it would let the electrons through but the positrons, that are bent to a different direction due to the magnetic field, hit the baffle. The baffle had a 11 % reduction of the electron flux on the Scionix detector in the experiment done in January 2018. In the test measurements done in May 2017 the positron baffle was not used.

3.4 Detectors

3.4.1 Scintillator detectors

A scintillator detector consists of scintillating material and a device to convert the light to an electrical signal. The ionizing particle hitting the scintillator material, called the incident radiation, undergoes many interactions while exciting the atoms of the scintillating material. When the excited states of the scintillation material de-excite visible light is emitted (low-energy photons). The light travels through the scintillator material to the surface where a photosensitive surface of for example a photomultiplier tube or a silicon photodiode is placed. This creates photoelectrons that are multiplied when hitting the dynode of the photomultiplier tube and accelerated with the electric field of the photomultiplier tube. This cascade of electrons formed with the photomultiplier tube are called secondary electrons, and they are different electrons than the ones released in the ionization of the scintillator material. The output signal can be then read with different electronic equipment from the anode of the photomultiplier tube. [12]

Different scintillator detectors have been used since 1950s. When choosing the scintillator material for a scintillator detector the most important qualities that need to be taken into account are the light output of the scintillator material, the efficiency needed for the detection, timing and energy resolution needed from the detector. The light output of a scintillator material has to have a high yield and the material has to be transparent towards its fluorecence light so that the emitted light is not absorbed into the material itself. The efficiency depends on how well the material absorbs the radiation and can be modified by choosing a correct size, for example the correct thickness to stop the radiation, and correct density of the scintillating material for the radiaiton type that is wanted to be detected. The timing aspect of the scintillating material is taken into account when for example a short decay time reduces the dead-time of the detector and gives a possibility for a high count rate measuring. [12, 31]

The scintillator detectors can be divided into two basic types: the detectors that are composed of organic scintillating material and those composed of inorganic scintillating materials. In detectors where the scintillator material is composed of organic material the photon emission happens because of the transitions of electrons between molecular orbitals in single molecules. For this reason the organic scintillators are know to have fast decay times (ns). The incident radiation excites both electron and vibrational levels of the molecule as shown in Fig. 15 where the singlet states (spin 0) and triplet states (spin 1) are marked. It is to be noted that the lifetime of a triplet state is longer than

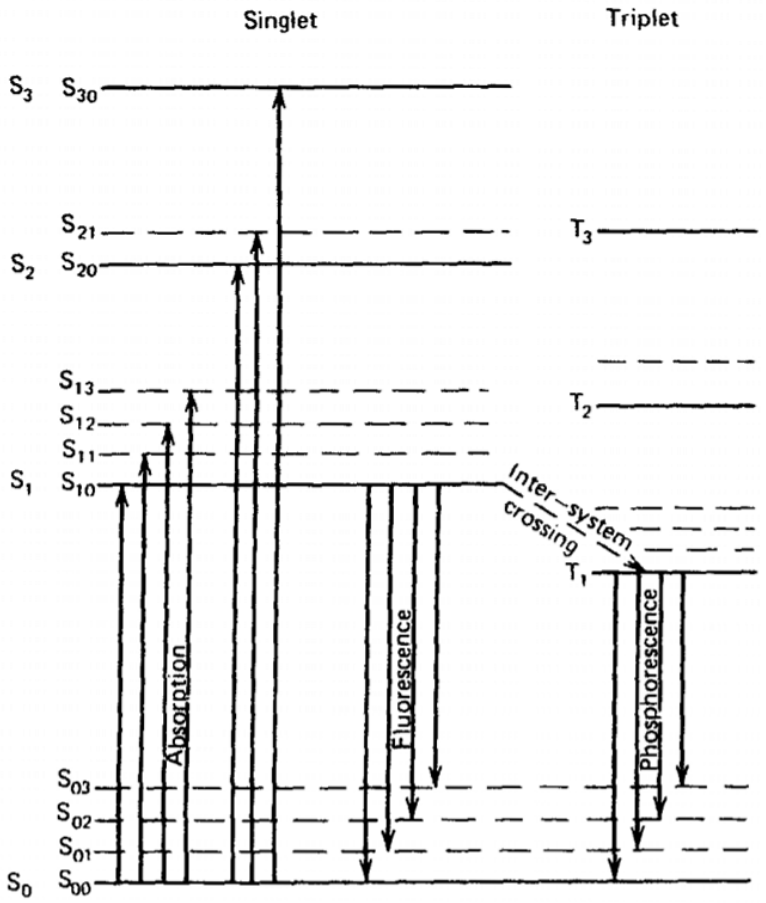

Figure 15. An example of the molecular orbitals and the scintillation principle in organic scintillators. [33]

a lifetime of a singlet state, leading to delayed light emission. Organic scintillators can be organic crystals (for example anthracene), organic liquids (PBD[2], PPO[3]) or plastic (polyvinyl toluene). [14]

In our experiment a Scionix plastic scintillator was used for β detection and a more detailed description is given in chapter 3.4.2. Plastic scintillators are easily cut into desired shape and they are relatively cheap while still having a high light output. To stop the 7 MeV energy electrons from the second-forbidden, non-unique transition between the ground states of ^{20}F and ^{20}Ne, a Si-detector would need a 17 mm thick layer of silicon when plastic scintillating material is needed a 35 mm thick layer [32]. Silicon is much more expensive material especially compared to plastic scintillators. Therefore, a plastic detector was used for practical reasons.

In inorganic scintillators the photon emission happens usually because of the combined effect of the crystal lattice and added activator. The activator is a small amount of im-

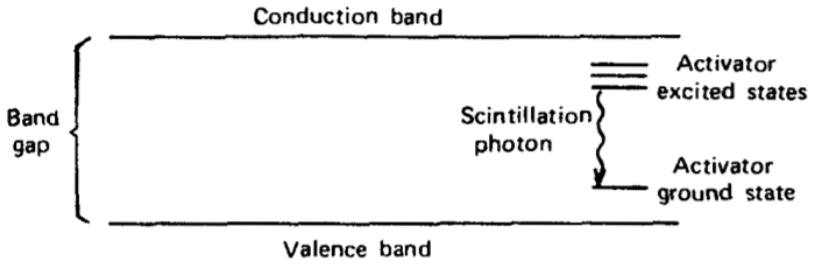

Figure 16. A schematic figure of the crystal lattice and the scintillation principle in inorganic scintillators. [34]

purity which is added to the crystal causing modifications in the band gap and energy structure of the crystal. This improves the probability of the photon emission and reduces the self-absorption of the light. In Fig. 16 a schematic of the energy band structure of an inorganic scintillator is shown. Incident radiation will elevate an electron to the conduction band from the valence band, and due to the activator the electron de-excites back to the valence band through the activator states emitting visible light [34]. The inorganic scintillators are usually slower by $2-3$ orders of magnitude than organic scintillators. A clear benefit of an inorganic scintillator is the high light output which gives the best energy resolution of all the different scintillator detectors. This leads to inorganic scintillators being a suitable solution for γ-ray detection. Some examples of used inorganic scintillators are NaI(Tl), CsI(Tl) and $LaBr_3$(Ce). [12, 14] In our experiment the used inorganic scintillator detector had a $LaBr_3$ crystal doped with Ce and combined with a Silicon photomultiplier (SiPM). The characteristics of this detector have been described in detail in section 3.4.3.

3.4.2 Scionix plastic scintillator

Figure 17. The Scionix detector mounted on its holder and a black cover covering the entrance window from light.

For the β detection a Scionix plastic scintillator detector was used. During most of the tests measurements and the test beam time described in chapter 5.2 a Scionix detector version 1.0 was used. This detector had an inner (called signal) and outer (called VETO) plastic scintillator detectors. The signal detector was a Scionix EJ200 plastic scintillator which had a diameter and height of 45 mm. This detector was used for detecting the electrons coming from the source. The VETO detector was also made of a Scionix EJ200 plastic scintillator but had a diameter of 55 mm and a height of 75 mm. The VETO detector was built with an axial well which was 60 mm deep and had a diameter of 46 mm. The signal detector was fitted inside of this axial well. The thickness of the VETO detector is 5 mm. In Fig. 17 the Scionix v.1.0 is shown with the holder system that lines the Scionix detector to the correct position at the edge of the spectrometer's iron door. A schematic diagram of the Scionix v. 1.0 detector is given in Fig. 18a. The second Scionix detector was built after testing the v.1.0 and realizing there was still room for improvement on the rejection of background radiation.

The Scionix plastic scintillator version 2.0 was built in a similar way than v.1.0 of Scionix EJ200 plastic with the same measurements except the signal detector was divided into

two parts: 5 mm thick front part and a 40 mm thick main detector part. A schematic view of the Scionix v. 2.0 is shown in Fig. 18b. The readout from all of the scintillators in both Scionix v.1.0 and v.2.0 are done with silicon photomultipliers (SiPM). The entrance window of the detector is made of aluminized mylar with a thickness of 6 μm. The Scionix detector has been designed so that a significant amount of the electrons with maximum energy of 7.024 MeV will be stopped in the plastic when at the same time the cosmic background radiation exposure is kept to a minimum.

With the Scionix v.1.0 the background radiation reduction was conducted as follows: when a count on the VETO detector could be seen in coincidence with the signal detector the count from the signal detector was discarded. The approach with the VETO detector on the Scionix v.2.0 was the same, but now also an $\Delta E - E$ cut between the front and signal detectors could be added.

The SiPM's inside of the Scionix detector were biased with an overvoltage of 5 V, which was provided through a voltage regulator biased at 6 V from HQ P.SUP.EU1500 universal AC/DC plug-in adapter. The signal from front, signal and VETO detectors were brought to Caen DT5724 digitizer, where settings for each detector were optimized. The configuring of the settings of Caen MC^2 analyzer has been described in more detail in the next section. Measurements made to characterize the Scionix plastic scintillator detectors are discussed in detail in chapter 4.1.

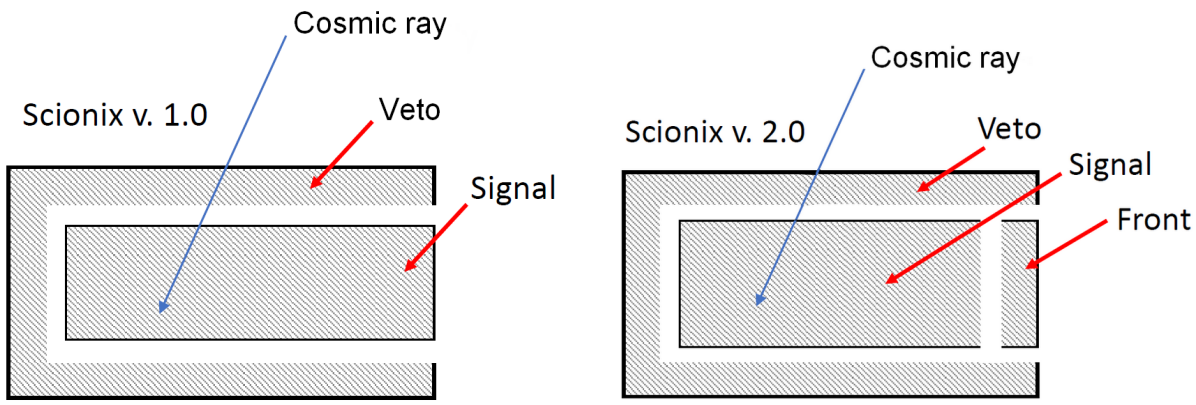

(a) The Scionix plastic scintillator v. 1.0 consisting of the signal and the VETO detector.

(b) The Scionix plastic scintillator v. 2.0 consisting of the front, the signal and the VETO detector.

Figure 18. Schematic diagrams of the Scionix plastic scintillator detectors v. 1.0 and v. 2.0.

3.4.3 $LaBr_3$(Ce) detector

Figure 19. The $LaBr_3$(Ce) detector out of the brass shield.

The monitoring of the γ-rays from the decay of the first excited state was done with a cerium-doped $LaBr_3$ scintillator detector. A $LaBr_3$(Ce) scintillator detector is promised to have a good energy resolution with a good linearity [35]. The dimensions of the $LaBr_3$(Ce) crystal were 25.5 mm of diameter and 38.5 mm of length. The $LaBr_3$(Ce) crystal was coupled with a SiPM because the detector would reside inside a magnetic field. The SiPMs are not affected by the magnetic field. The $LaBr_3$(Ce) scintillator detector was placed inside a brass shield that is described in section 3.3. The γ-ray spectrum measured could be used for the absolute normalization of the β spectrum and for monitoring the beam rate at the experimental setup during the experiment (this was done by monitoring the γ-ray rate). When placing the brass shield with the detector inside the spectrometer the $LaBr_3$(Ce) detector was 13 cm away from the implantation site.

The efficiency of the $LaBr_3$(Ce) detector was measured to be $(4.77 \pm 0.18) \cdot 10^{-5}$ at 1.6 MeV. The determination is described in chapter 4.2. The resolution (FWHM) was measured to be (3.31 ± 0.02) % and is described in detail in chapter 5.2. The $LaBr_3$(Ce) detector was biased with three different power supplies during the testing of the setup and the experiment. During the first tests the power supply was a Iseg NHS 6001p power supply, during the test experiment described in chapter 5.2 it was an Ortec 428 bias supply and during the experiment described in chapter 5.3 it was a TENMA 72-10480 power supply.

When measuring a γ-ray spectrum for example of a ^{152}Eu source three peaks can be seen between $2 - 3$ MeV (chapter 4.2 Fig. 34). These peaks are because of the internal properties of the $LaBr_3$ crystal arising from the presence of ^{138}La and ^{227}Ac in the crystal.

3.5 Data acquisition and analysis software

Figure 20. The 4-channel Caen DT5724 digitizer used for data acquisition.

The signal from the Scionix detector and the $LaBr_3(Ce)$ detector was converted into digital form with the Caen 14 bit DT5724B 4 channel Desktop Waveform digitizer [36]. The Caen digitizer was used with the Multi-Channel (MC^2) analyzer program provided by Caen. In MC^2 analyzer different settings for each channel could be set and this is described in more detail later in this chapter. During most of the testing and the whole experiment channels 0, 1 and 3 were occupied with signals from Scionix detector while the channel 2 was used for $LaBr_3(Ce)$ detector.

A block diagram of how the Caen digitizer is used in a spectroscopy system is shown in Fig. 21. In our case the detector was a scintillator detector and in the place of the charge sensitive preamplifier we had SiPMs. The SiPMs make the signal from the detector into an electronic signal. The signal is fed to the digitizer where the pulse shaping and

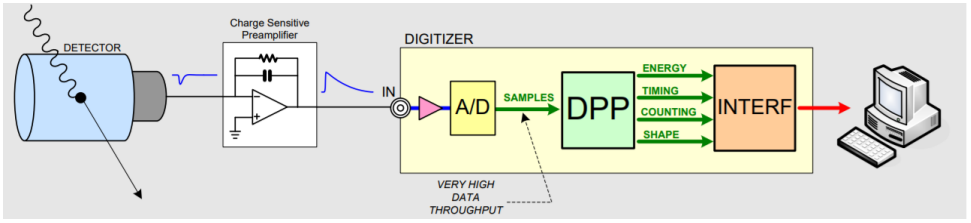

Figure 21. A block diagram how the Caen digitizer is used in a spectroscopy system [37].

amplification, digitizing the height of the pulses, filling a histogram with the correct values and the timing information are handeled. From the digitizer the information is transferred to a computer and MC^2 analyzer program via USB. [37] A general interface of the MC^2 analyzer is shown in Fig. 22.

The configuration of the most important settings for each detector in the MC^2 analyzer program are described here briefly. An example of the configuration of the settings is shown in table 5 which has the optimal configuration of settings for the measurement done in January 2018 (chapter 5.3). The modification of the settings can be started in MC^2 analyzer after connecting the digitizer with the MC^2 program. The configuration of the settings are made for each channel individually by choosing a channel in the "Signal Inspector" window. The signal inspector opens a tab where different analog and digital traces can be visualized. The vizualized traces are chosen accordingly to the different filters that are changed. The correct vizualizations are described in more detail in the user manual of MC^2 [37]. The changing of the settings happens while the vizualization is on from the Acquisition Setup.

First the "Input signal" settings are defined. In the digitizer model DT5724 the "Input Range" setting is not available. The "Decimation" and "Digital Gain" setting were also kept in number 1 as they were default settings for the digitizer. After these the polarity

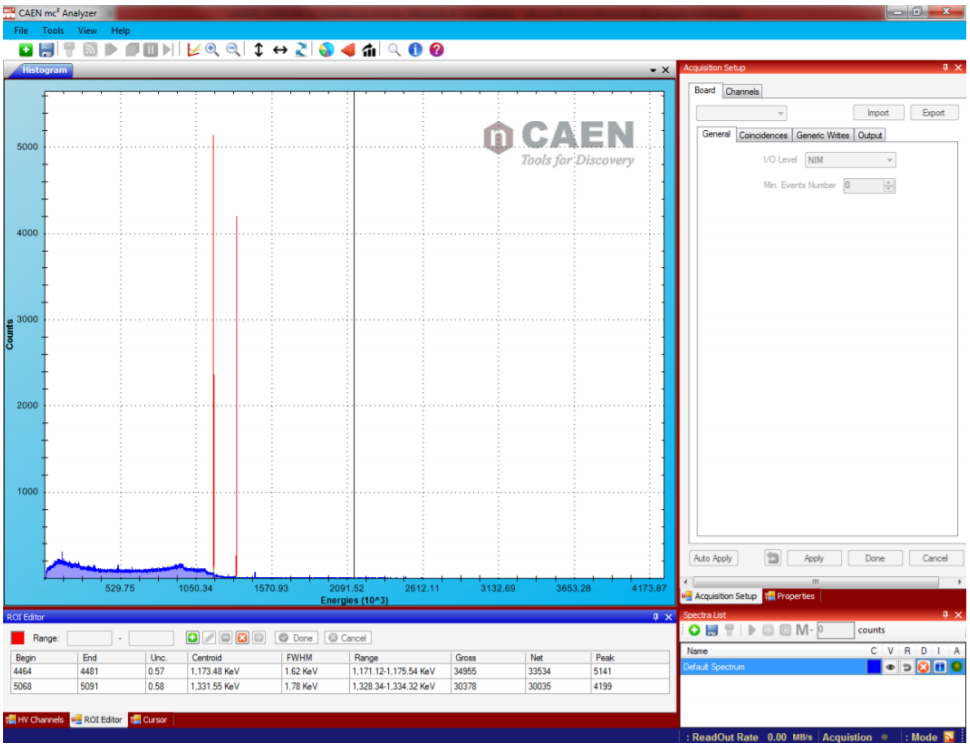

Figure 22. A general interface of the MC^2 program [37].

of the pulse can be chosen depening on the detector. The Scionix detector had a negative pulse polarity for each of the channels when the $LaBr_3(Ce)$ had a positive pulse polarity.

After the input signal filter is set, the trigger filter can be configured from the trigger tab. First the "RC-CR^2 Smoothing" factor needs to be defined because all of the other setting on the trigger tab are set accordingly to this smoothing factor. This factor defines a number of samples that are used for the formation of the RC-CR^2 signal. We have chosen a smoothing factor of 16 as instructed in the user manual [37]. A setting called "Input Rise Time" is supposed to be set to have the same height as the RC-CR^2 signal and the input pulse. After this the "Trigger Hold-Off" setting can be adjusted to avoid triggering on the over- or undershooting of the RC-CR^2 signal. The value needs to be adjusted so that it includes the overshoot or undershoot inside it as shown in Fig. 23. The setting called "Threshold" is set just above the noise level of the RC-CR^2 signal.

Next an energy filter needs to be set from the Energy Filter tab. Two of the most important aspects of setting the energy filter are to make sure that the trapezoid is shaped correctly and that the energy value of the flat top region of the trapezoid is correct. The first task is to approximate a value for the "Decay time" setting which is determined from half-time of the input signal. The decay time is then calculated as $\tau = T_{1/2}/\ln 2$, where $T_{1/2}$ is the half-life. Then a value for the rise time of the trapezoid can be given. A smaller trapezoid rise time will help to reduce the pile-up but will not give as good of a resolution as a larger value would. In our case it is important to

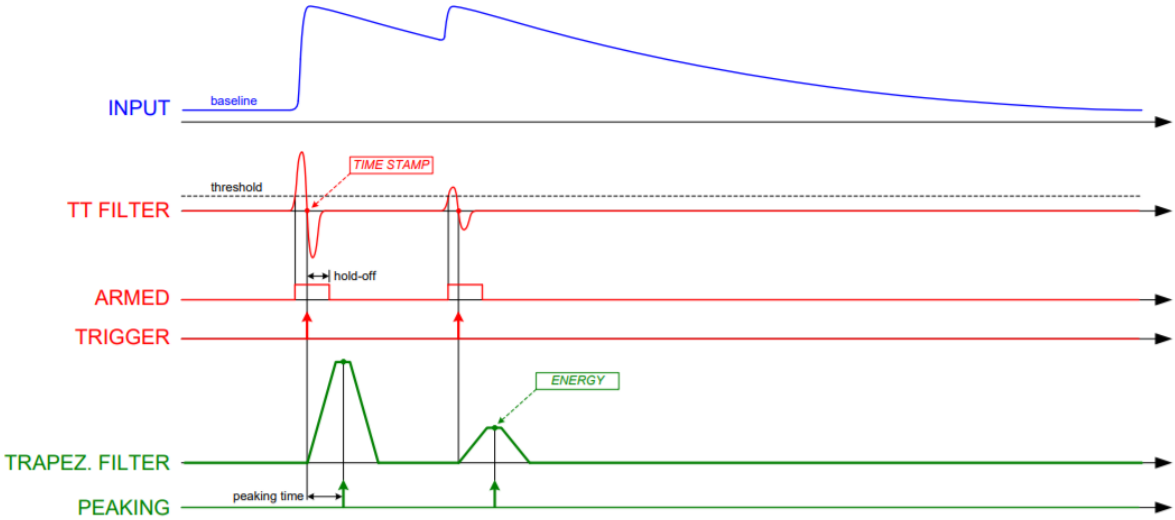

Figure 23. A schematic view of the trigger and energy filters. In blue the input signal is given after the preamplifier (in our case SiPM), next in red the trigger filter is shown and last in green the energy filter (called also trapezoid filter) is shown. [37].

reject the pile-up when measuring the β spectrum, making the "Trapezoid Rise Time" value a compromise between the resolution and pile-up rejection. The "Trapezoid Rise time" is set to 4 μs for the Scionix plastic scintillator detector when for the $LaBr_3(Ce)$ detector we could use a longer time of 7 μs. The height of the flat top of the trapezoid is proportional to the amplitude of the input pulse. It is important to check that the top of the trapezoid is actually flat so that the peaking position and the number of samples for energy calculation are taken from a flat point of the trapezoid. In our case the "Trapezoid flat top" setting was 1.50 μs. Next on the energy filter the resolution settings in our case were done manually (setting: Man) but the MC^2 analyzer program also offers default settings for different cases (HiRes, Bal, HiRate). More detailed instructions of defining all of the settings is given in the user manual of MC^2 analyzer [37].

The final analysis of the collected data was done with the ROOT data analysis software that was developed in CERN and is mainly written in C++.

4 Testing the experimental setup

4.1 Scionix plastic scintillator

4.1.1 Test measurements with a ^{207}Bi source

The Scionix plastic scintillator detector was tested using a ^{207}Bi source (JYFL-91). The activity of the source was (397 ± 11.910) kBq on 15.12.2008. More detailed information of the decays and emitted particles from the ^{207}Bi source are given in table 2 [38]. The shape of the β-decay spectrum is explained in chapter 2.3. The source was placed on a source holder shown in appendix I Fig. 2. The source holder was designed so that the source was at the same position as the carbon foil which was used to stop the 30 keV ^{20}F beam. Most of the measurements done with the ^{207}Bi source were made inside the spectrometer so that the electrons could be bent with the magnetic field of the spectrometer and also so that the shield inside the spectrometer would cover the Scionix detector from the emitted γ-rays of the source.

The ^{207}Bi source was used to test the magnetic field of the spectrometer (for example the transmission of the spectrometer), to get an idea of the efficiency of the Scionix detector, to optimize the settings on MC^2 analyzer and to validate the GEANT4 simulations of the setup. The ^{207}Bi source was also used to make an energy calibration for the Scionix scintillator detector.

Changing the magnetic field strength a different part of the electron spectrum of ^{207}Bi could be measured. In Fig. 24 three different measurements with three different magnetic field strength settings are shown. Measurements in both Figs. 24 and 25 were made with Scionix v.2.0 detector. The magnetic field strength was chosen so that the measurements would focus around the electrons emitted at the energy of 975 keV which have the highest decay intensity. Each of the measurements are 1 minute in duration or scaled to 1 minute. As seen in the figure we are scanning "through" the 975 keV area: at $I/I_{max} = 11$ % the electron spectrum is starting to show, at $I/I_{max} = 14$ % we are at the highest part of the electron spectrum and at $I/I_{max} = 17$ % we have nearly passed the 975 keV part and see the end-tail of the spectrum.

The measurement made with the magnetic field strength setting of $I/I_{max} = 14$ % shows a clear part of the electron specturum but around 1900 keV a clear excess of counts can be

Table 2. Details of the transitions in ^{207} Bi source [38].

E_γ (keV)	$I_\gamma(\%)$	$E_{electron}(keV)$	I_{exp} (%)
569.702	97.75	481.697 (K)	(1.562 ± 0.03)
		554.4 (L)	(0.469 ± 0.011)
1063.662	74.09	975.657 (K)	(7.17 ± 0.17)
		1048.1 (L)	(0.469 ± 0.011)
1770.237	6.868	1682.232 (K)	(0.0237 ± 0.0015)
		1754.4 (L)	(0.0038 ± 0.0004)

seen. This is a result from pile-up when two electrons of the same energy hit the detector at the same time and are counted as one. The pile-up can be dealt with optimizing the settings on MC^2 analyzer for example making the "Trapezoid Rise Time" value smaller. The configuration of the MC^2 analyzer settings is described in detail in chapter 3.4.

Figure 25 shows mesurements with three different magnetic field strengths focusing on the electrons around the 1682 keV energy region. All of the measurements were 5 minutes in duration because the intensity of the decay is not as high as in the 975 keV region (see table 2). Here, because the intensity is lower than in the case of 975 keV electrons, we do not see any pile-up. With different magnetic field strength setting the measurement goes through the spectrum and comparing these measurements to GEANT4 simulations with certain settings we can confim that the spectrometer and the simulations are working correctly at least untill energies of 2 MeV.

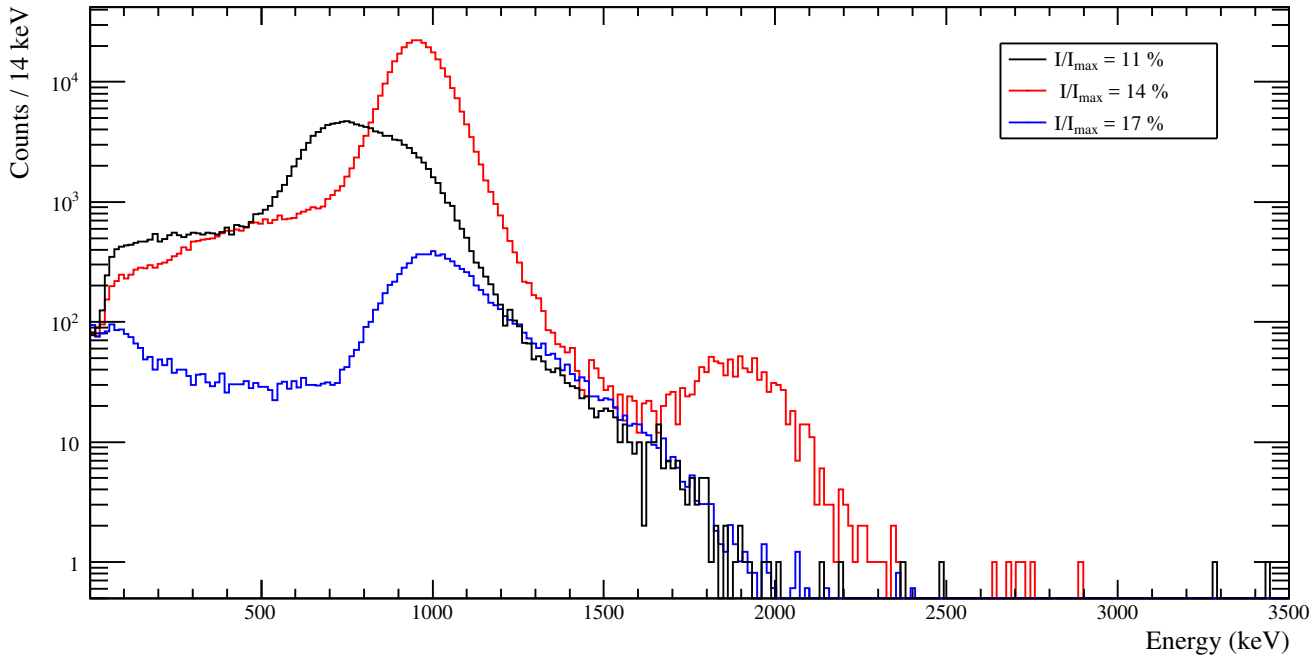

Figure 24. Electron spectrum of ^{207}Bi source around 975 keV area measured with the Scionix v.2.0 detector. The duration of the measurements were 1 minute. The VETO or $\Delta E - E$ cut has not been enabled.

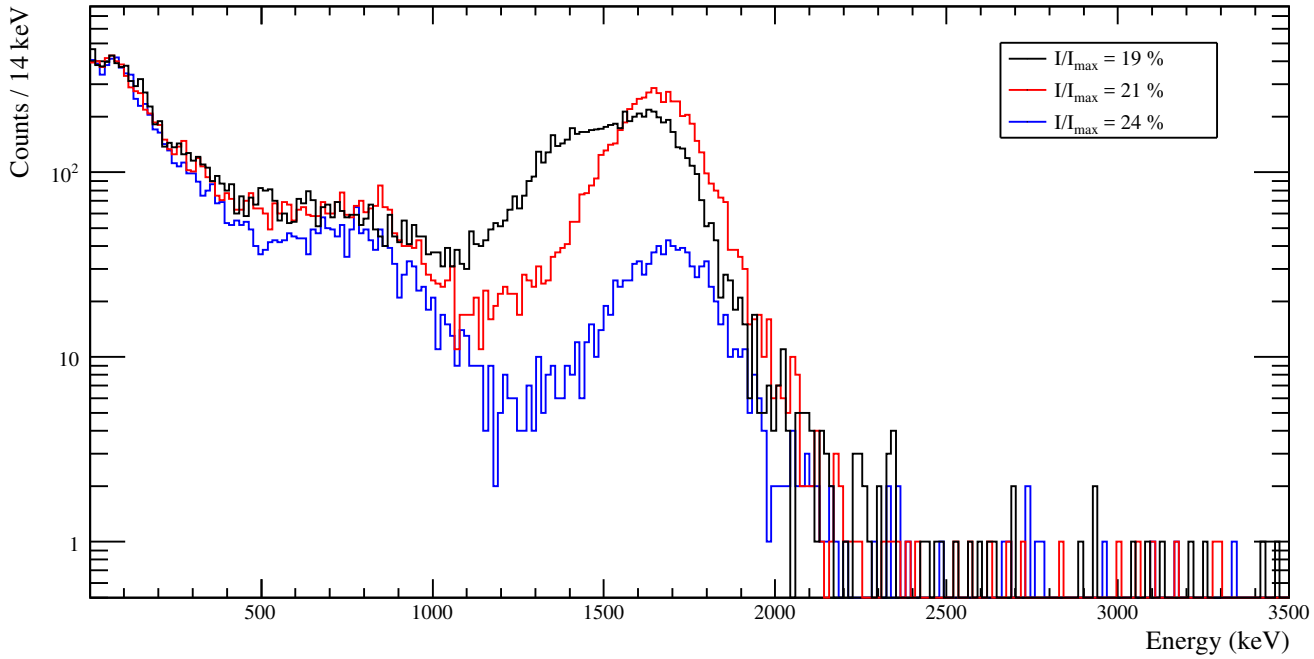

Figure 25. Electron spectrum of ^{207}Bi source around 1.682 MeV area measured with the Scionix v.2.0 detector. The duration of the measurements were 5 minutes. The VETO or $\Delta E - E$ cut has not been enabled.

4.1.2 Background radiation tests

Measuring the transition from ^{20}F ground-state to the ground-state of ^{20}Ne is an extremely low count rate measurement. Therefore, it is important to determine the number of background counts that need to be substracted from the measured electron spectrum. Background radiation is radiation from natural and artificial sources around us. The most common sources for background radiation are for example the cosmic rays, ^{40}K from the concrete and the decay chain products of naturally occuring uranium and thorium. The background measurements were done with and without a lead shielding to find out if the background could be sufficiently reduced by shielding. The results of lead shielded background measurements are described in chapter 4.1.2.1. Measurements inside and outside of the spectrometer were also carried out to find out if the background is different inside the spectrometer. To investigate whether the magnetic field induces more background to the detector, the measurements were done also with and without the magnetic field.

4.1.2.1 Lead shielding test

The level of background radiation was measured inside a lead shielding to have an estimate of how much the leadshielding reduces the background radiation level at the signal area of 5.5 MeV to 7.4 MeV. The Scionix (v. 1.0) detector was placed inside of a cave made of 5 cm thick leadbricks, that is shown in Appendix I fig. 7 and 8. The detector's entrance window was covered with a light tight cover. The detector was placed inside a piece of beamtube with a closed end cup to shield the detector from possible damage. The lead cave was covered with a black plastic bag to make sure that the detector was fully covered from the light. The background radiation was measured inside the lead shielding for 48 hours. The result of this measurement is shown on Fig. 26 with a red line. The background radiation without the shielding was measured before and is shown with blue on Fig. 26. This is also scaled to the 48 hours. The ratio is shown in the lower figure with black, the red being the error band calculated as

$$\delta R = R \cdot \sqrt{\left(\frac{\sqrt{N_1}}{N_1}\right)^2 + \left(\frac{\sqrt{N_2}}{N_2}\right)^2}, \tag{6}$$

where N_1 and N_2 are the counts of the measurements labeled background and background + Pb respectively.

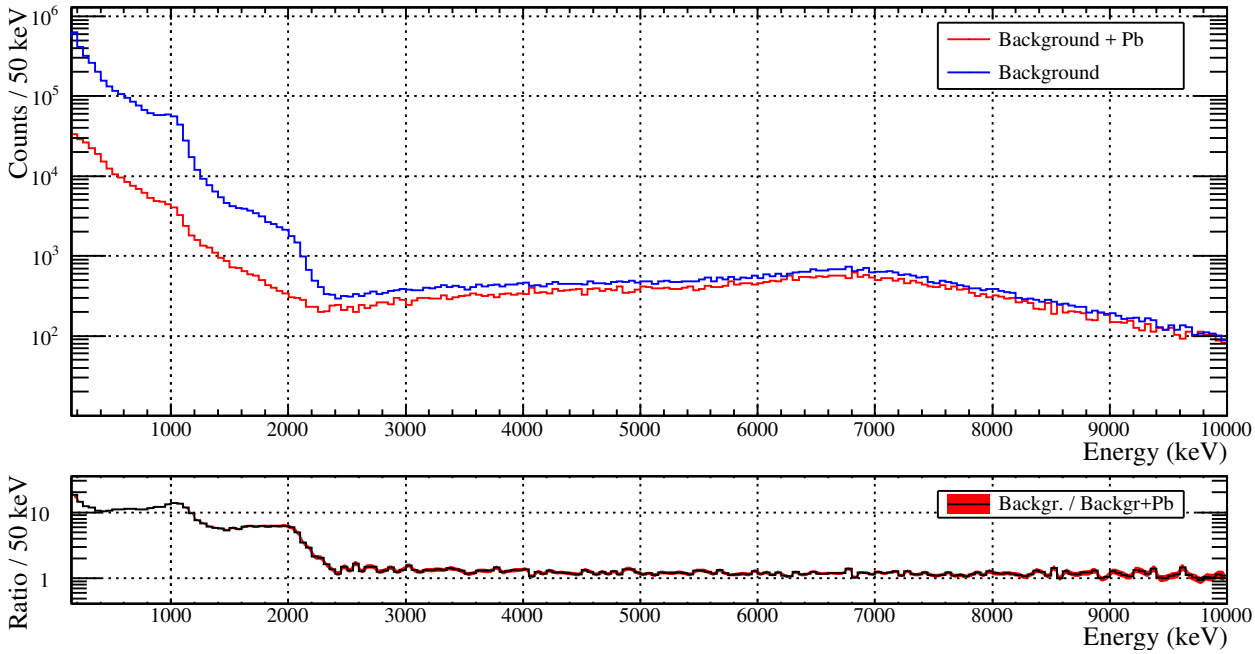

Figure 26. The measured background radiation spectra with and without lead cave and the ratio with an error band. The measurements were done with the Scionix v.1.0 detector.

The amount of counts between the energies of 5.5 MeV and 7.5 MeV on the background without a shield was (486.04 ± 22.05) when with a lead shielding it was (405.101 ± 20.127). This gives us a ratio of (1.20 ± 0.08) between the energies of $5.5 - 7.5$ MeV which is shown in the lower part of Fig. 26. This indicates that the lead shield would not make much of a difference in reducing the background radiation at the higher energies. At lower energies the lead shielding reduced the background radiation by a factor 10. With this reduction factors it was not feasable to modify the experimental setup to fit the lead shielding.

4.1.2.2 Background reduction by VETO detector

In Fig. 27 a background measurement has been implemented with a measurement done with a ^{207}Bi source. The measurement has been done with the Scionix v. 1.0 detector. From this measurement it can be seen that at the high energies the measured background radiation follows the measurement with ^{207}Bi. This confirms that it is indeed background radiation at the higher energies. In Fig. 27a) the background measurement implemented with a ^{207}Bi source measurement is shown without the veto cut condition enabled. The count rate between 5 MeV and 6 MeV is around 149 counts / hour. In fig. 27b) the veto cut condition has been enabled. The countrate between 5 MeV to 6 MeV was reduced to only 3.37 counts/hour. The reduction of the background rate is a factor of 44.2.

In Fig. 28 the measured background radiation with both Scionix detectors is shown. Figure 28a) has a background measurement measured with Scionix v.1.0 detector. The count rate without veto cut condition between energies 5 MeV to 7 MeV is around 264.2 counts/hour. When the veto cut condition is enabled the count rate is 3.4 counts/hour. Figure 28b) has the background radiation measured with the Scionix v.2.0. The count rate without the veto cut condition and the Δ E - E cut enabled is 277.2 counts/hour. When the veto cut condition is enabled the count rate is 4.9 counts/hour. The VETO is little less efficient in the Scionix v.2.0 detector because the gain of the VETO detector has been reduced. When the Scionix v. 2.0 is applied with the Δ E - E cut the measurement results to a count rate of 2.4 counts/hour. Meaning that the reduction factor is 113 when with the v.1.0 detector at the same energy range the reduction factor was 107.

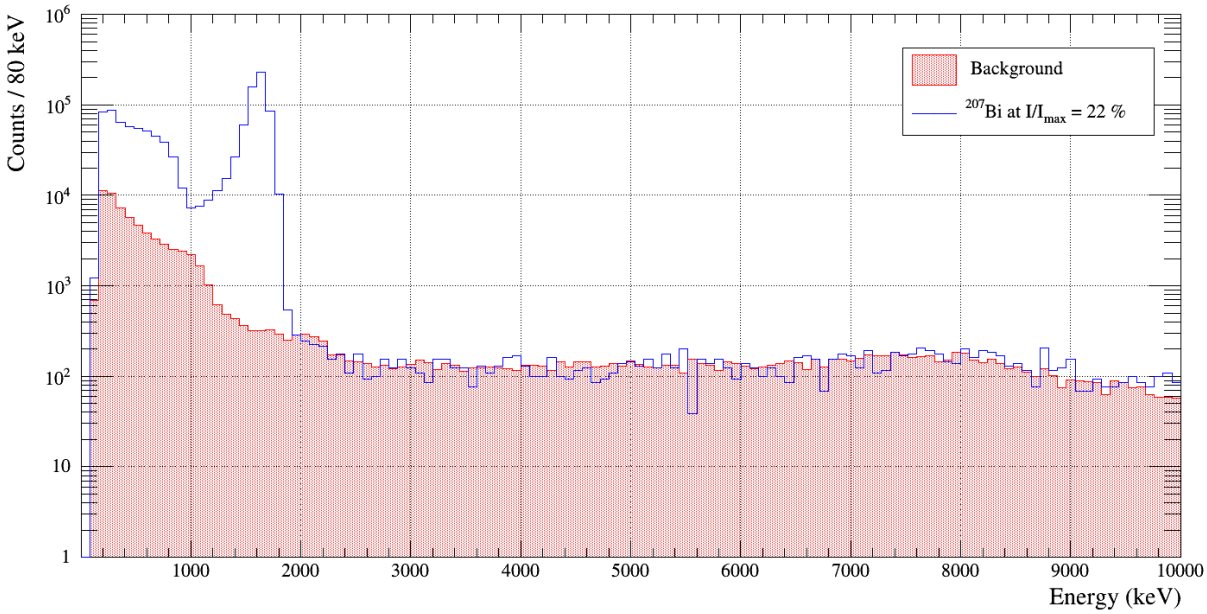

(a) Background and ^{207}Bi signal detected but the VETO condition is not enabled. The amount of counts between 5 MeV and 6 MeV was 149 counts/hour.

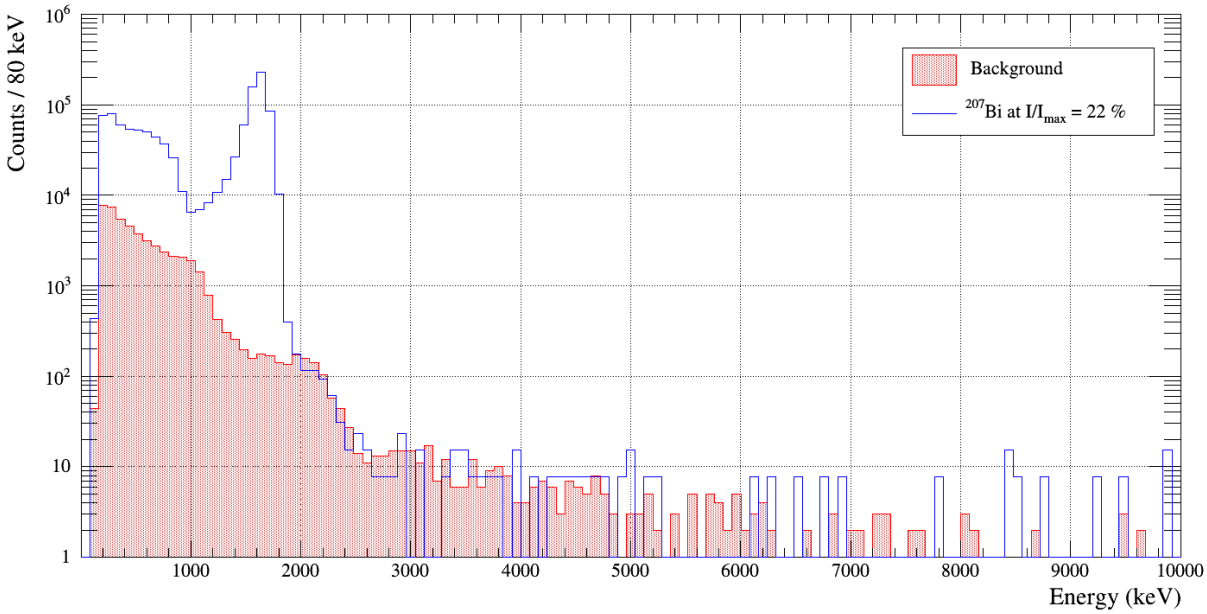

(b) Background and ^{207}Bi signal detected with the VETO condition enabled. The amount of counts between 5 MeV and 6 MeV was 3.37 counts/hour.

Figure 27. Measurements of the background radiation with a signal implemented from the ^{207}Bi source detected on a magnetic field current setting of $I/I_{max} = 22$ %. Measurements were made with the Scionix v.1.0 detector. The background measurement is scaled to be the same duration as the ^{207}Bi measurement.

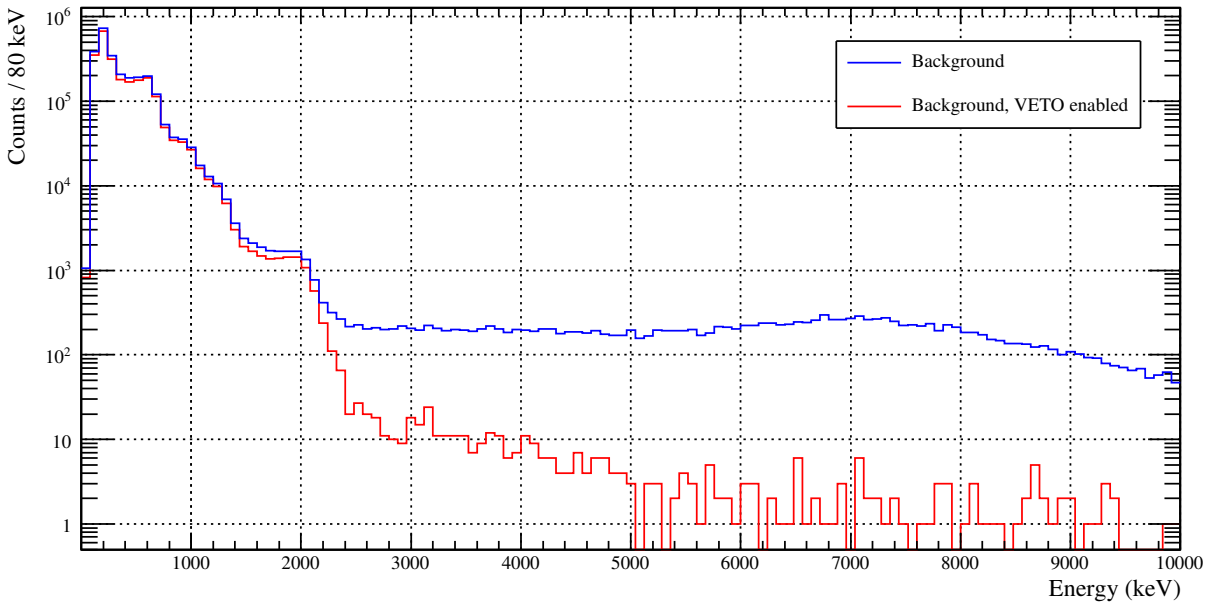

(a) The background radiation measured with Scionix v. 1.0 detector for 15.6 hours.

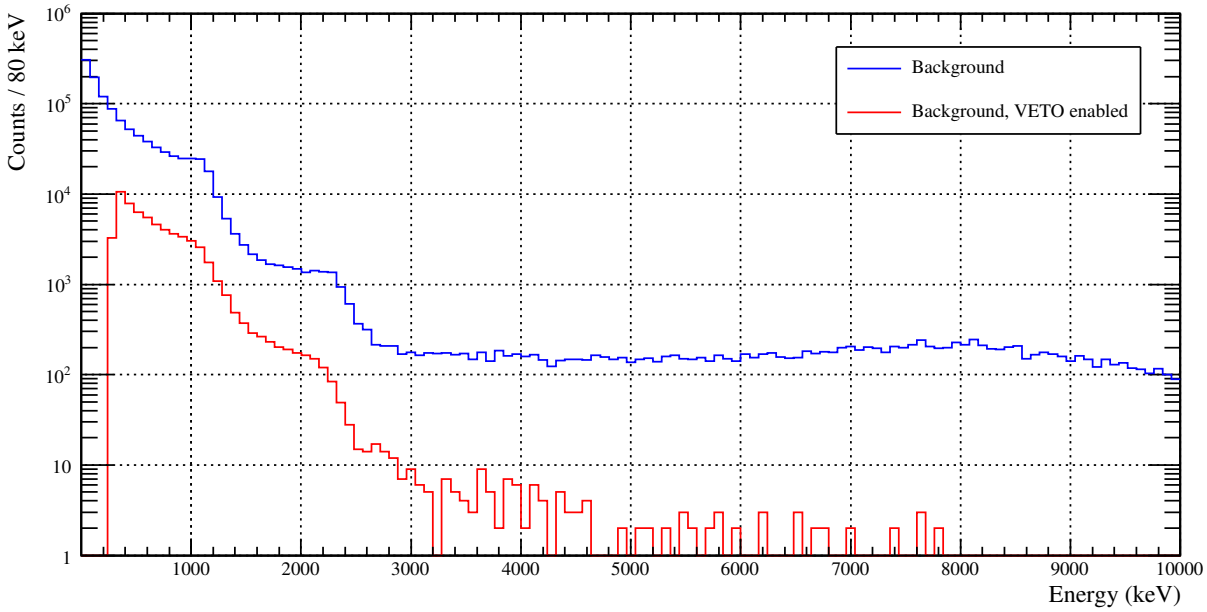

(b) The background radiation measured with Scionix v. 2.0 detector for 15.1 hours.

Figure 28. Measurements of the background radiation with the Scionix v.1.0 detector and the Scionix v. 2.0 detector. The signal is shown in blue and the signal with enabled VETO cut condition is shown in red. In Scionix v.2.0 detector the $\Delta E - E$ cut has also been enabled.

4.1.2.3 Background radiation tests underground

To estimate whether the background radiation seen in the high-energy region of the Scionix v. 1.0 detector was from cosmic rays or something else, the background radiation was measured also in the underground laboratory of Pyhäsalmi mine. The laboratory is located in about 1.4 km underground (4000 meters of water equivalents) where the cosmic muon flux is around $5.9 \cdot 10^{-7}$ $1/\mathrm{m}^2\mathrm{s}$ compared to 1 muon $1/\mathrm{m}^2\mathrm{s}$ on the ground level [39]. The measurement area in the CallioLab at Pyhäsalmi is shown in Fig. 29.

The Scionix detector was placed inside a vacuum tube in atmospheric pressure to keep the detector safe and light tight. The duration of the measurement was around 20 hours. The spectra collected are shown in Fig. 30. No counts are seen in the signal area from 5.5 MeV to 7.4 MeV. If there is an event in the VETO detector in coincidence with the signal detector, it will be rejected. This provides us the knowledge of the background radiation detected in the signal area is from the cosmic rays in the JYFL laboratory.

Figure 29. The measurement area in the CallioLab of Pyhäsalmi mine.

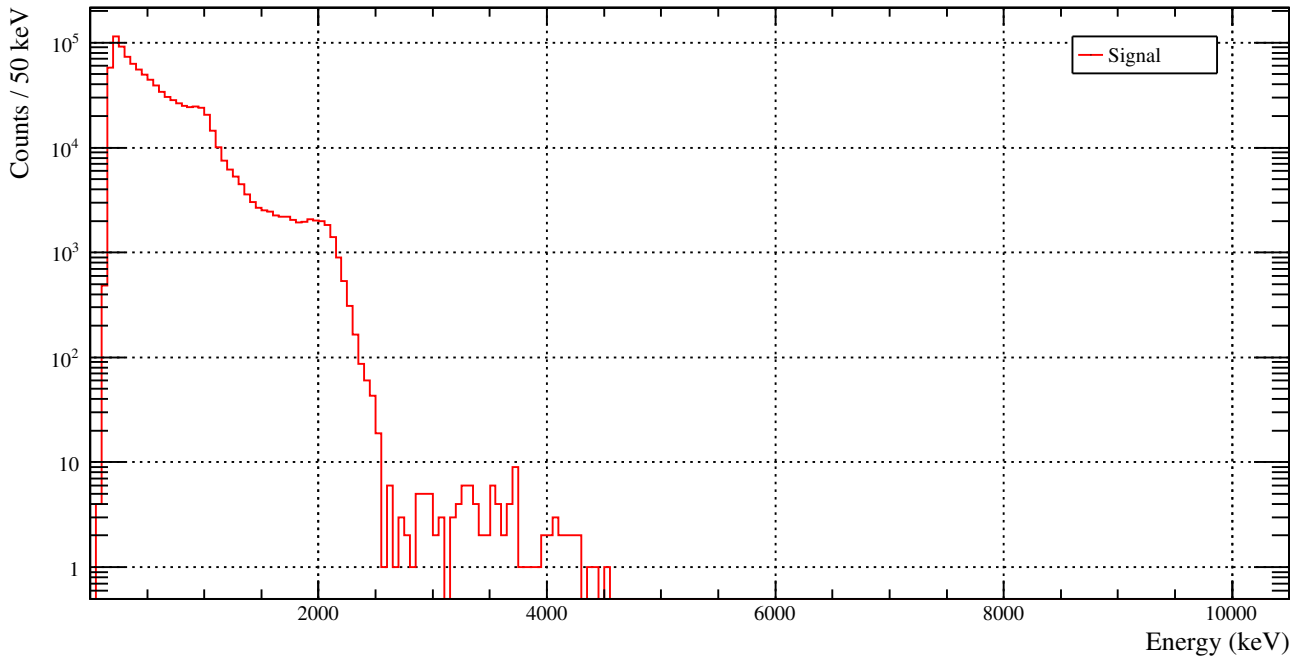

Figure 30. The counts measured underground as a function of the energy of the particles. The red line indicates the signal channel. In the signal area of the second forbidden transition around 5.4 MeV to 7.4 MeV no counts were detected.

4.1.2.4 Muon test with Scionix v. 1.0 and v. 2.0

The resolution of the Scionix v. 2.0 was determined by making a telescope setup. The Scionix v. 2.0 was placed at one end of a vacuum tube when Scionix v. 1.0 in the other end. The tube was placed vertically so that the Scionix v. 1.0 was on top of the v. 2.0 detector creating a telescope like system as shown in Fig. 31. The measured muon count could be determined when a coincidence condition was applied: a hit had to be seen in both Scionix v.1.0 and Scionix v.2.0 signal detectors close to the same energy and time. The distribution of the high energy muons is shown in Fig. 32 where it can be seen that the resolution of the detectors is comparable. The resolution for the Scionix v.1.0 detector was around (4.6 ± 1.7) % and for the Scionix v.2.0 (8.0 ± 2.8) % when 81 high energy muons were detected going through both signal detectors in 4 hours. The resolution was achieved by fitting a Gaussian function with a constant background on the high energy muons and dividing the standard deviation (σ) with the mean value of the distribution.

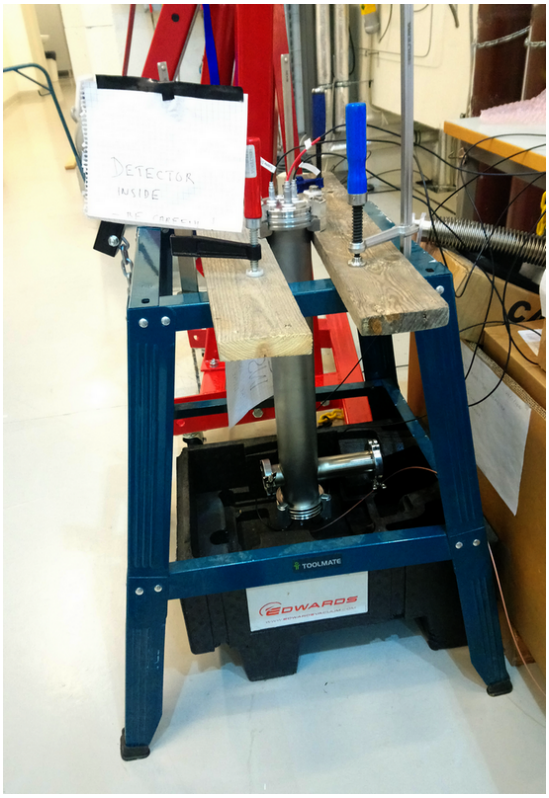

Figure 31. The built muon telescope setup where the Scionix v.2.0 is on top side and Scionix v.1.0 at the bottom side of the vacuum tube.

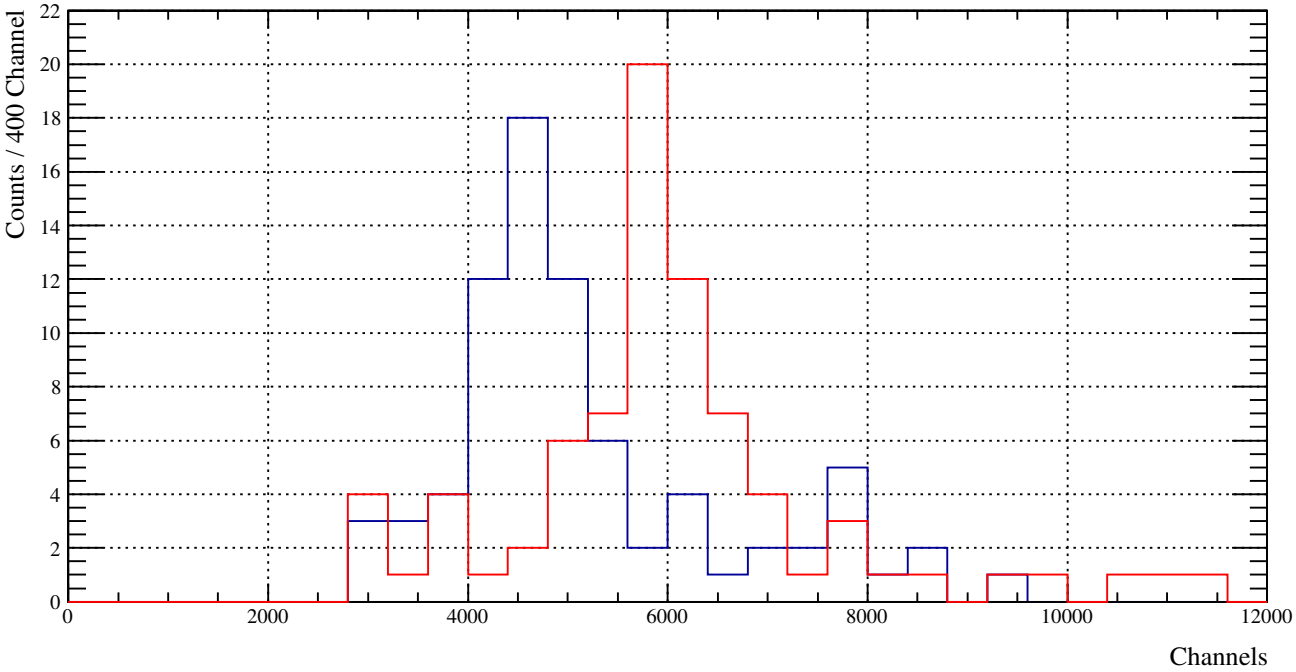

Figure 32. Detected muons at the high energy area, where the blue line is for the signal detector of Scionix v.2.0 and the red line is for the signal detector of Scionix v.1.0.

4.2 $LaBr_3$(Ce) detector and its efficiency

The efficiency of the $LaBr_3$(Ce) detector was measured in May 2017 and after the experiment in 2018. Here the measured efficiencies after the experiment in 2018 are discussed. The measurements were made with four different sources: ^{152}Eu (JYFL-81, 15.2.2018), ^{60}Co (JYFL-80, 14.2.2018), ^{207}Bi (JYFL-91, 20.2.2018) and a mixed source (JYFL-030, 22.2.2018) consisting of ^{241}Am, ^{137}Cs and ^{60}Co.

The activity of the source on the day of the measurement can be calculated

$$A = A_0 e^{-\frac{ln(2)}{T_{1/2}}t}, \tag{7}$$

where A_0 is the activity of the source on the reference day, $T_{1/2}$ is the half-life of the nuclide and t is the time between the reference day and the measurement day.

The error of the activity can be calculated

$$dA = \sqrt{\left(e^{-\frac{ln(2)}{t_{1/2}}t} \cdot \delta A_0\right)^2 + \left(\frac{ln(2)}{t_{1/2}^2} t A_0 e^{-\frac{ln(2)}{t_{1/2}}t} \cdot \delta t_{1/2}\right)^2 + \left(-\frac{ln(2)}{t_{1/2}} A_0 e^{-\frac{ln(2)}{t_{1/2}}t} \cdot \delta t\right)^2}, \tag{8}$$

where the error of time δt has been taken to be 4 hours (half of a workday). The rest of the used values can be found in table 3.

The observed activity is defined as follows:

$$A_{obs.} = \frac{N_\gamma}{t_{measured} \cdot I_\gamma}, \tag{9}$$

where N_γ is the counts measured at a certain energy γ-ray peak, $t_{measured}$ is the duration of the measurement and I_γ is the intensity of the γ-ray. The intensities were taken for each γ-ray transition from National Nuclear Data Center by Brookhaven National Laboratory webapage [40] and are tabulated in table 4 with more detailed references. All of the measurements were scaled to 653 minutes, which was the duration of the shortest measurement.

The error of the observed activity is calculated as

$$\mathrm{d}A_{obs.} = \left[\left(\frac{1}{t_{meas.} \cdot I_\gamma} \cdot \delta N_\gamma\right)^2 + \left(-\frac{N_\gamma}{t_{meas.}^2 \cdot I_\gamma} \cdot \delta t_{meas.}\right)^2 + \left(-\frac{N_\gamma}{t_{meas.} \cdot I_\gamma^2} \cdot \delta I_\gamma\right)^2\right]^{1/2}, \tag{10}$$

where $\delta t_{meas.}$ was determined to be 60 s and the error of counts was determined from the fitting of the peaks.

Using above calculations the efficiency can be calculated as

$$\varepsilon = \frac{A_{observed}}{A}. \tag{11}$$

The uncertainty for efficiency can be calculated as

$$\mathrm{d}\epsilon = \sqrt{\left(\frac{1}{A} \cdot \delta A_{obs.}\right)^2 + \left(-\frac{A_{obs}}{A^2} \cdot \delta A\right)^2}. \tag{12}$$

The calculated efficiencies are tabulated in table 4 with the corresponding energies and plotted in Fig. 33.

As an example the efficiency calculation at 344 keV is shown. The activity on the measurement day is calculated with equation 7. This gives $A = (18.7 \pm 0.6)$ kBq, where the error has been calculated using equation 8. The observed activity was calculated with equation 9 giving $A_{obs.} = (5.55 \pm 0.07)$ Bq, when the number of counts was (57846 ± 477). The number of counts is given by a Gaussian fit with an constant background. The error of the observed activity was calculated using equation 10. From these two activities the efficiency and its error can be calculated with equations 11 and 12 giving an efficiency of $\varepsilon = (2.97 \pm 0.10) \cdot 10^{-4}$. The measured γ-ray spectrum of ^{152}Eu in logarithmic scale is shown in fig. 34 where the most prominent γ-ray peaks are marked.

Table 3. Sources used for the efficiency calibration measurements of $LaBr_3(Ce)$ detector and activities of the sources with their reference dates and half-lives.

Source	Activity (kBq)	Reference date	Half-life
^{152}Eu (JYFL-81)	(40.1 ± 1.2)	1.4.2003	(13.517 ± 0.009) y
^{60}Co (JYFL-80)	(401 ± 12)	1.4.2003	(1925.28 ± 0.14) d
^{207}Bi (JYFL-91)	(397 ± 12)	15.12.2008	(31.55 ± 0.04) y
Mixed source (JYFL-30)		1.4.1995	
^{241}Am	(6.2 ± 0.4)		(432.6 ± 06) y
^{137}Cs	(2.3 ± 0.1)		(30.08 ± 0.09) y
^{60}Co	(3.8 ± 0.2)		(1925.28 ± 0.14) d

Table 4. Literature energies (Ref. [41, 42, 43, 44]) of the detected γ-rays and the intensities of the γ-ray branches with the calculated efficiencies.

Energy (keV)	Source	Intensity I_γ (%)	Efficiency
(344.2785 ± 0.0012)	^{152}Eu	(26.59 ± 0.20)	$(2.97 \pm 0.10) \cdot 10^{-4}$
(569.698 ± 0.002)	^{207}Bi	(97.75 ± 0.03)	$(1.61 \pm 0.05) \cdot 10^{-4}$
(661.657 ± 0.003)	^{241}Am, ^{137}Cs, ^{60}Co	(85.10 ± 0.20)	$(1.49 \pm 0.07) \cdot 10^{-4}$
(778.9045 ± 0.0024)	^{152}Eu	(12.93 ± 0.08)	$(0.99 \pm 0.05) \cdot 10^{-4}$
(964.057 ± 0.005)	^{152}Eu	(14.51 ± 0.07)	$(0.82 \pm 0.05) \cdot 10^{-4}$
(1063.656 ± 0.003)	^{207}Bi	(74.5 ± 0.3)	$(0.79 \pm 0.03) \cdot 10^{-4}$
(1173.228 ± 0.003)	^{60}Co	(99.85 ± 0.03)	$(0.66 \pm 0.02) \cdot 10^{-4}$
(1332.492 ± 0.004)	^{60}Co	(99.9826 ± 0.0006)	$(0.64 \pm 0.02) \cdot 10^{-4}$
(1770.228 ± 0.009)	^{207}Bi	(6.87 ± 0.03)	$(0.424 \pm 0.013) \cdot 10^{-4}$

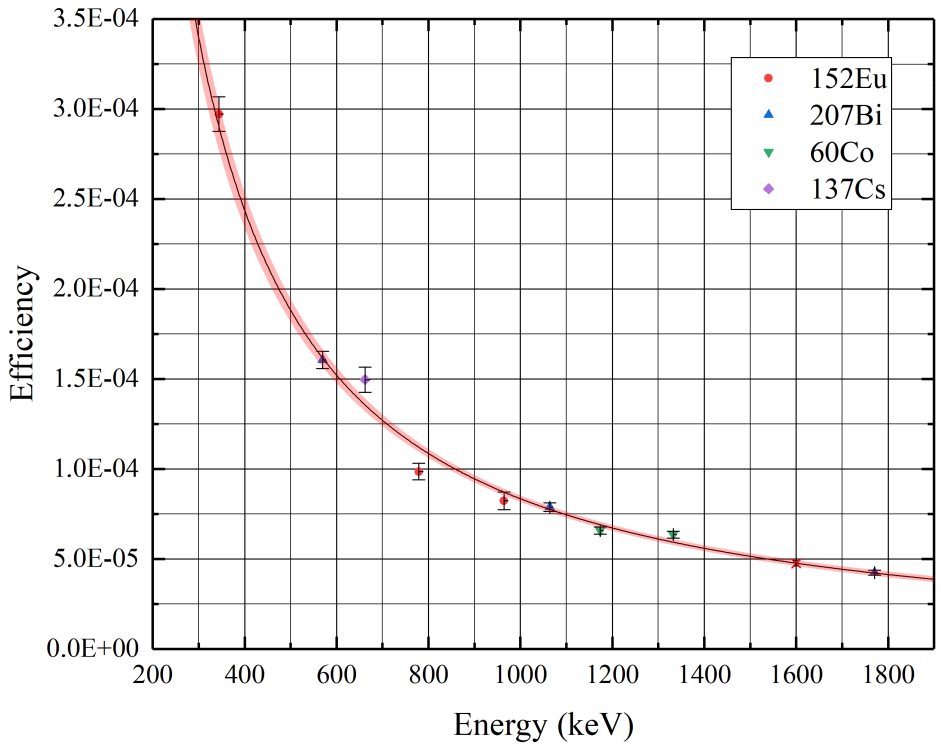

Figure 33. The calculated efficiencies as a function of energy. Efficiencies calculated using different sources are marked with different colors. The confidence band used on the fit was 68 %. The efficiency of interest at 1.6 MeV is marked with a red cross.

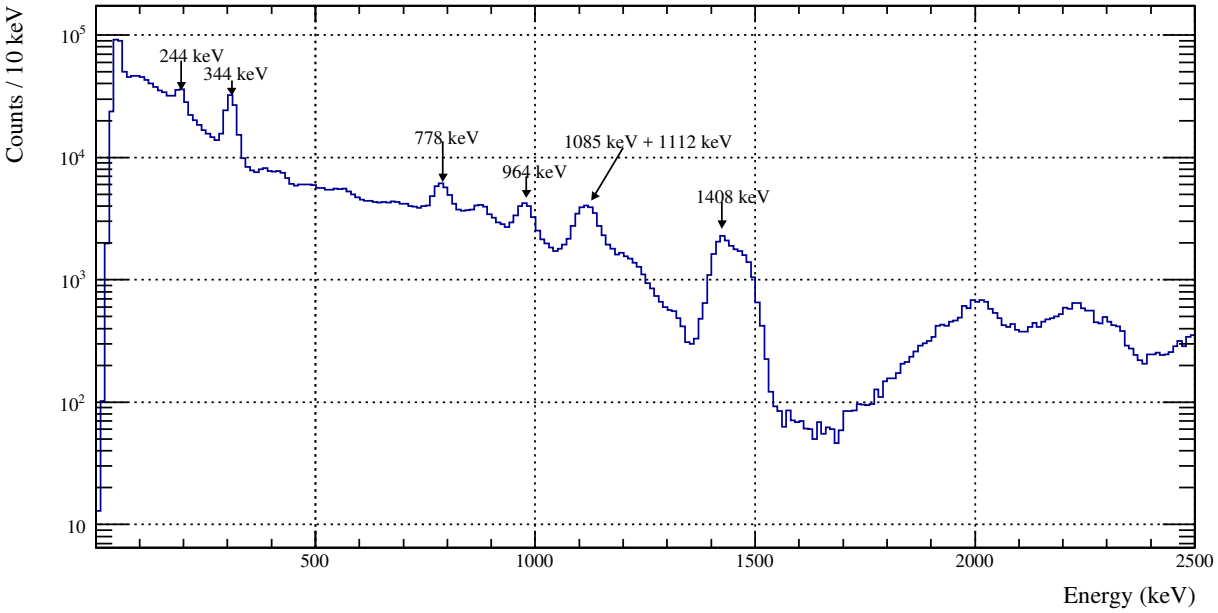

Figure 34. γ-ray spectrum of ^{152}Eu source measured with $LaBr_3(Ce)$ detector. The bump next to 1408 keV peak is from the ^{40}K background radiation. The peaks around 2 MeV and 2.25 MeV are from the internal properties of the $LaBr_3(Ce)$ crystal.

The efficiency of the $LaBr_3(Ce)$ detector at 1.6 MeV can be determined from fig. 33 to be $\varepsilon = (4.77 \pm 0.18) \cdot 10^{-5}$. The error of the efficiency has been determined by using a confidence band of 68 %. Efficiency at 1.6 MeV is of interest because of the γ-rays coming from the de-excitation of the first excited state in ^{20}Ne (see Fig. 5). This can be used as an absolute normalization of the ^{20}F yield.

4.3 Magnetic field measurements of the spectrometer

Precise GEANT4 simulations have been conducted for the whole measurement setup and have been used in the analysis of the experimental data. The simulations are based on a certain type of distribution of the magnetic field. The main goal during these measurements was to confirm that the magnetic field distribution corresponds to the distribution used in the simulations.

Measurements to characterize the magnetic field of the spectrometer were made. The magnetic field was measured using a Danfysik Group3 LPT-130 Hall probe fixed into a plastic tube that was supported from one side of the spectrometer. This provided us to have the probe perpendicular to the magnetic field and also keep the probe on the axial line of the spectrometer.

To define the shape of the magnetic field throughout the whole spectrometer the shield with the $LaBr_3$ detector was removed. The measurement was started from the detector side because the entrance side of the spectrometer was too tight to fit the measurement stick between the beamline and the spectrometer. In fig. 35 the results obtained are shown with a comparison to a simulation. The simulation uses a 18K-configuration of

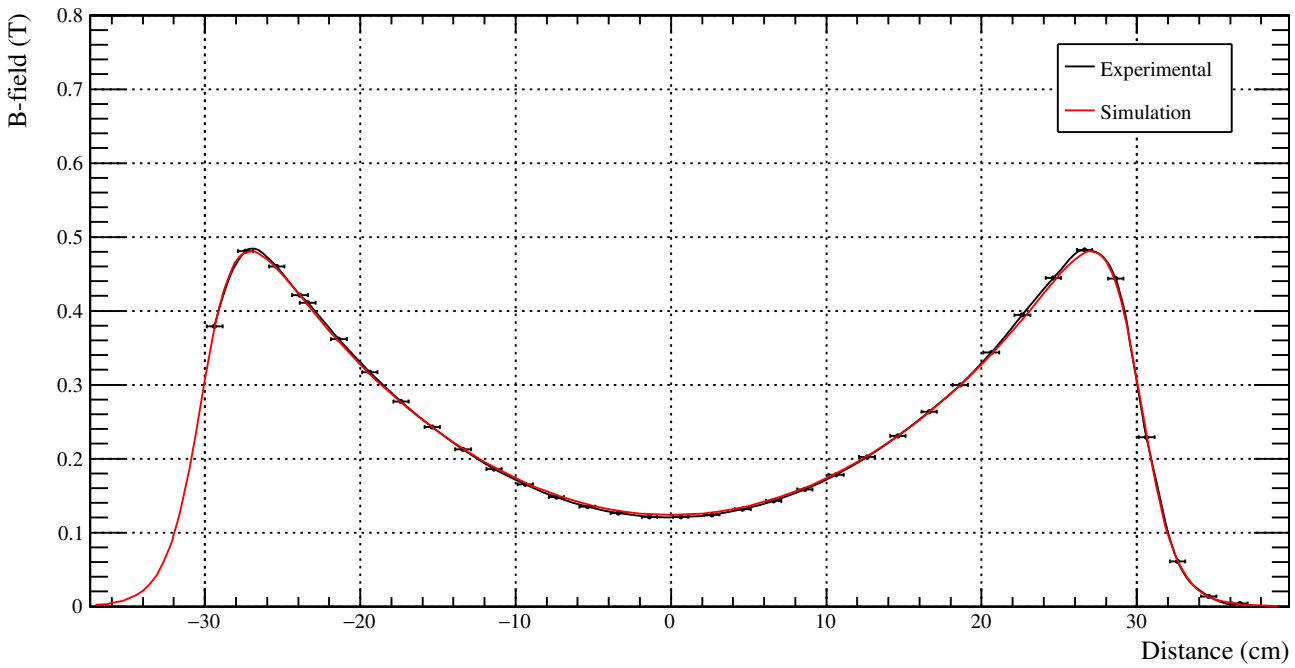

Figure 35. Magnetic field strength of the spectormeter as a function of distance. The measured magnetic field strength is shown in black and the GEANT4 simulation in red.

the magnet assuming 12800 Ampere-windings in the outermost coils. The measured magnetic field agrees with the simulated field well. The simulated field had to be scaled with a factor of $8 \cdot 10^{-5}$ to make the measured field fit the simulated field, but the shape of the field agrees confiming the 18K-configuration of the spectrometer.

The linearity of the current scaling was tested from both sides of the spectrometer while having the brass shield inside. The result of the measurements from both ends of the spectrometer are shown in fig. 36. The scaling of the magnetic field as a function of the current applied to the coils could be found to be rather linear in different distances inside the spectrometer. Also it can be noted that both coils gave similar readings for the magnetic fields at similar distances and current values. Rotating the probe to 90 degrees had no effect on the magnetic field reading, so small differences on the probes angular position did not affect the measurements.

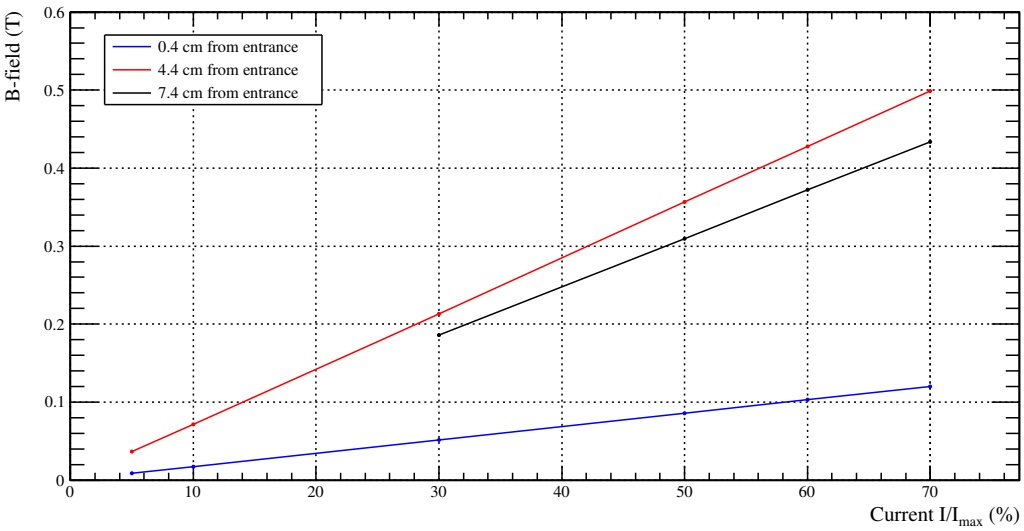

(a) From the entrance side of the spectrometer.

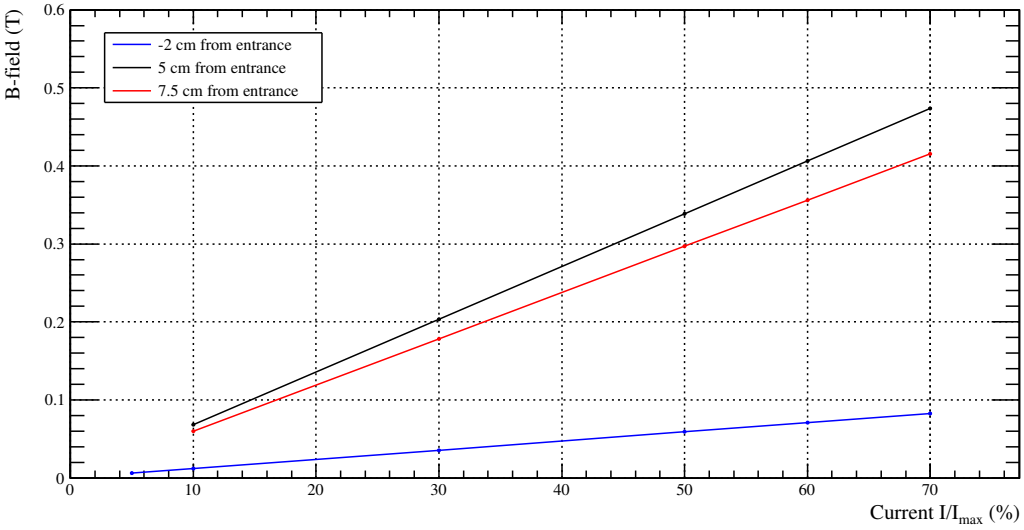

(b) From the detector side of the spectrometer.

Figure 36. The linearity of the magnetic field strength shown as a function of the current setting of the spectrometer. The current is given in I/I_{max} and the dependence of the magnetic field strength and I/I_{max} is described in chapter 3.2.

5 β-decay studies of ^{20}F at IGISOL

5.1 Production of ^{20}F at IGISOL

In May 2017 a yield test of $^{20}F^{+}$ beam was conducted at the IGISOL facility. The ^{20}F activity was produced by 9 MeV deuterons from the K130 cyclotron impinging on a 1.2 mg/cm^2 thick BaF_2 target at the entrance of the light ion guide. Based on the estimated range of produced fluorine ions in BaF_2 target, the effective target thickness was estimated to be 0.2 mg/cm^2. Here effective target thickness describes an area of the target where the reaction products have enough energy to survive out of the target and are also still stopped in the gas. The reaction products at IGISOL are usually stopped in purified helium gas and the products are extracted out of the gas cell using the sextupole ion guide (SPIG). Then the products were accelerated to 30 keV and mass-separated with a 55° dipole magnet based on the products mass to charge ratio (m/q). At switchyard the mass-separated $^{20}F^{+}$ beam was sent to the end of the spectroscopy line, where a spectroscopy setup was built. It consisted of a 500 μm thick and round Si-detector with an area of 300 mm^2 and an efficiency of around 31 % equipped with an Al-foil ladder. The silicon detector was followed by a $3\pi\Delta E_\beta$ β scintillator detector and a Canberra GC7020 coaxial Ge-detector. This setup is shown in Fig. 37. Measurements of the yield were also made at the switchyard (SW) Si-detector. The results related to the scintillator and Ge detector measurements have already been reported in A.Khanam's MSc thesis [45]. In this work, the yield of ^{20}F was optimized by studying the optimal beam energy, SPIG coil configuration and helium pressure for which the yields using the Si detectors at SW and spectroscopy line were used.

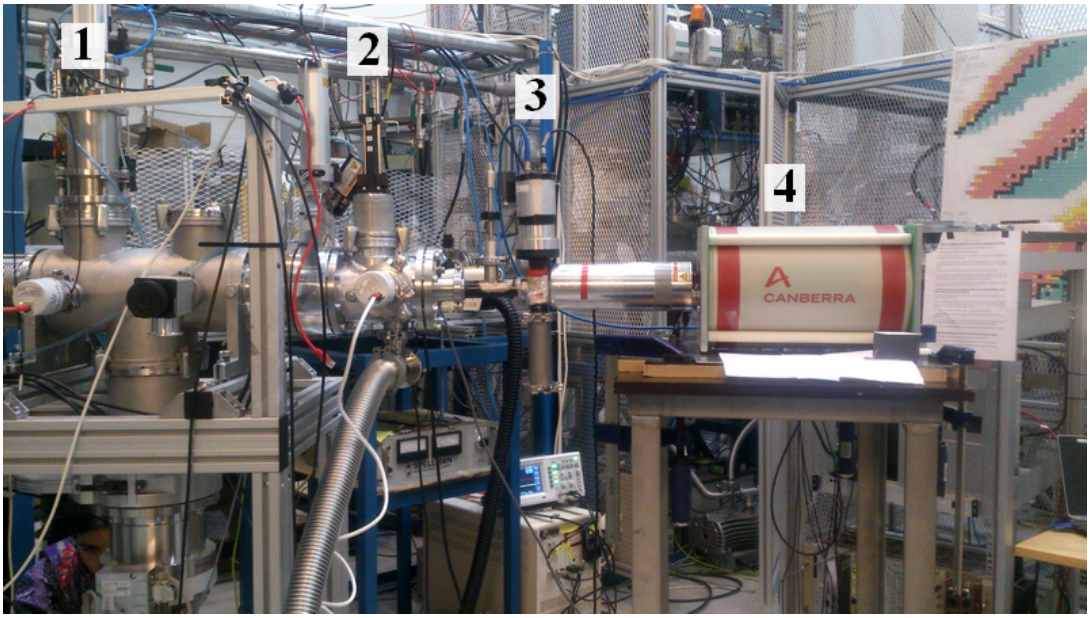

Figure 37. The spectroscopy setup at the end of the spectroscopy line consisting of a Si-detector (2), IGISOL scintillator detector (3) and a Ge-detector (4). The beam is implanted on a tape just before the Ge-detector. The spectroscopy beamline was equipped with a Faraday cup (1).

5.1.1 Optimal deuteron beam energy and intensity

A TALYS [46] calculation for the used reaction ^{19}F(d,p)^{20}F was conducted and is shown in Fig. 38. This shows that the largest cross section for ^{20}F would be around 140 mb produced with a deuteron beam with an energy between 4 - 6 MeV. The ^{20}F experiment was initially planned to be run using the MCC-30 cyclotron which can produce deuterons with an energy range of 9-15 MeV. Hence, the yield test was done using 9 MeV deuterons from the K130 cyclotron. To obtain the best yield of ^{20}F beam, additional degrader foils to reduce the beam energy were tested in front of the BaF_2 target. The test was run with three different configurations: without a degrader foil, with 52 μm thick Ta degrader foil and 100μm thick Ta degrader foil. The degrader foil was placed at the entrance window of the ion guide. The effect of the degrader foil thickness can be seen in Fig 39 where the measured β countrate with the switchyard Si-detector is shown as a function of the primary deuteron beam intensity measured at the Faraday cup labeled FCE2 located just before the IGISOL target chamber. The different Ta degrader foil configurations are marked with different colors: black is without a degrader foil, blue is with the 52 μm foil and red is with a 100μm foil. These measurements were all done with the same SPIG RF coil frequency of 3.1 MHz. The highest yield of $^{20}F^{+}$ ions was obtained with a 52 μm Ta degrader foil. The efficiency of the Si-detector is around 30 % giving us a yield of 32000

^{20}F ions/s. When comparing this to a measurement made without the Ta degrader foil the $^{20}F^{+}$ ion rate dropped by 34 %. During the measurements the energy deposition on the degrader foil made the temperature rise at the ion guide. One deuterium deposits 5.1 MeV of its energy on a 100 μm thick Ta foil. With a beam current of 10 μA this would mean the energy transfer of around 50 W. From the same figure it can be seen that the yield increases steadly as the primary beam intensity was increased and no saturation of the yield can yet to be seen with any of the three different configurations. In general with high beam intensities the yield does not rise linearly but rather saturates when for example plasma begins to form lowering the efficiency of the ion guide.

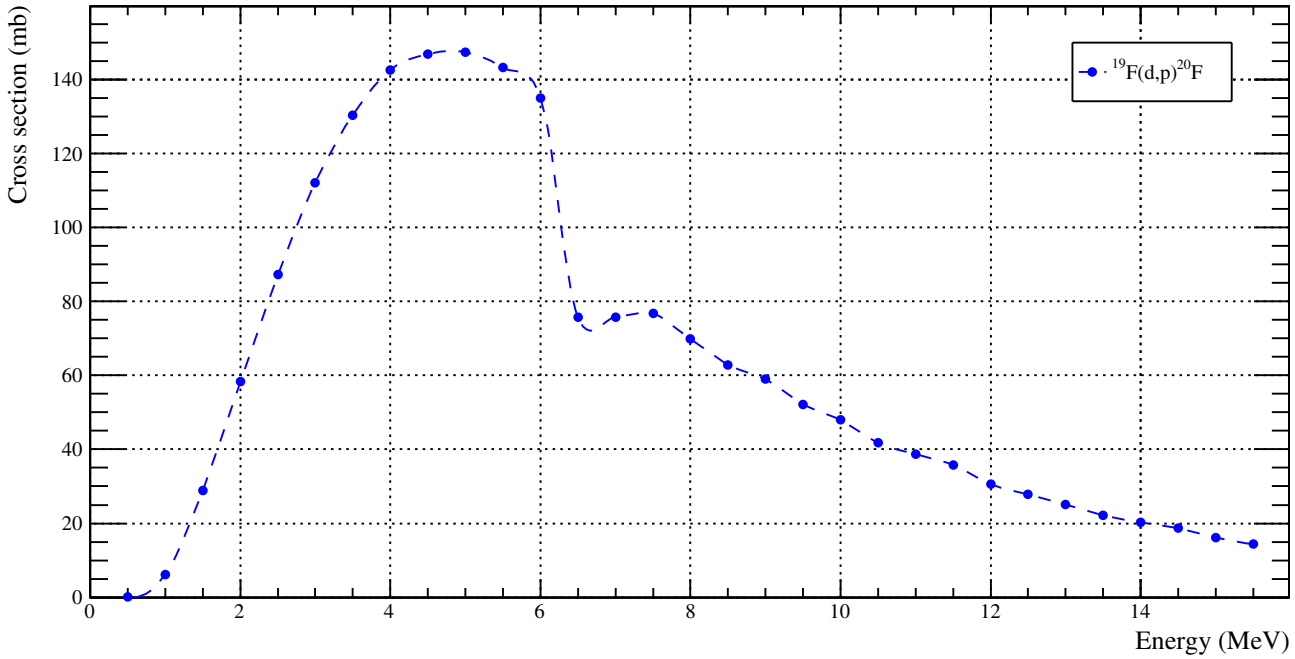

Figure 38. TALYS calculation of the cross section for the production of ^{20}F via ^{19}F(d,p) reaction. The line is to guide the eye while the points are the actual results of the TALYS calculation.

5.1.2 SPIG RF coil frequencies

At IGISOL, there are currently three different SPIG RF coils available: 2.8 MHZ, 3.1 MHz and 5.6 MHz. The higher frequency coils should in theory work better for lighter ions. Here, we wanted to study the effect of different coils on the ^{20}F yields. Figure 39 shows a comparison between the different SPIG coil frequencies. The yields obtained with the 3.1 MHz SPIG coil are clearly higher than yields obtaind with the 2.8 MHz and 5.6 MHz coils at all studied primary beam intensities.

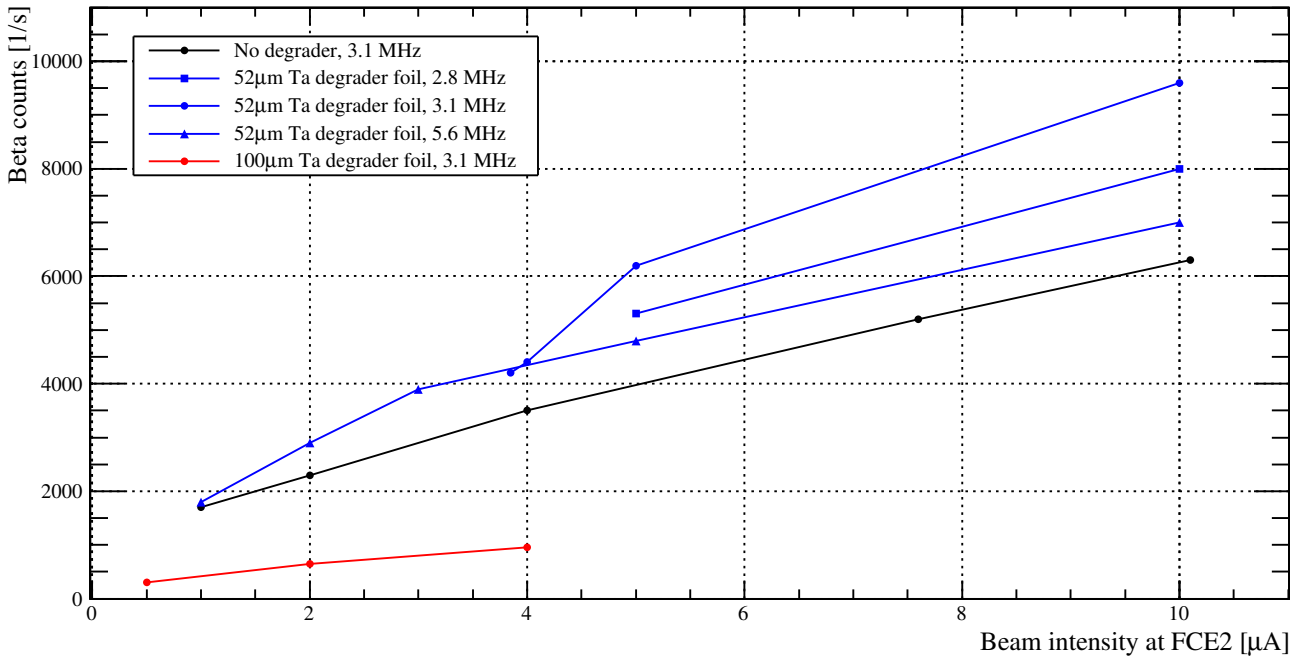

Figure 39. The β counts detected at switchyard (SW) Si-detector as a function of the primary beam intensity measured at FCE2. The data is classifyed depending on the Ta degrader foil thickness and the frequency of the SPIG coil used.

5.1.3 Helium pressure

Helium pressure is used in the ion guide to thermalize the reaction products. The pressure needs to be optimized for each studied case because the produced ions have different masses and energies depending on the reaction and beam energy. A measurement of the yield compared to the helium pressure of the ion guide was made. The helium pressure of the ion guide was varied from 70 mbar to 295 mbar. The result of this measurement is shown in Fig. 40. The yield of $^{20}F^{+}$ ions grows linearly as a function of the helium pressure until about $150 - 200$ mbar. This means that with higher pressure more of the $^{20}F^{+}$ ions are stopped in the helium gas. The maximum rate of β counts detected was when the helium gas pressure was between 200 mbar to 250 mbar.

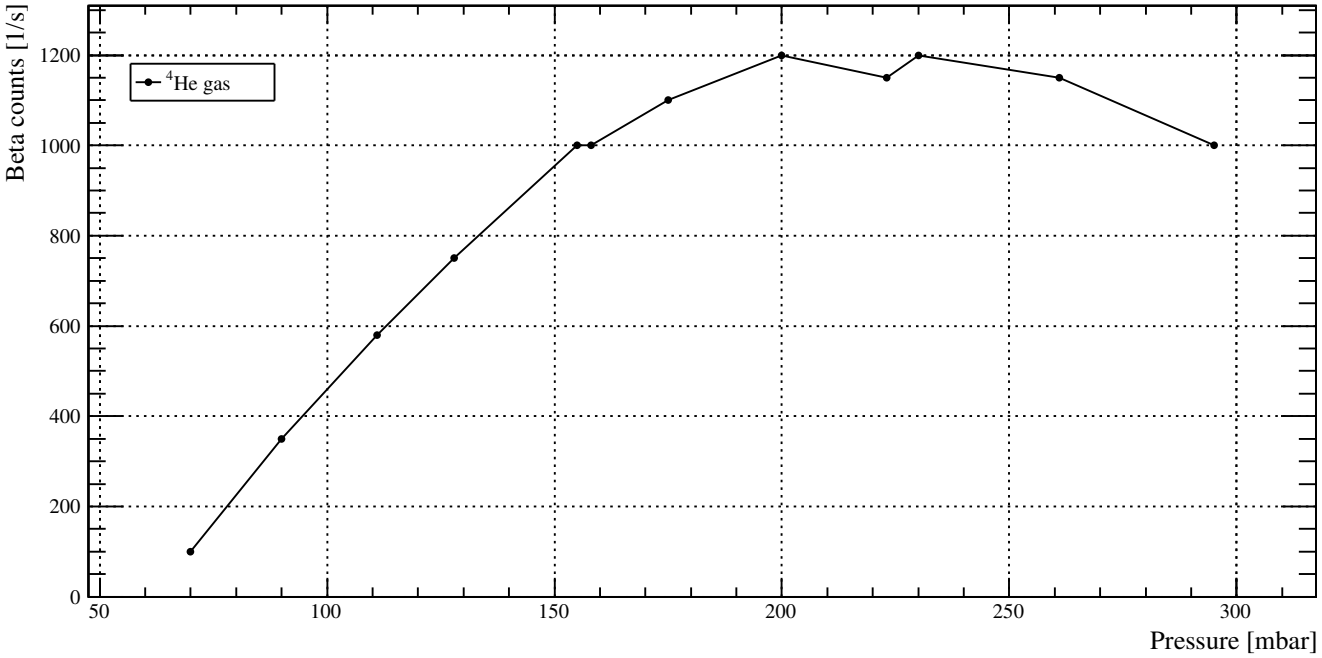

Figure 40. Detected β counts at the SW Si-detector shown as a function of the helium gas pressure in the ion guide. The anomality around 225 mbar can be explained as the measurement was done after all the other data points were measured.

5.1.4 Transmission from the SW to the spectroscopy setup

The ^{20}F experiment took place at the end of the spectroscopy line. A kicker and deflector plates are used to turn the beam to the spectroscopy beamline. After that, there are XY steerers, optical lenses and at the end of the spectroscopy line a second pair of XY steerers. The beamline settings were first optimized to the Faraday cups in the beamline using stable $^{20}Ne^{+}$ ions. After that, the transmission was optimized with radioactive ions by comparing the β counts detected with the SW Si-detector and the β counts detected with the spectroscopy line Si-detector. While optimizing the transmission on radioactive ions the halflife of ^{20}F must be taken into account ($T_{1/2} = 11.163$ s). The transmission from the switchyard to the end of the spectroscopy line with the best target configuration and well optimized beamline elements was determined to be around 72 %. The highest yield measured was 9600 ions/s at SW Si and 5900 ions/s at the spectroscopy line Si, using 3.1 MHz SPIG RF coil, while the primary beam was 10 μA and the helium pressure of the ion guide was 220 mbar. If looking at the highest yield measured and taking into account the efficiency of the Si detector it means that the yield at the SW was around (32000 ± 180) ions/s. The best transmission was around 72 % meaning that at best we

had (23000$\pm$150) ions/s just infront of the spectroscopy setup. This is less than expected 40000 ions/s estimated in the experiment proposal [27].

5.2 Test beamtime for ^{20}F (I218)

In May 2017 we had two days of beam time for ^{20}F at IGISOL to make a test measurement using the whole setup. The spectrometer was moved to the end of spectroscopy line and a carbon foil was placed inside. The shield did not have a positron baffle during this experiment. The measurement was conducted using the Scionix v. 1.0 detector. In this measurement the Scionix detector was biased with a TTi EL561 power supply when the $LaBr_3$ detector was biased with a Ortec 428 detector bias power supply. The K130 cyclotron was used to provide 9 MeV deuteron beam to IGISOL facility.

The IGISOL ion guide was equipped with a fusion ion guide having a BaF_2 foil (thickness 1.2 mg/cm^2). The entrance window had a 52 μm Ta degrader foil to degrade the deuteron beam energy from 9 MeV closer to 6 MeV. The maximum beam intensity could only be 6 μA due to the heating of the ion guide because of the energy deposited in the Ta degrader foil. Due to this problem a cooling system for the Ta window was designed for the experiment in January 2018. For the SPIG coil frequency we used the 3.1 MHz coil which was found to give the best yield during the yield test at the beginning of May 2017. One night of measuring was lost because of an electronic problem at the cyclotron.

During the measurements the vacuum system of the measurement setup had a problem with air leaking into the system. At the beginning of the measurements the pressure at the setup was $3.8 \cdot 10^{-6}$ mbar. Moving the FC (Faraday cup), which was between the spectroscopy line and the spectrometer, leaked air into the vacuum increasing the pressure about one order of magnitude. Poor vacuum lead to a smaller observed β yield at the setup. Quick fixes to the setup were made and the leaking of air could be kept at minimum with only using the FC if necessary.

At the beginning of the test measurement we tried different collimator sizes just before the carbon foil. The carbon foil was 51 μg/cm^2 thick and was used for the stopping of the ^{20}F ions. For fully stopping the 30 keV ^{20}F ions only 58.5 nm of carbon would be needed. Our carbon foil was 226 nm which resulted in stopping the ^{20}F ions comfortably. The biggest collimator size was 15 mm which did not reduce the measured 1.633 MeV γ-ray count rate. With a 9 mm collimator, the measured γ-ray rate was reduced by 16 % and a 6 mm collimator lead to a 49 % to 51 % reduction in the γ-ray rate. These measurements were done on a magnetic field current setting of $I/I_{max} = 28.2$ %. After testing the different collimator sizes we decided to do the measurements using a 9 mm collimator. The reduction can be better seen on the β spectrum shown in Fig. 41.

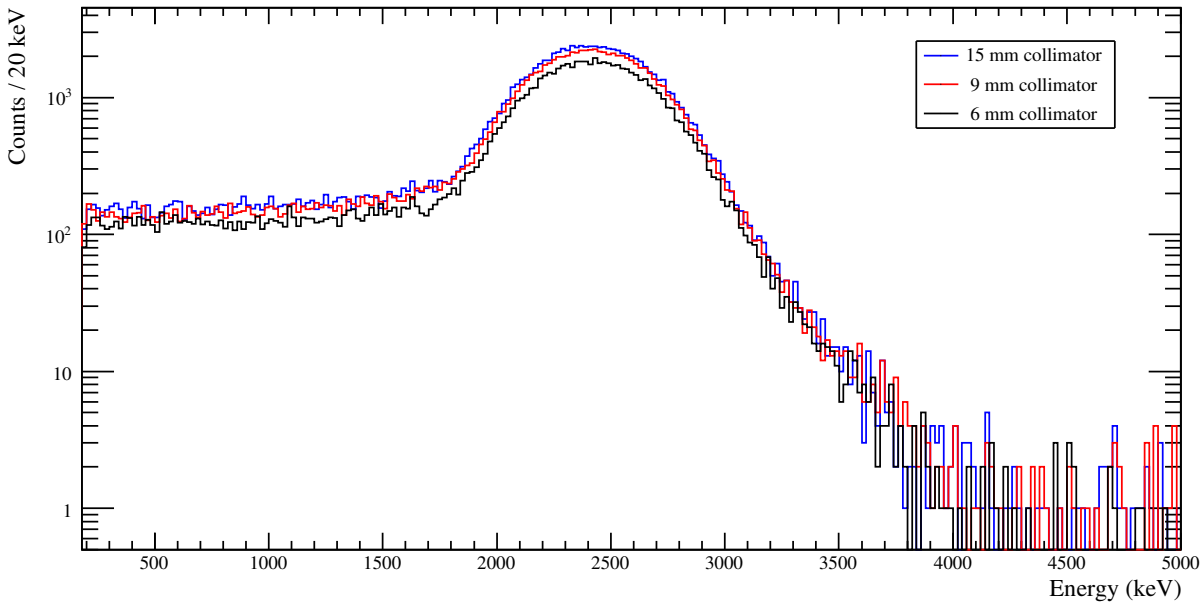

Figure 41. The effect of the collimator size on the ^{20}F β count rate. The measurement was made at a magnetic field setting $I/I_{max} = 28.2$ %. The veto cut condition has not been enabled.

The ^{20}F β decay proceeds mainly to the first excited state of ^{20}Ne (branching of 99.99 %) which is followed by the de-excitation of the state and emission of a 1.633 MeV γ-ray. For monitoring of the ^{20}F yield we used both the β particle rate when it was possible and the intensity of the 1.633 MeV γ-ray peak. The monitored 1.633 MeV γ-ray peak was observed to slowly drift during the experiment. The reason for this was that the bias voltage of the detector was not stable enough. To make the data analysis easier for future experiments (so we did not need to take into account the drifting of the 1.6 MeV peak) a new power supply for the $LaBr_3$(Ce) detector was bought to be used on the actual experiment. An example of a γ-ray spectrum measured during a β measurement on $I/I_{max} = 67.7$ % is shown in Fig. 42. The γ-ray peak at 1.6 MeV was fitted with a Gaussian function with a constant background. The resolution of the $LaBr_3$ detector was then determined by dividing the full width at half maximum (FWHM) by the energy of the γ-ray peak. From the test experiment the calculated resolution was (4.56 ± 0.06) % but the drifting of the γ-ray peak was not accounted for. The main concern we had using the $LaBr_3$(Ce) detector was that the energy resolution would be good enough to separate the 1.633 MeV γ-ray peak from the 1.460 MeV background radiation peak, which is observed because of the ^{40}K in concrete. If looking at measurements made in January 2018 with a more stable bias supply the calculated resolution is around (3.31 ± 0.02) %. Both measured energy resolutions were sufficient enough for separating the two peaks

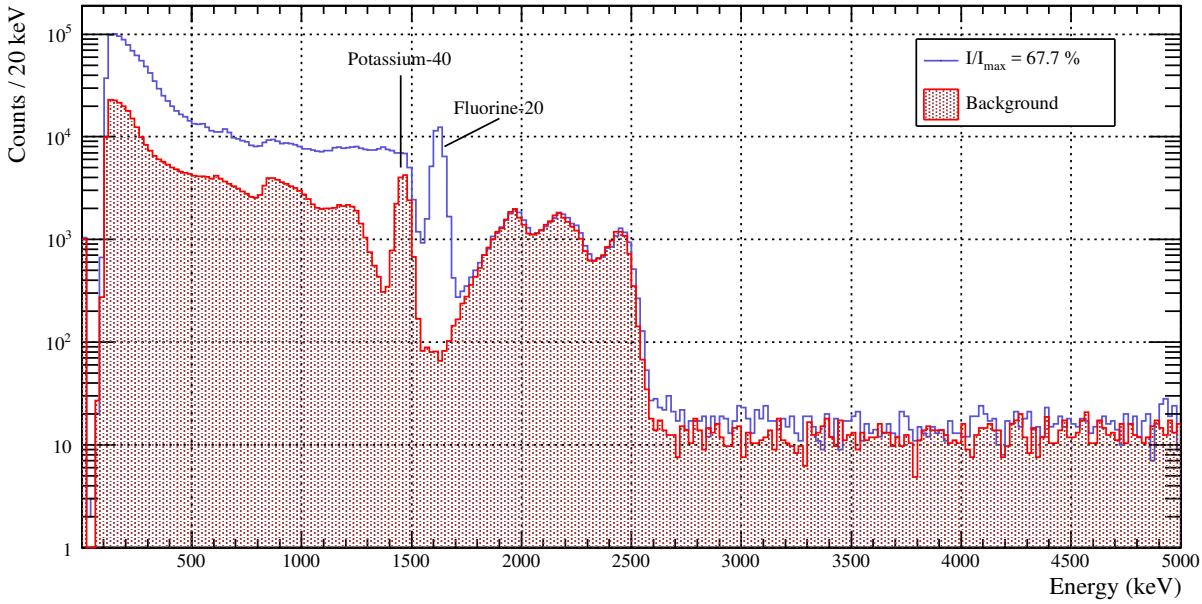

Figure 42. The γ-ray spectrum from the β decay of ^{20}F measured with the $LaBr_3(Ce)$ detector. The measurement was done while measuring electrons with Scionix detector on a magnetic field setting of $I/I_{max} = 67.7$ %. A γ-ray background measurement has been implemented and is marked in red.

from each other. The duration of the measurement in Fig. 42 was around 932 minutes when the compared measurement done in January 2018 was 913 minutes.

In Figs. 43 and 44 a series of measurements with different magnetic field current settings are shown. These measurements were made to measure the full range of ^{20}F β spectrum. In Fig. 43 the measurements are shown without the veto cut condition enabled when in Fig. 44 the veto cut condition is enabled. When comparing these two figures it can be seen that the veto cut condition works sufficiently well on the high energy region. At the signal region enabling the veto cut condition reduces the background radiation by 96 %. After the veto cut condition is enabled on a magnetic field current setting of 35.3 % a clear excess of counts can be seen between the energies of 6 MeV to 7 MeV. This is a result of summing. The measurements of the ^{20}F electron spectrum with different magnetic field current settings were made to validate the GEANT4 simulations. At the highest energies the simulations are not in perfect agreement with the measurements.

During the test experiment we made a longer measurement on a magnetic field current setting $I/I_{max} = 67.7$ % that would focus on the signal area of the second forbidden transition. The duration of the measurement on high magnetic field setting was about 15

hours and the result of this measurement is shown in Fig. 45. In the figure a background run done after the experiment has been implemented and the veto cut condition has been enabled on both the background and the ^{20}F measurements. Around 5 MeV the end tail of the transition to the first excited state can be seen and after that an excess of counts on top of the background radiation. A simulation of the second forbidden transition on similar conditions as in the measurements were done. The simulations showed that the measured excess counts deviated from the distribution that the second

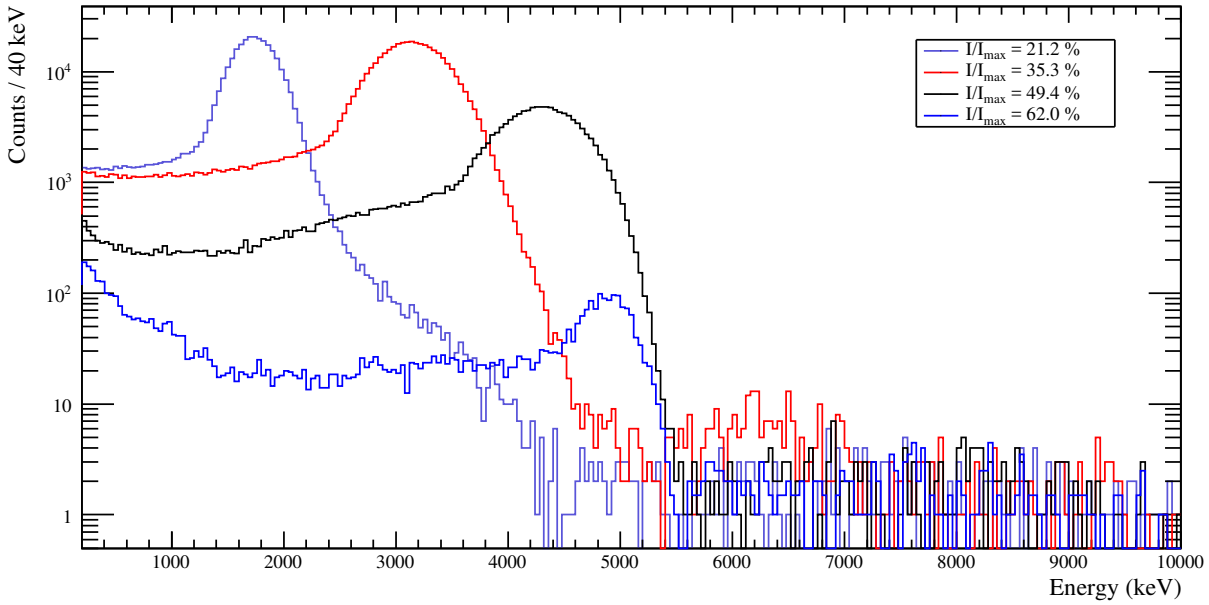

Figure 43. A scan of the ^{20}F β spectrum measured with different magnetic field current settings. All the runs are 15 minutes or scaled to 15 min. The VETO cut condition has not been enabled. The measurements were made with Scionix v.1.0 detector.

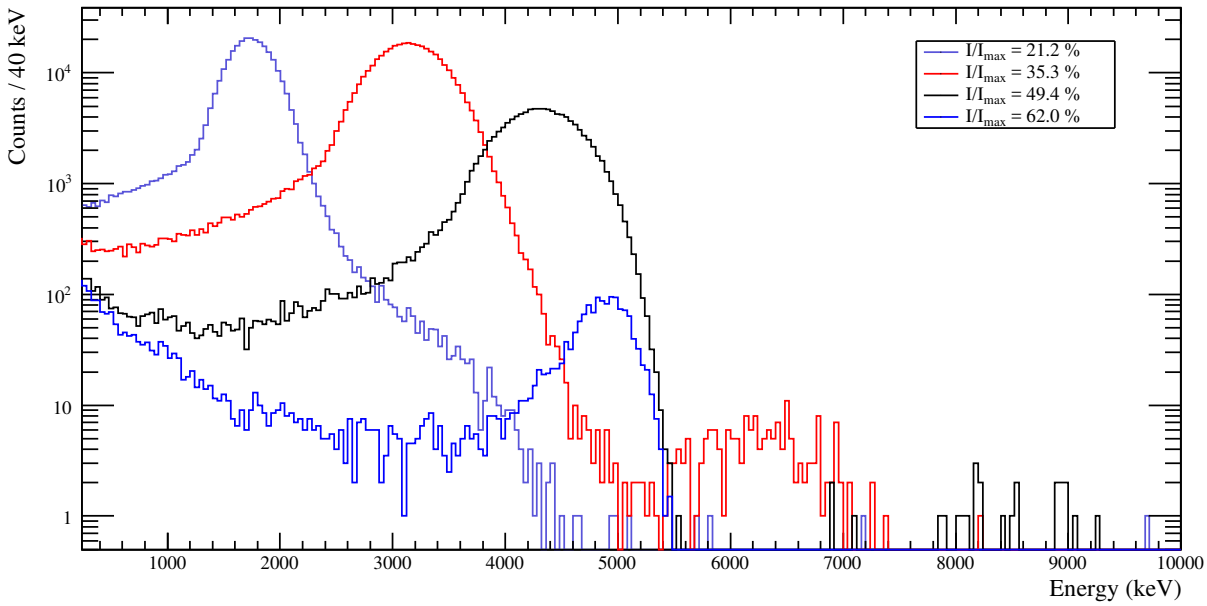

Figure 44. A scan of the ^{20}F β spectrum measured with different magnetic field current settings but the VETO cut condition has been enabled. All the runs are 15 minutes or scaled to 15 min. Measurements were made with the Scionix v.1.0 detector.

forbidden transition would have. Possible reason for this could have been that the simulation was inaccurate. However for lower energies the simulations were in good agreement with the measurements. Another possibility could be a contamination from a β-unstable isotope produced during the experiment. A possible β-unstable isotope which could produce such a shape of spectrum as seen in the measurement could be ^{16}N. The production of a ^{16}N isotope could be possible in ^{19}F(d,p) reaction used. The ^{16}N has a half-life of 7.1 seconds with a β-endpoint energy of 10.4 MeV. For the ^{16}N to get through the mass separation it would have to be in the ammonium form (NH_4^+).

Due to these test measurements improvements to the setup for the January 2018 experminet were made. The magnetic field of the spectrometer bends positrons in a different way than electrons. To get rid of the possibility of postiron emitting β-unstable isotope as a contaminant a positron baffle was placed inside the spectrometer. A new Scionix detector was designed to have even better background radiation supression. The new bias supply for $LaBr_3$ detector was bought and the water cooling for the degrader foil was designed.

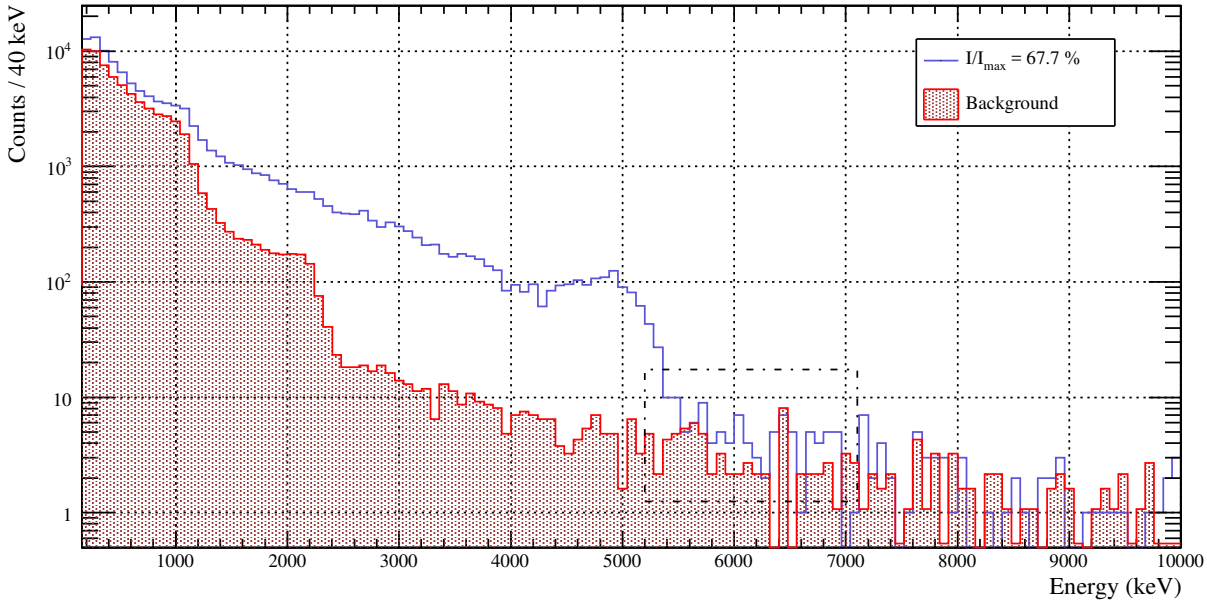

Figure 45. A part of the electron spectrum measured with the Scionix detector on a magnetic field current setting of $I/I_{max} = 67.7$ %. The signal area of interest has been highlighted with a box. The VETO cut condition has been enabled.

5.3 β-decay study of ^{20}F (I230)

The experiment to detect the second-forbidden, non-unique, transition to the ground state in the β decay of ^{20}F was done in January 2018. The results of the experiment are discussed in more detail in Ref. [30]. Since this MSc thesis work focuses on the development work for the actual measurement, the results are discussed here only briefly.

A similar target foil of BaF_2 with a thickness of 1.2 mg/cm^2 was used as in the test experiment. The thickness of the Ta window was 82 μm and it was attached to a water cooled Cu window frame. Between the Ta degrader foil and the ion guide a 100 μm steel separation plate was used to reduce the conduction of heat towards the ion guide. The deuteron beam energy used was again 9 MeV. The duration of the beam time was nine days from which eight days were spent on measuring on ^{20}F beam and one day on ^{12}B beam. The ^{12}B beam was produced with a 0.5 mg/cm^2 ^{11}B target via ^{11}B(d,p)^{12}B reaction. The target was changed to a new ion guide head and it was used without a degrader foil. During the experiment the 3.1 MHz SPIG RF coil was used while the ion guide helium pressure varied between $279-298$ mbar. The settings used in MC^2-analyzer on the Scionix v.2.0 detector and $LaBr_3$ detector for the measurements done on the ^{20}F beam during the experiment are shown in table 5. The spectrometer setup has been described in more detail in chapter 3.2.

The Scionix v. 2.0 detector had a malfunction on the 3rd day of beam when a bias regulator on the built-in amplifiacation board broke. For the while that the Scionix v. 2.0 detector was under examination to find the malfunctioning component and to fix it, the Scionix v. 1.0 detector was placed inside the spectrometer. We changed to a ^{12}B beam to make measurements that show that the spectrometer works as expected. The ^{12}B was used for this measurement for three different reasons: 1) the end-point energy has a value of (13.3693 ± 0.0013) MeV [11] which allows us to test the spectrometer at the higher energies, 2) the decay from the ground state of ^{12}B to the ground state of ^{12}C proceeds via an allowed transition providing a lot of statistics (branching of 97.22 %) and 3) the yield of ^{12}B is good when a 9 MeV deuteron beam is used (measured just before the spectroscopy setup to be around $37 \cdot 10^3$ ions/s). The target was changed from BaF_2 to ^{11}B and a 9 MeV deuteron beam was still used. The ^{11}B target was 0.5 mg/cm^2 thick using a new ion guide head with no degrader foil with a reaction of $^{11}B(d,p)^{12}B$. We spent one day measuring with the ^{12}B beam. As a result of using the v. 1.0 we could not do the $E - \Delta E$ cut when substracting the background radiation. The measurement showed that the spectrometer works as it was expected. Figure 46 shows the electron spectrum from ^{12}B β decay with three different magnetic fields.

With the ^{20}F beam, the measurements started with similar scans through different magnetic field current settings as in the test experiment in May 2017. These were done to validate and check that the spectrometer and the Scionix v. 2.0 detector work as expected. These were followed by long measurements with high magnetic field current settings I/I_{max} = 67.7 % and I/I_{max} = 79 %. A figure of the long measurements are shown in fig. 47 with the different background radiation cuts.

The measurement made on I/I_{max} = 67.7 % was carving out the part of the electron spectrum where the high-energy tail of the second-forbidden transition would be. The measurement conducted on I/I_{max} = 79.0 % was focused on a part of the elctron spectum where no part of the second-forbidden transition should be seen. The energy cut has been defined by how much energy electrons deposit in the front detector. In fig. 47a) an excess of counts can be seen at the signal area of 5.6 MeV to 6.6 MeV as would be expected from the second-forbidden transition. The distribution of the counts agrees with the simulations. This is different from the experiment in May 2017 employing the old Scionix v. 1.0 detector for which $\Delta E - E$ selection could not be done. A more detailed analysis has been conducted in Ref. [30].

The experiment was a success at determining the branching ratio of the second-forbidden transition resulting in the strongest second-forbidden, non-unique, transition detected.

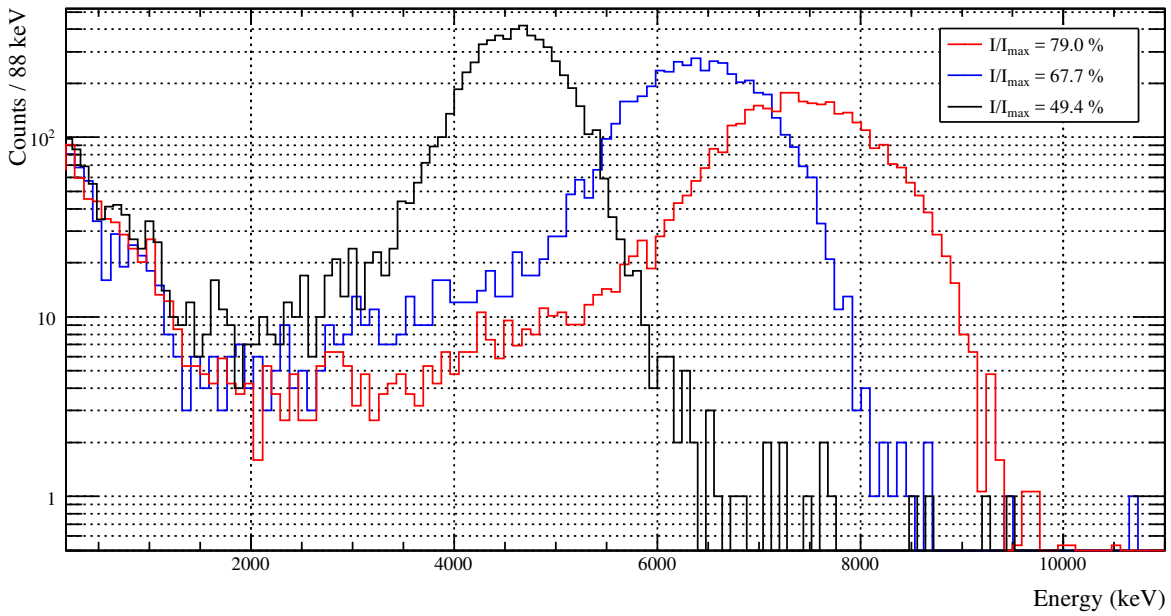

Figure 46. The measurement made with Scionix v. 1. 0 of the ^{12}B beam to validate that the spectrometer works correctly. ^{12}B has a β decay endpoint energy of 10.4 MeV. The VETO cut condition has been enabled.

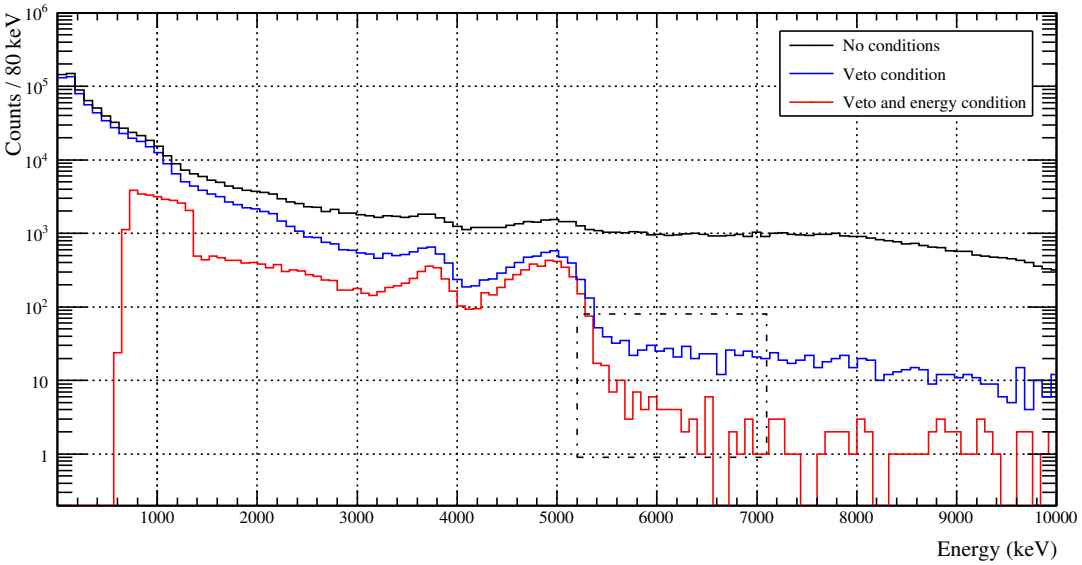

(a) The β spectrum from the β decay of ^{20}F measured on magnetic field current setting of $I/I_{max} =$ 67.7 %. The duration of the measurement was around 67 hours.

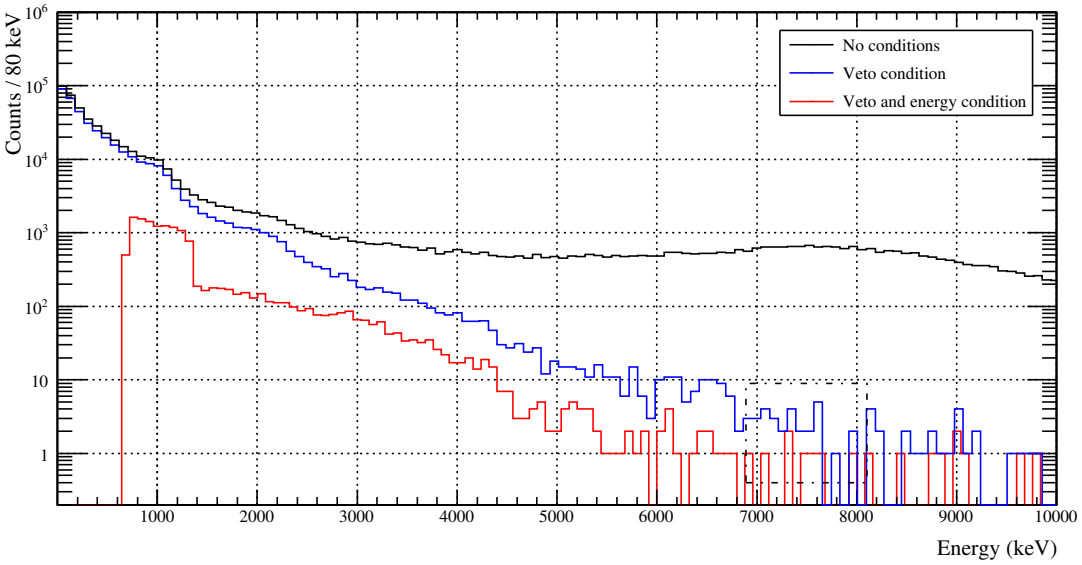

(b) The β spectrum from the β decay of ^{20}F measured using the magnetic field current setting of $I/I_{max} = 79.0$ %. The duration of the measurement was around 38 hours.

Figure 47. Long measurements of the ^{20}F β spectrum with two different magnetic field current settings.

Table 5. Settings for both detectros and their channels. The Scionix detector was placed on channels 0 (SIGNAL), 1 (VETO) and 3 (FRONT) while the 2 channel was for $LaBr_3$ detector.

Setting	Ch0 SIGNAL	Ch1 VETO	Ch2 LABR	Ch3 FRONT
Input Signal				
DC Offset	1786	1787	15370	1898
Input range	-	-	-	-
Decimation	1	1	1	1
Digital Gain	1	1	1	1
Impedance	50	50	50	50
Pulse Polarity	NEG	NEG	POS	NEG
Trigger				
Threshold	30	40	180	30
RC-CR2 Smooth.	16	16	16	16
Trigger Holdoff	2.00	3.50	2.40	2.00
Input Ride Time	0.25	0.25	0.20	0.25
RT Val. Width	0.00	0.00	0.00	0.00
Energy Filter				
Baseline mean	1024	1024	16384	1024
Trapezoid Gain	1.00	1.00	1.00	1.00
Trap. Rise Time	4.00	4.00	7.00	4.00
Decay Time	1.10	1.10	1.40	0.42
Trap. Flat top	1.50	1.50	1.50	1.50
Flat Top Delay	60.00	60.00	60.00	60.00
	Man	Man	Man	Man
Peak Mean	1	1	1	1
Baseline Holdoff	1.00	1.00	2.00	1.00
Peak HoldOff	2.00	2.00	5.00	2.00

6 Discussion

The main motivation behind this thesis work was to characterize the setup used for the experiment to determine the branching ratio of the second-forbidden, non-unique transition between the ground states of ^{20}F and ^{20}Ne and to give a brief overview of the experiment. The experimental setup consisted of a Siegbahn-Slätis type of intermediate image spectrometer, a Scionix plastic scintillator and a $LaBr_3$(Ce) detector.

For the detection of the β particles a Scionix plastic scintillator was used at the end of the spectrometer. The first version of the Scionix plastic scintillator was tested and discovered to give insufficient background radiation prevention. Test measurements involved measurements with a ^{207}Bi source, background radiation measurements underground at the Pyhäsalmi mine, lead shielding tests and many hours of background radiation measurements. After the test beamtime for ^{20}F was conducted the second version of the Scionix plastic scintillator detector was produced. This detector was like the Scionix version 1.0 with having a VETO detector around the inner signal detector. However, in the Scionix v.2.0 the inner signal detector had been divided into two parts: a thin front detector and the signal detector. This provided us enough protection from the background radiation. For measuring the γ-rays from the de-excitation of the first excited state of ^{20}Ne we used a $LaBr_3$(Ce) detector. The main concern in our experiment when using the $LaBr_3$(Ce) detector was the energy resolution. The emitted γ-ray had the energy of 1.633 MeV while the major background radiation emission was from ^{40}K at 1.460 MeV. The energy resolution (FWHM) of $LaBr_3$(Ce) detector was measured to be (3.31 ± 0.02) % which was sufficient to separate the 1.633 MeV peak from the ^{40}K background radiation peak. The magnetic field of the spectrometer was measured to ensure the 18K coil configuration.

After the preparations on the experimental setup the production of ^{20}F was tested at IGISOL. The beam was produced via ^{19}F(d,p)^{20}F reaction using 9 MeV deuterons from the K-130 cyclotron on a thin BaF_2 target. TALYS calculations indicated that the optimal production of $^{20}F^{+}$ ions would be with deuteron beam energies of $4 - 6$ MeV thus we needed a degrader foil to lower the beam energy. Measurements on different degrader foil thicknesses were made leading to the highest production of ^{20}F with a 52 μm Ta degrader foil. At IGISOL there are three different SPIG RF coils with frequencies of 2.8 MHz, 3.1 MHz and 5.6 MHz. A measurement testing the optimal SPIG RF frequency coil was made resulting for the highest production of ^{20}F with the 3.1 MHz coil. Also the helium

pressure of the light ion guide was optimized to give the highest production rates around 225 mbar.

With the measurements of the ^{20}F production done a test beam time for the whole setup was done at the end of May 2017. First the whole β decay spectrum of ^{20}F was measured by doing short scans of the spectrum with different magnetic field settings. Second a longer measurement was made on a high magnetic field setting which corresponded to the β decay energy around the signal area of the second-forbidden, non-unique transition. During the 2 days of beam time we did not detect the transition even though we detected an excess of counts at the signal area. These were believed to be from a contamination because the distribution of the counts did not correspond to the simulated (GEANT4) distribution for the second-forbidden, non-unique transition. During the test experiment it was noticed that the power supply of the $LaBr_3$(Ce) detector was unstable leading to a travelling γ-ray peak. This was taken into account for the next experiment by purchasing a new more stable power supply.

The experiment performed in January 2018 lead to the successful determination of the second-forbidden, non-unique, ^{20}F ground state to ^{20}Ne ground state transition strength which has been reported in more detail in the publication by O.S. Kirsebom et al. in Ref. [30]. Still in the making are at least two more publications: the impact of the now measured transition strength on the astrophysical sites and a Nuclear Instrumentation Methods publication of the experimental setup.

The experimental setup has been characterized and proven to be a well working setup. In the future the setup could be used for similar kind of online measurements of similar ground-state to ground-state low background transitions or for example coincidence measurements of electron-positron pair production. The Siegbahn-Slätis spectrometer has been used previously on conversion-electron measurements and could be used on these type of measurements again [28]. A similar measurement as we have done could be repeated at an underground laboratory for eliminating the biggest background radiation source: cosmic rays. The spectrometer setup will be presented within the next users meeting of the Accelerator Laboratory of the University of Jyväskylä.

References

[1] G. Martinez-Pinedo et al. *Phys. Rev. C*, 89:045806, (2014).

[2] F.P. Calaprice and D.E. Alburger. *Phys. Rev. C*, 17, (1978).

[3] C. Iliadis. *Nuclear Physics of Stars, Second, Revised and Enlarged edition.* Wiley-VCH, Einheim. Germany, 2015.

[4] H. Karttunen et al. *Fundamental Astronomy.* Springer, 2007.

[5] NASA. `https://www.nasa.gov/`. Refered: 1.10.2018, pictures of stellar cloud, small/medium/large star and black hole.

[6] ESO. `https://www.eso.org/public/images/`. Refered: 1.10.2018, pictures of white dwarf, neutron star (by L.Calcada), planetary nebula (by ESO/VISTA: J.Emerson. Acknowledgment: Cambridge Astronomical Survey Unit), red giant (by M.Kornmesser) and supernova.

[7] S. Jones et al. *Astr. & Astrophys.*, 593:A72, (2016).

[8] K. Nomoto et al. S. Miyaji. *Pub. Astron. Soc.*, 32:303–329, (1980).

[9] J. Schwab et al. *Mon. Not. R. Astron. Soc.*, 453:1910–1927, (2015).

[10] H. Möller. *Evolution of Degenerate Oxygen-Neon Cores.* PhD thesis, Technische Universität Darmstadt, Darmstadt, 2017.

[11] W.J.Huang et al. The atomic mass evaluation. `https://www-nds.iaea.org/amdc/`. Refered: 1.10.2018.

[12] K.S. Krane. *Introductory Nuclear Physics.* Wiley, 1987.

[13] J. Suhonen. *From Nucleons to Nucleus. Concepts of Microscopic Nuclear Theory.* Springer, Berlin Heidelberg, 2007.

[14] W.R. Leo. *Techniques for nuclear and particle physics experiments: a how-to approach.* Springer, New York, 1987.

[15] M. Haaranen. *Rare beta decays and the spectrum-shape method.* PhD thesis, Department of Physics ,University of Jyväskylä, Jyväskylä, 2017.

[16] M. Pfützner et al. *Rev. Mod. Phys.*, 84:568–619, (2012).

[17] B. Singh et al. *Nucl. Data Sheets*, 84:487–563, (1998).

[18] D.R. Tilley et al. *Nucl. Phys. A*, A 636:249–364, (1998).

[19] Evaluated Nuclear Structure Data Files. `https://www-nds.iaea.org/`. Refered: 23.9.2018.

[20] M. Hughes et al. *Phys. Rev. C*, 97:054328(10), (2018).

[21] J.Äystö et al. *Three decades of research using IGISOL technique at the University of Jyväskylä*. Springer Netherlands, Dordrecht, 2014.

[22] I.D. Moore et al. *Hyperfine Interactions*, (223):17–62, (2014).

[23] I.D. Moore et al. *Nuclear Inst. Meth. B*, (317):208–213, (2013).

[24] P. Karvonen. *Fission yield studies with SPIG-equipped IGISOL: A novel method for nuclear data measurements*. PhD thesis, Department of Physics ,University of Jyväskylä, Jyväskylä, 2010.

[25] P. Karvonen et al. *Nucl. Inst. Meth. B*, 266:4794–4807, (2008).

[26] Root Data Analysis Framework. `https://root.cern.ch/`. Refered: 14.9.2018.

[27] O.S. Kirsebom et al. Determination of the strength of the second-forbidden transition between the ground states of ^{20}f and ^{20}ne (i218). (2016). Proposal to the JYFL PAC (unpublished).

[28] J. Kantele et al. R. Julin. *Nucl. Inst. Meth. A*, 270:74–77, (1988).

[29] V. Nieminen. MSc. *Siegbahnin-Slätisin beetaspektrometrin muuttaminen Si(Li)-yhdistelmäspektrometriksi*. Jyväskylä, Department of Physics, University of Jyväskylä, 1984.

[30] O.S. Kirsebom et al. (2018). submitted to Physics Letters B, arXiv: 1805.08149v1.

[31] Scionix Holland. `https://scionix.nl/`. Refered: 3.9.2018.

[32] ESTAR. National Institute of Standards and Technology. `https://physics.nist.gov/PhysRefData/Star/Text/ESTAR.html`. Refered: 14.9.2018.

[33] J.B. Birks. *The Theory and Practice of Scintillation Counting*. Pergamon Press, 1964.

[34] G.F. Knoll. *Radiation Detection and Measurement*. John Wiley & Sons, Inc., New York, 1989.

[35] Saint-Gobain crystals. `https://www.crystals.saint-gobain.com/`. Refered: 7.9.2018.

[36] Caen *Technical Information Manual*. Revision n. 11. 11.3.2015.

[37] Caen *MC^2 Analyzer User Manual (UM3182)*. Revision 2. 4.11.2016.

[38] W. H. Trzaska. *Nucl. Inst. Meth. A*, 297:223–229, (1990).

[39] Callio Lab. `https://calliolab.com`. Refered: 21.5.2018.

[40] National Nuclear Data Center. `http://www.nndc.bnl.gov/chart/`. Refered: 30.10.2017.

[41] M. J. Martin. *Nucl. Data Sheets*, 114:1497, (2013).

[42] F.G. Kondev and S.Lalkovski. *Nucl. Data Sheets*, 112:707, (2011).

[43] E. Browne and J.K. Tuli. *Nucl. Data Sheets*, 108:2173, (2007).

[44] E. Browne and J.K. Tuli. *Nucl. Data Sheets*, 114:1849, (2013).

[45] A. Khanam. MSc. *Yield measurements at IGISOL with a digital data acquisition system*. Jyväskylä, Department of Physics, University of Jyväskylä, 2017.

[46] TALYS. `http://www.talys.eu/home/`. Refered: 2018.

Appendices

Appendix 1: Research training work: Testing Scionix plastic scintillator detector and $LaBr_3$ γ-ray detector

Appendix 1:

marjut.h.hukkanen@student.jyu.fi

Testing Scionix plastic scintillator detector and $LaBr_3$ γ-ray detector

Author: Marjut Hukkanen
Supervisor: Anu Kankainen
Research Training, 21.12.2017

Abstract

In this research training work, I tested a plastic scintillator detector and a $LaBr_3$ γ-ray detector in the Accelerator Laboratory of the University of Jyväskylä (JYFL-ACCLAB). A short introduction of the nuclear astrophysics related to this detector testing is given. The measurements that have been made to characterize the detectors are described and obtained result discussed. The characterization has been successful for both detectors. The cosmic ray suppression efficiency of the veto detector with a high veto trigger setting was around 98.5 % at the time of testing. This research training work is a part of the MSc studies at the Department of Physics in University of Jyväskylä.

Contents

1 Introduction and Motivation

After carbon burning stage the $8 - 10\ M_{\odot}$ stars develop electron-degenerate ONe cores. Nuclear burning in surrounding shells or mass transfer from a nearby star will keep the core growing until the Chandrasekhar limit of 1.4 $M_{\odot}$ is reached. After this the electron-capture reactions start on ^{24}Mg and ^{20}Ne causing reduction on both electron pressure and the mean mole number of electrons. These reactions heat the core up to a temperature where the oxygen burning can start, triggering a ^{16}O+^{16}O thermonuclear runaway. The effect of this thermonuclear runaway depends on the oxygen ignition density: a complete or partial disruption of the star in lower densities or a collapse into a neutron star in higher densities. [1, 2]

Martínez-Pinedo et al. [3] have suggested that in an important temperature-density range the second forbidden, non-unique, transition between the ground states of ^{20}Ne and ^{20}F would dominate the electron-capture rate. The strength of this transition can be determined from the branching ratio of the inverse transition in the β-decay of ^{20}F. A schematic β-decay scheme of ^{20}F is shown in figure 1. The transition between the ground states ($2^+ \rightarrow 0^+$) has only been measured assuming an allowed shape and a upper limit of $< 0.001\%$ was achieved [4]. The allowed transition $2^+ \rightarrow 2^+$ will dominate the β-spectrum below the energy of 5.4 MeV and cover most of the weaker second-forbidden transition. The second forbidden ground-to-ground state transition can be observed in a energy range from 5.4 MeV to 7.0 MeV, which contains about 10 % of the decay's emission strength [6].

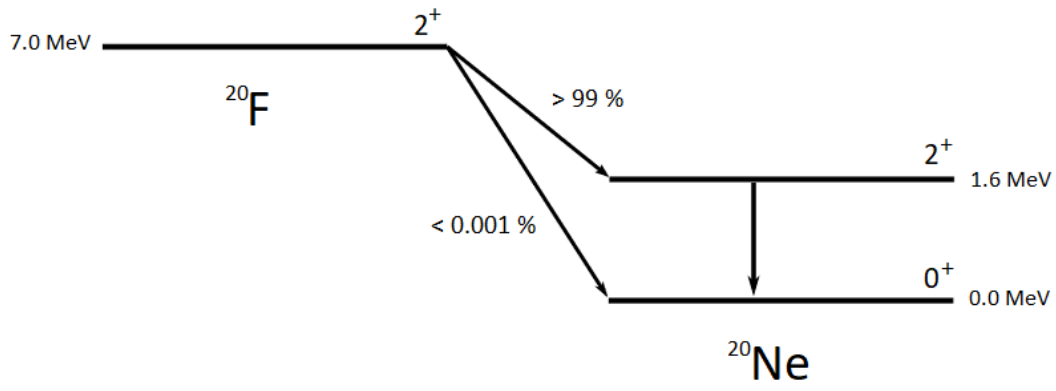

Figure 1. Decay scheme of ^{20}F β-decaying to ^{20}Ne. The half-life of ^{20}F is $T_{1/2} = (11.163 \pm 0.008)$ seconds. [5]

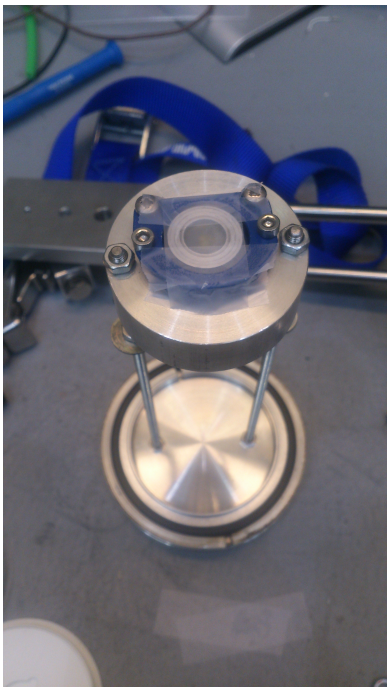

Figure 2. On left is the spectrometer that is used for guiding the electrons [7]. On right is a source holder used during the test measurements with different sources.

We aim to measure the branching ratio by transporting the electrons using a Siegbahn-Slätis intermediate-image spectrometer shown in figure 2 on left. The magnetic transporter was built in 1980s in Jyväskylä for in-beam conversion-electron spectroscopy [8]. The magnetic field transports electrons of interest to a Scionix plastic-scintillator detector situated at the end of the spectrometer. The signal region for measuring the ground-to-ground state transition is between energies 5.4 MeV to 7.0 MeV. Inside the spectrometer there is a shield with a $LaBr_3$ detector which is used to measure the 1.6 MeV γ-rays from the ^{20}F β-decay. This can be used for normalization. Both of the detectors will be described in more detail later on this report. For data acquisition we use Caen DT5724B digitizer and Caen MC^2-analyzer program.

In this report I describe the test measurements that have been done to characterize both detectors. For testing and optimizing the settings of the detectors we have used different sources on a holder, shown in figure 2 on right, at one end of the spectrometer. A list of measurements we have done for testing the detectors is listed in a table 1 in appendix 1.

2 Electron detection with Scionix detector

For electron detection we used a plastic scintillator, called signal detector, that is surrounded by another plastic scintillator, called veto detector, which is used to detect and veto the cosmic rays. The inner signal detector is a Scionix EJ200 plastic scintillator with diameter and height of 45 mm. The entrance window of the signal detector is made of aluminized mylar and has a thickness of 6 μm. The veto detector is a Scionix EJ200 plastic scintillator with a 55 mm diameter and 75 mm height. The veto detector has an axial well that has diameter of 46 mm and is 60 mm deep so that the signal detector can fit inside the veto detector. The whole Scionix detector is shown in figure 3.
The Scionix detector was set to Caen digitizer so that the signal detector was attached to channel 0 and the veto detector to channel 1. The settings of both detectors were controlled using MC^2-analyzer.

Figure 3. The Scionix plastic scintillator detector with the light tight cover [7].

We studied the detectors signal and veto pulses on Tektronix TDS 2024C oscilloscope. This measurement was made using ^{207}Bi source with the magnet's current set at $I/I_{max} = 13.5\%$. We could see that when an electron induces a pulse in the signal detector of Scionix there is also a pulse induced in the Scionix veto detector. From figure 4 we can notice that the signal pulse is about 60 mV and the induced veto pulse is around 15-20 mV. This means that the veto detector's trigger threshold has to be set so that it does not trigger on these cross-talk pulses. In figure 5 the crosstalk effect is shown with plotting the Scionix veto data as a function of Scionix signal data. It can be seen that there is a line under which the cross-talk does not happen. That must be taken into account while analyzing the data.

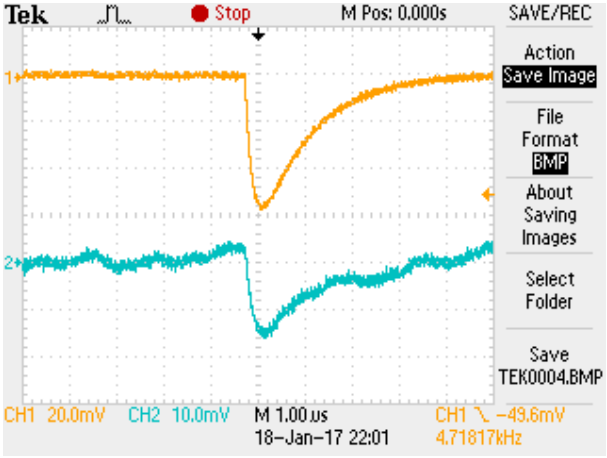

Figure 4. A figure from the oscilloscope with Scionix signal in channel 1 and Scionix veto in channel 2.

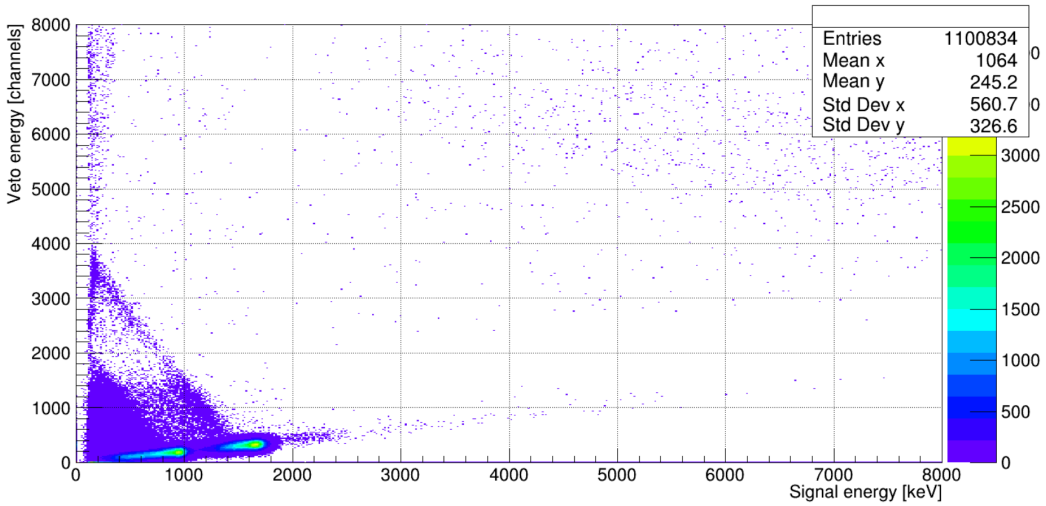

Figure 5. A figure to show the effect of cross-talk when measuring using a ^{207}Bi source while the magnetic field is set to $I/I_{max} = 20\%$.

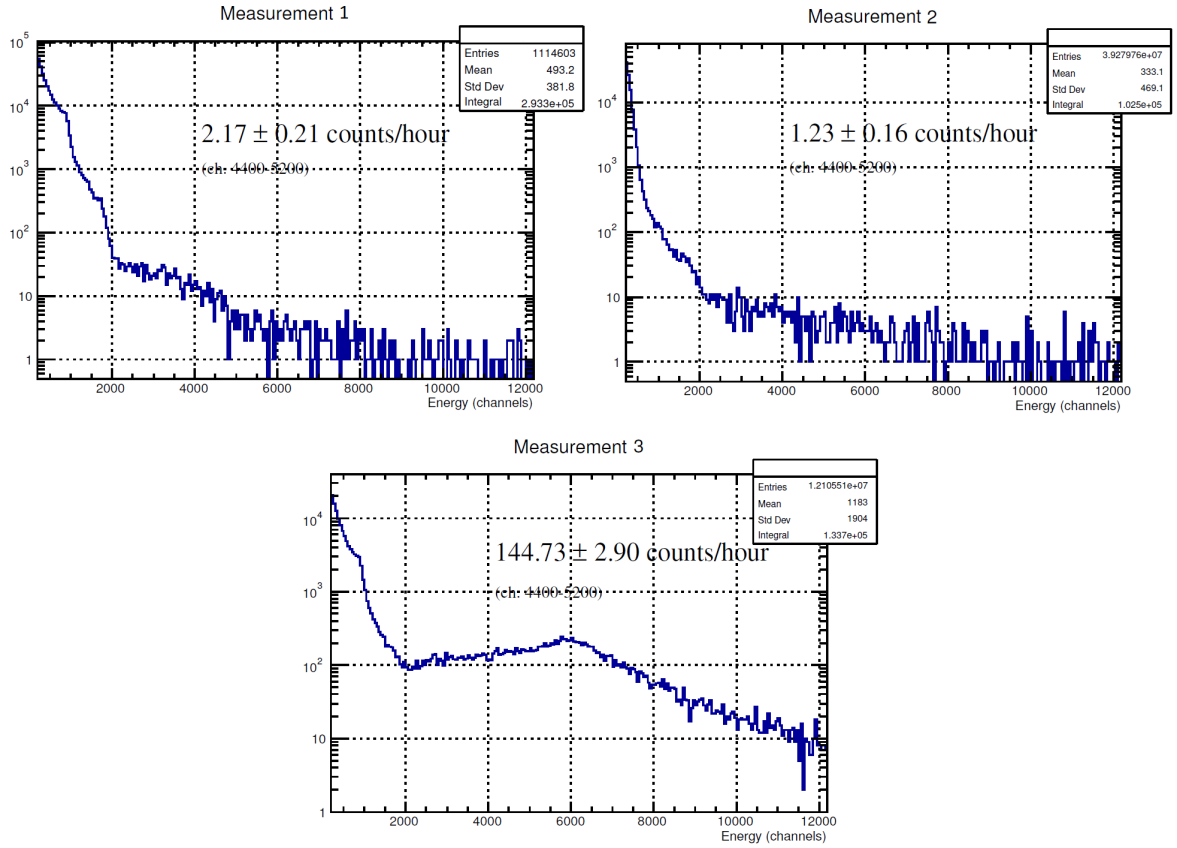

Figure 6. Measurement 1 has veto detectror's trigger threshold set to high setting of 610 LSB when in measurement 2 we have chosen a low veto trigger threshold setting of 40 LSB. Measurement 3 was made for comparison of the background count rate without cosmic-ray supression (by disabling the veto detector).[9]

Background measurements were done inside the spectrometer with different veto trigger threshold settings. All measurements were done in vacuum. There was a setting of "high veto threshold" that was 610 LSB. It means that the trigger threshold has been set high to not trigger on cross-talk pulses. The "low veto threshold" is 40 LSB and is just above the noise level. There was also a measurement done with no veto condition enabled. These measurements are shown in figure 6 respectively. When comparing the count rates from measurement done with high veto threshold (measurement #1) and without veto (measurement #3) the suppression of cosmic rays is 98.5 %.

To test the electron detection on Scionix detector and the magnetic field of our spectrometer we made magnetic field scans. In these kind of scans we measured the same amount of time and changed the current of the magnet. With different magnetic field settings we could see the peak moving, meaning we could select which energy electrons we wanted to see on our detector.

The characterization of the Scionix detector was continued by building a lead cave around

the Scionix detector to see how the 5 cm of lead shielding would reduce the detected background radiation. The lead cave is shown in figure 7. Scionix was placed inside a Ge-detector cup to protect the detector. This is shown in figure 8. We also protected the detector from light by placing a black light tight cover over the entrance window. To make sure that no light could interfere with our measurement we covered the lead cave with a black plastic bag. Inside the lead cave we measured for 48 hours and this is marked with a red line in figure 9. With blue is marked a background measurement that was made without any lead shielding straight after the lead cave measurement. The background measurement is scaled to be 48 hours. From comparing these two we can notice that around our signal region of 5.4 - 7.0 MeV, the reduction with lead shielding is not much. This means that if we wanted to shield the detector with lead it would not help much to reduce the background and would complicate our setup greatly.

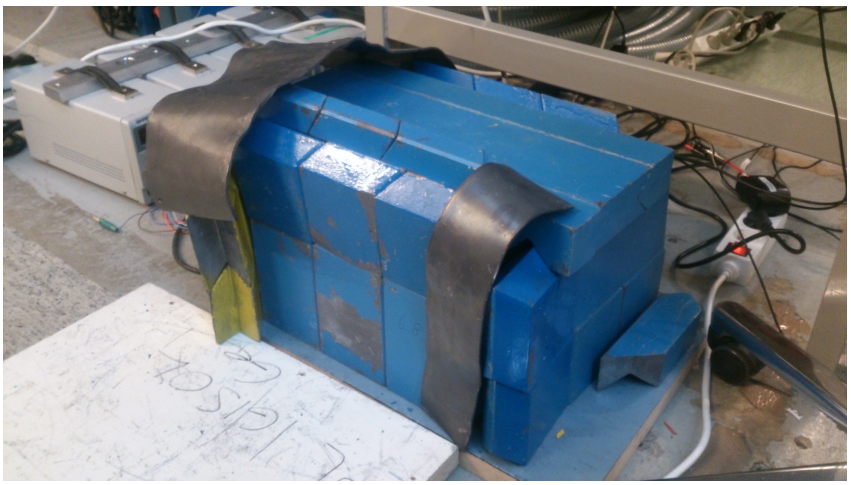

Figure 7. Scionix detector is placed inside a lead cave for a background radiation measurement.

Figure 8. Scionix detector was protected with a Germanium detector -cup inside the lead cave.

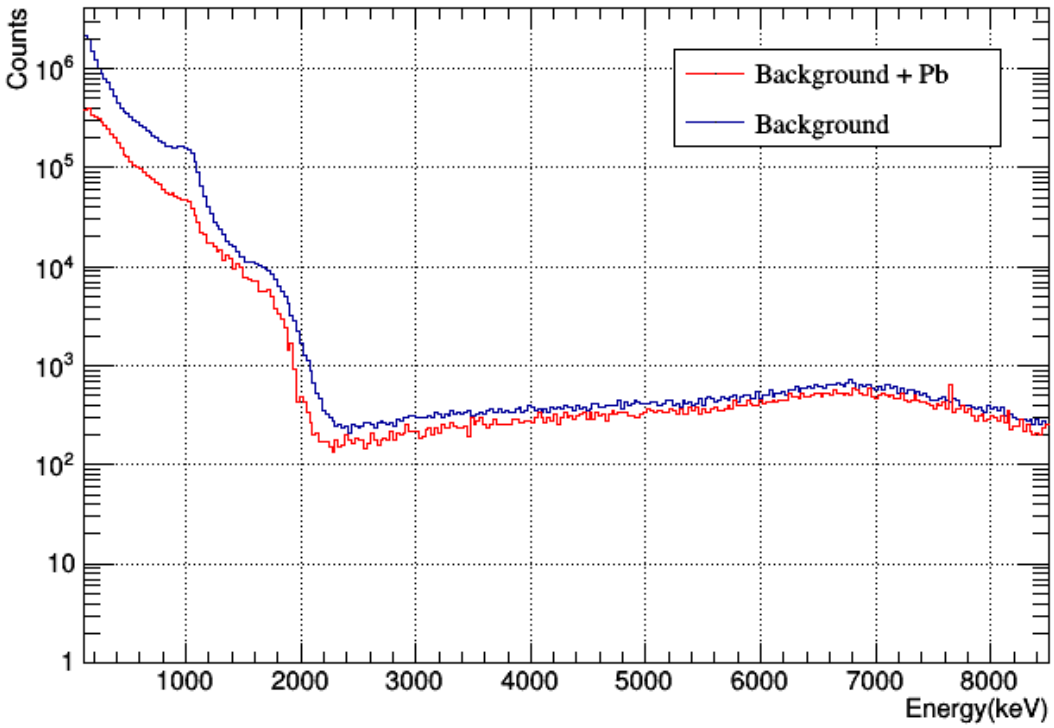

Figure 9. 48 hours long measurement with Scionix detector of the background radiation where the red line shows the background radiation with the 5 cm lead shielding and the blue line shows the background radiation without a lead shielding.

3 γ-ray detection with $LaBr_3$ detector

For γ-ray detection we used a detector that had a $LaBr_3$ crystal coupled to a silicon photomultiplier (SiPM). $LaBr_3$ crystal had a diameter of 25.5 mm and length of 38.5 mm. The $LaBr_3$ detector will be implemented on a brass shield in the middle of the spectrometer on the measurement setup. The shield is used to protect the Scionix detector from the γ-rays.

To bias the LaBr-detector we used two different power supplies: for measurements before May 2017 we used iSeg NHS 6 001p and on the efficiency calibration measurements we used Ortec 428 power supply. The optimal bias voltage for $LaBr_3$ detector was between 25.5 V - 30.0 V, we decided to use bias voltage of +28.5 V. The instability of the Ortec 428 power supply could be noticed as a shift of 5-20 keV in the measured γ-ray spectra peaks. If needed this shift has been taken into account on for example calculating the efficiencies.

The $LaBr_3$ was attached to the channel 2 of Caen digitizer and was controlled using MC^2-analyzer. The analyzer settings were set using a ^{60}Co source and this could be done online. The detector had to be covered from any possible light sources and that was achieved by setting the detector inside a light tight box as shown in figure 10.

We have made different test and characterization measurements with the $LaBr_3$ detector both inside and outside of the spectrometer. The measurements are listed on table 1 in appendix 1. In the final measurement setup the γ-ray detection is going to be used for normalization.

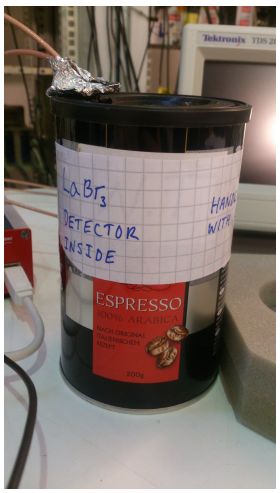

Figure 10. $LaBr_3$ detector inside a light tight box.

Figure 11. A figure of a background measurement made with $LaBr_3$ detector.

A spectra of a background measurement with the LaBr detector inside the spectrometer is shown in figure 11. The peak of 1.46 MeV ^{40}K, that is caused by the surrounding concrete of the laboratory, is clearly seen around 1500 keV. This tells us that the energy calibration is not exactly correct yet, but can be easily corrected in ROOT.

Efficiency calibration measurements for the γ-ray detector inside the spectrometer were done in June 2017. In figure 12 is shown a spectrum measured using a ^{152}Eu source. In the figure a peak around 750 keV has been identified to be the 778 keV γ-ray peak of ^{152}Eu and has been fitted with a modified gaussian function to get a measure of the counts. With using the number of counts, time of the measurement and the intensity of 778 keV γ-peak the activity can be calculated. The observed activity can be calculated:

$$A_{obs.} = \frac{N_\gamma}{t_{measured} \cdot I_\gamma}, \tag{1}$$

where $N_\gamma = (11643.3 \pm 684.509)$ counts is from the fit of the peak, $t_{measured}$ is the time of the measurement that was in this measurement 4 hours and I_{gamma} is the intensity of the transition. I_γ for the 778 keV line is 12.93(8) % [5]. With these values we get for observed activity $A_{obs} = (6.3 \pm 0.4)$ Bq. The error analysis of the observed activity is shown in appendix 2.
Using this and the original activity of the source at the measurement day we can calculate the efficiency of the $LaBr_3$ detector.

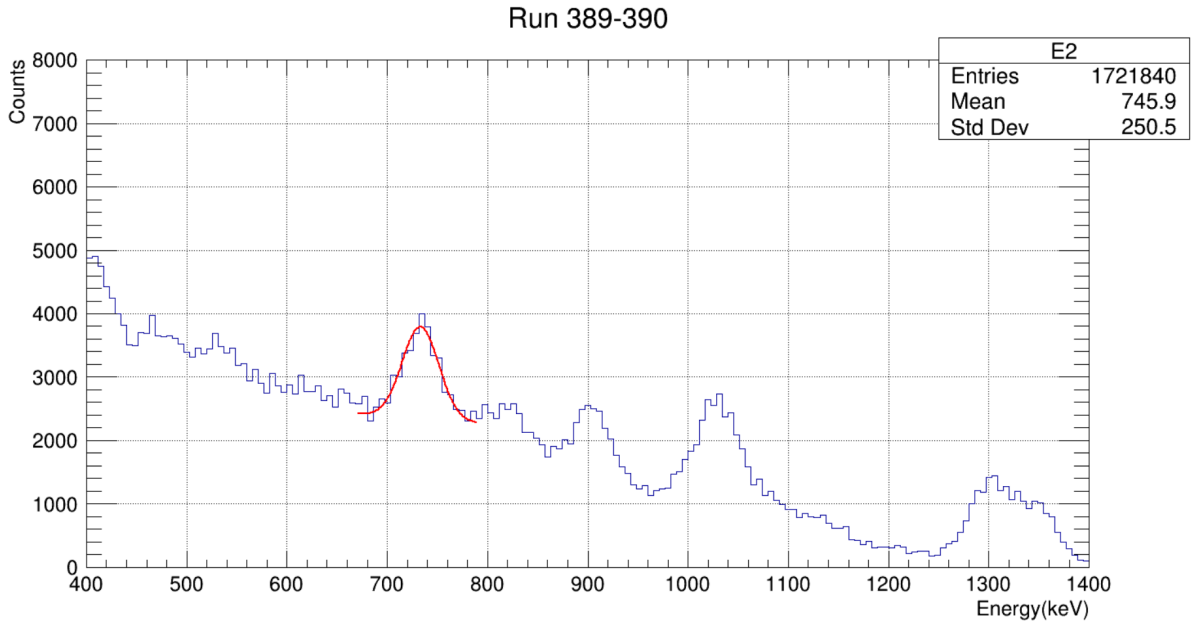

Figure 12. Efficiency calibration measurement made using a ^{152}Eu source with a modified gaussian fitting on 778 keV γ-ray peak.

The activity of the source on the measurement day can be calculated using

$$A = A_0 e^{-\frac{ln(2)}{T_{1/2}}t}, \tag{2}$$

where A_0 is the activity of 40.01 kBq on the reference day 1.4.2003 with an error of 3 %. Our measurement happened on 7.6.2017. The half-life $T_{1/2}$ is 13.517 years for ^{152}Eu. This gives us the reference activity of $A = (19.3 \pm 0.6)$ kBq. Now the absolute efficiency ϵ can be calculated from

$$\epsilon = \frac{A_{obs}}{A}. \tag{3}$$

This gives us an efficiency of $(0.032 \pm 0.003)\%$ at the 778 keV. The error analysis is given in appendix 2. Efficiency calibrations will be described in detail in my MSc thesis.

4 Conclusions

The testing and characterization of the detectors has been successful. We received a new digitizer at the end of January 2017 and it enables us to implement the veto condition offline instead of online. This will make handling the MC^2-analyzer settings for the detectors easier.

The testing of the Scionix β-detector revealed the cross-talk issue between the inner signal detector and outer veto detector. For now the cross-talk issue will only be dealt with by taking it into account while analyzing the collected data, making the data-analysis a bit more tedious. The cosmic-ray suppression of the Scionix veto detector has an efficiency of 98.5 % at high veto trigger threshold setting (610 LSB). With low veto trigger threshold setting (40 LSB) the suppression is even better, but we have to be careful of triggering on the cross-talk pulses. The measurements that were done for the Scionix detector inside the lead cave let us know that a lead shielding around the detector would not help too much to suppress the background radiation and would only complicate our measurement setup. Due to the test measurements there is an idea of a new design for the Scionix β-detector that will give us better shielding against the cosmic rays.

While measuring the efficiency measurements with $LaBr_3$ detector the noticeable slow drift of the γ-peak was caused by the unstable power supply. This will be solved by buying a more stable power supply making the data-analysis a bit more easier. Overall the test measurements provided us good understanding of the effects of the MC^2-analyzer settings on the detectors.

After the measurements that are listed on this contribution we have for example tested the Scionix detector in the Pyhäsalmi mine to see if the background radiation at our signal energy region is from the cosmic rays or from something else. Both of the detectors have been used for a test measurement of our whole setup. In the future the new Scionix detector will need similar testing for finding the optimal settings.

References

[1] S. Miyaji, K. Nomoto, K. Yokoi and D. Sugimoto. Pub. Astron. Soc. Japan **32** (1980) 303-329.

[2] S. Jones, F.K. Röpke, R. Pakmor, I.R. Seitenzahl, S.T. Ohlmann and P.V.F Edelmann. Astronomy & Astrophysics manuscript. (2016) arXiv: 1602.05771v2

[3] G. Martínez-Pinedo, Y.H. Lam, K. Langanke, R.G.T. Zegers and C. Sullivan. Physical Review C **89** (2014) 045806

[4] F.P Calaprice and D.E. Alburger. Physical Review C **17** (1978) 730-738

[5] National Nuclear Data Center, http://www.nndc.bnl.gov/chart/ ; taken on 30.10.2017

[6] A. Idini, A. Brown, K. Langanke and G. Martínez-Pinedo. Proceedings of Science NIC XIII (2014) 002.

[7] Picture: W.H. Trzaska.

[8] R. Julin, J. Kantele, J. Kumpulainen, M. Luontama, V. Nieminen, A. Passoja, W. Trzaska and E. Verho. Nucl. Inst. Meth. A **270** (1988) 74-77.

[9] Oliver Kirsebom, private communication

Appendices

Appendix 1: Table 1
Appendix 2: Error analysis for 778 keV γ-ray peak of ^{152}Eu

Appendix 1

Table 1. List of measurements that were done to test the detectors untill the beginning of April.

Runs	Description	Channel
2	Background run with rise time 30 ns, around 8,5 hours of data	2
3	Background measurement with default digitizer settings	0,1
6	Background measurement with more optimized settings	0,1
7	Background measurement with rise time setting reduced to 4us	0,1
8	^{60}Co source on top of the Scionix detector	0,1
9	Measurement with Scionix detector with coincidence condition on	0,1
10 & 11	Measurements with Scionix detector with veto condition on, different coincidence window	0,1
12	Measurement with modified settings	0,1
13	Background measurement	0,1
14 & 15	Measurements with ^{60}Co source	2
18	Background measurement	2
19-20	Background measurement inside the spectrometer	0,1,2
21-34	^{207}Bi source inside the spectrometer, current varying from I/I$_{max}$=20-10 %	0,1,2
35-53	^{207}Bi source, current I/I$_{max}$ = 13,5 %, varying VETO threshold 200 LSB - 20 LSB	0, 1, 2
54-60	^{207}Bi source, current I/I$_{max}$ = 20,6 %, varying VETO threshold 300-50 LSB	0, 1, 2
61-68	^{207}Bi source, current I/I$_{max}$ = 8,2 %, varying VETO threshold 150 - 20 LSB	0,1,2
69	Measurement with different settings, I/I$_{max}$ = 20,6 %, VETO threshold 250 LSB	0,1,2
70 & 71	Background measurement, ^{207}Bi source inside, VETO threshold 610 LSB and 40 LSB respectively	0,1,2
72	Background run, ^{207}Bi source inside, VETO condition removed	0,1,2
73-83	^{207}Bi source inside, magnetic field scan around 1,6 MeV peak I/I$_{max}$ = 29-19 %, no VETO	0,1,2

84-91 & 98-101	^{207}Bi source inside, magnetic field scan around 0,4 MeV peak I/I$_{max}$ = 11-0 %, no VETO	0,1,2
92-97	^{207}Bi source inside, measurements with higher magnetic field I/I$_{max}$ = 30-40 %	0,1,2
102	^{207}Bi source inside, longer measurement on 1,6 MeV peak, I/I$_{max}$ = 20,0 %, VETO enabled	0,1,2
103	^{207}Bi source inside, anti-coincidence condition enabled, I/I$_{max}$=20,0 %	0,1,2
104	^{207}Bi source inside, coincidence condition enabled, background measurement	0,1,2
105	^{207}Bi source inside, I/I$_{max}$ = 20,0 %, VETO enabled with threshold = 610 LSB	0,1,2
106	^{207}Bi source inside, different VETO window, background measurement	0,1,2
107	Background measurement	0,1,2
108	Background run with magnetic fiel on I/I$_{max}$= 40,0 %	0,1,2
109	Background measurement	0,1,2
110-114	Background measurement, VETO threshold 610 LSB	0, 1
115- 119	Background measurement, VETO threshold 40 LSB	0,1
120 & 121	Background measurement, VETO condition off	0,1
122-125	Background measurement , VETO threshold 610 LSB, atm pressure	0,1
126-133	Background measurements with different conditions	0,1
134-137	Background measurement inside a lead cave	0,1
138	Background measurement on the table for comparison to the lead cave measurement	0,1

Appendix 2: Error analysis for 778 keV γ-ray peak of ^{152}Eu

Error for observed activity was calculated from

$$dA_{obs.} = \sqrt{\left(\frac{1}{t_{meas.} \cdot I_\gamma} \cdot \delta N_\gamma\right)^2 + \left(-\frac{N_\gamma}{t_{meas.}^2 \cdot I_\gamma} \cdot \delta t_{meas.}\right)^2 + \left(-\frac{N_\gamma}{t_{meas.} \cdot I_\gamma^2} \cdot \delta I_\gamma\right)^2},$$

where $\delta N_\gamma = 684.609$ counts is the error of the counts, $\delta t_{meas.}$ is the error of the measurement time approximated to be 60 seconds and $\delta I_\gamma = 0.08$ % error of the gamma peak intensity [5]. The calculated error of observed activity was 0.37 Bq.

Error for the activity of the source on the reference day can be calculated

$$dA = \sqrt{\left(e^{-\frac{ln(2)}{t_{1/2}}t} \cdot \delta A_0\right)^2 + \left(\frac{ln(2)}{t_{1/2}^2} t A_0 e^{-\frac{ln(2)}{t_{1/2}}t} \cdot \delta t_{1/2}\right)^2 + \left(-\frac{ln(2)}{t_{1/2}} A_0 e^{-\frac{ln(2)}{t_{1/2}}t} \cdot \delta t\right)^2},$$

where $\delta A_0 = 3.0$ % is the error of activity, $\delta t_{1/2} = 0.009$ years is the error of the half-life and δt is the error of the measurements of the reference day approximated to be 4 hours. The error of activity and half-life are taken from the data sheet of the ^{152}Eu source. The calculated error of the activity on the measurement day was 579.9 Bq.

The error for efficiency can be calculated from:

$$d\epsilon = \sqrt{\left(\frac{1}{A} \cdot \delta A_{obs.}\right)^2 + \left(-\frac{A_{obs}}{A^2} \cdot \delta A\right)^2}$$

using the errors of activities calculated above. The calculated error of efficiency of the $LaBr_3$ detector at the 778 keV peak is 0.003 %.